Indentation and Fracture Behaviour of Electroless Ni-P-based Composite Coatings

by

Chuhong Wang

Submitted in partial fulfilment of the requirements
for the degree of Master of Applied Science

at

Dalhousie University
Halifax, Nova Scotia
August 2017

Table of Contents

List of Tables

List of Figures

Abstract

Ni-P coatings have been a popular option for many applications because of their autocatalytic nature and excellent resistance to wear and corrosion. These properties of Ni-P coating suggest a potential application as a pipeline inner coating in oil industries. However, the erosion and indentation behaviour of the coating have not been fully explored yet. The objective of this study, is to determine the suitability of using electroless Ni-P and Ni-P-Ti coatings in the oil industry. To achieve this objective, Hertzian-type indentation, three-point bending tests and solid particle erosion tests were performed to investigate the extent of the mechanical damage in the coating. Acoustic emission energy spikes were collected and used to monitor crack formation in the coating during indentation and bend tests. The present research also correlates the fracture responses of coating to its microstructure. The microstructure, mechanical properties, erosion and indentation behaviour are identified and discussed in details.

List of Abbreviations and Symbols Used

Abbreviations

AISI	American Iron and Steel Institute
API	American Petroleum Institute
ASTM	American Society for Testing and Materials
FCC	Face Centered Cubic
EDS	Energy Dispersive Spectroscopy
ICP	Inductively Coupled Plasma Mass Spectrometry
XRD	X-ray Diffraction
DSC	Differential Scanning Calorimetry
SEM	Scanning Electron Microscope
FIB	Focused Ion Beam
HV	Vickers Hardness
AE	Acoustic Emission

Symbols

a	Radius of contact circle (mm^2)
P	Load
R	Radius of indentation ball
P_m	Mean contact stress
E	Young's Modulus
$\sigma_1, \sigma_2, \sigma_3$	Principal stress
τ	Shear stress
K_c	Fracture Toughness
d	Thickness of the coating

v	Poisson's ratio
r	Radius of bend ring cracks
M	Bending moment
L	Distance between two lower supports in bend tests
l	Distance between the upper support and the lower support in four-point bending test
I	Moment of inertia
ϵ	Bend strain
b	Width of the specimen
h	Height of the coating
H	Height of the substrate
R^2	Coefficient of determination
F	Initial fracture force
σ_b	Bend strength of the bilayer system
σ_f	Fracture strength of the coating

Acknowledgements

Foremost, I would like to thank my supervisor, Professor Dr. Zoheir Farhat, director of the Advanced Tribology Laboratory (ATL). I am extremely fortunate to have an advisor who guided me all the times when my steps faltered and acted as my mentor and guardian for last two years. He has been supportive since the first day I started working at ATL group. His insightful comments and constructive criticisms motivated me to focus my ideas and raise my standards. He taught me how to express ideas by questioning thoughts. My learning from Dr. Farhat was not only confined into research. I strongly believe my experience at ATL group will be an asset for the next step of my life. Thank you Dr. Farhat, for being such an amazing mentor.

I would like to express my sincerest gratitude to Dr. George Jarjoura. I am deeply grateful to him for all his help and invaluable suggestions. Also, I would like to thank Dr. Hany El Naggar for agreeing to be my thesis committee member. Thank you for guiding me throughout my journey.

I am indebted to the members of ATL. I would like to thankfully acknowledge the contribution of my senior Tahirm Alam. Also, I really appreciate the help and support I received from my group mate and friend Marciel Gaier. I am also thankful to the help from my colleague Dr. Md. Aminul Islam, Abdullah Almotairi, Chenxin Jin and all my present and past group members. I am grateful to Stephanie Hartlen for the help with technical writing. I would also like to thank all the technicians, Peter Jones, Angus MacPherson, Mark MacDonald, Albert Murphy, and Dean Grijm for

the amazing help and support. Last but not least, thanks Patricia Scallion of IRM and Kate Hide as the administrative secretary.

Chuhong Wang

August, 2017

Chapter 1

Introduction

1.0 Background and Objectives

Pipelines are a critical infrastructure in oil and gas transportation, they are considered to be the safest and most cost-effective way for transporting large volumes of petroleum products. Oil and gas are transferred by pipelines from excavation to refineries, terminals and markets. However, the erosion-corrosion damage of pipelines is an increasing problem across the petroleum industry due to the severe erosive and corrosive internal environment of pipelines. The presence of CO_2 gas in pipelines causes internal corrosion, and the interaction between the internal pipeline surface and solid particles carried in the oil results in a progressive mechanical material loss due to erosion [1-3]. The synergistic effect of erosion and corrosion leads to extensive material loss to the pipeline. In addition to erosion-corrosion damage, dents and gauges also contribute greatly to pipeline failures [4]. A dent in a coated pipe causes a local stress and strain concentrations, resulting in a permanent plastic deformation of the steel pipeline and cracks in the coating [5]. Many methods have been proposed to protect pipelines from damages, with internal coatings proved to be the most effective method [6]. Epoxy, polymer tapes and numerous composite coatings are used or tested as inner coatings in industry [6-8]. However, each of these methods has its limitations. Therefore, developing a new low-cost coating that

provides high erosion-corrosion and indentation resistance, while remaining cost effective, is essential.

Electroless nickel coatings have been used in many industrial applications as protection due to its superb adhesion and unique ability to coat metal components regardless of their size and shape [9, 10]. The autocatalytic nature of an electroless nickel reaction creates smooth deposits with uniform depth across all surfaces, including edges and complex interior geometries [9]. Electroless Ni-P coating, which has excellent wear and corrosion resistance, has been adopted for many applications in aerospace, automotive and food industries. It is well known that amorphous Ni-P coating transforms to nickel phosphide and FCC nickel at 300-350°C [9, 11]. Therefore, annealing of electroless Ni-P coating at a temperature up to 350 °C can further improve its hardness and wear resistance as a result of phase transition. The high strength and excellent corrosion and wear resistance make electroless Ni-P coating a potential candidate in the oil and gas industries. The superior corrosion resistance of electroless Ni-P coating in CO_2 and H_2S environments is well demonstrated in published literature [4, 5]. However, to assess the possibility of using electroless Ni-P coating as an inner coating in pipeline steel, it is necessary to investigate its erosion and dent resistance.

However, many researchers have confirmed the brittleness and low toughness of the as-deposited and annealed electroless Ni-P coating [4, 12]. In erosion of brittle materials, brittle fracture in which material is removed from the surface due to surface cracks, is found to be the dominant mechanism [13]. In this case, toughness becomes the most relevant material property that determines the erosion resistance [13, 14]. Thus, adding additive particles to improve the toughness of electroless Ni-P is required. The addition of particles in the Ni-P matrix can further improve its properties. For example, Al_2O_3, one of the most widely used additions, can

improve the hardness and wear resistance of the electroless Ni-P coating, while electroless Ni–P–Si$_3$N$_4$ and Ni–P–CeO$_2$ can improve the corrosion resistance of plain Ni-P coating [15-18]. TiNi alloys are well known for their shape memory, superelastic properties and superb wear and dent resistance [19, 20]. Superelastic TiNi alloy has the ability to accommodate large scale deformation without generating permanent damage [20, 21]. Adding TiNi particles is a possible way to improve the toughness and indentation resistance of Ni-P coatings. However, the difficulty and high-cost of producing TiNi particles limit the usage of TiNi. Adding titanium nano-particles into Ni-P coating and forming TiNi through heat treatment is an alternative way to improve the properties of Ni-P coating.

To investigate the suitability of utilizing electroless Ni-P and Ni-P-Ti coatings in the oil and gas industries, a fundamental understanding of the indentation and erosion behaviour of electroless Ni-P coatings is necessary. Indentation behaviour can help to predict possible failure in coatings. Coating cracks that form under axial loading during indentation tests are recognized as a key factor in limiting the lifetime of brittle materials and coatings. Different types of cracks such as Hertzian, radial, median, and lateral cracks may form during Hertzian indentation [22]. The investigation of coating failure modes and crack types can be used to predict the possible failure of industrial coatings. On the other hand, toughness is the most relevant material property that determines the erosion resistance of brittle materials [13, 23]. Over the years, several methods have been developed to investigate the fracture toughness of brittle coatings on ductile substrates, such as indentation, tensile, bend, and scratching tests [24, 25]. Bend tests provide a simple method for measuring toughness. In addition to toughness, other mechanical properties such as Young's modulus and fracture strength can also be calculated from bend tests.

This research provides a comprehensive and a systematic investigation on the mechanical properties, indentation and erosion behaviour of Ni-P coatings. In addition, the study also correlates the fracture behaviour with the Ni-P coating microstructural transitions during annealing. Moreover, phase transition and fracture behaviour of electroless Ni-P-Ti coating were also investigated. The specific objectives of the research are summarized as follows:

1. Investigate the suitability of utilizing electroless Ni-P coatings in the oil and gas industries by characterizing their mechanical damage under indentation and erosion conditions.

2. Study the effect of coating thickness of electroless Ni-P coatings on indentation behaviour. Investigate the effect of annealing on mechanical properties, and indentation behaviour of electroless Ni-P coatings.

3. Study the erosion behaviour of as-deposited electroless Ni-P coatings in erosive environment.

4. Investigate mechanical properties and indentation behaviour of electroless Ni-P-Ti composite coatings before and after annealing.

1.1 Preparation of Electroless Ni-P Coatings

In general, electroless plating is a way to deposit a metal layer on the surface of materials by autocatalytic chemistry instead of using electric current. Electroless plating solution contains a reducing agent and a metal source, and the process relies on reactions between a reducing agent and metal ions to deposit metal [9]. The method was first proposed by Brenner and Riddell in 1946 [26]. Electroless nickel plating is undoubtedly the most important catalytic plating process in use today. However, the electroless nickel coatings are not pure nickel. It may contain phosphorus, boron or nitrogen, depending on the reducing agents employed in the solution. In the past few decades, electroless nickel-phosphorus coatings have received widespread acceptance and attention due to their excellent chemical and mechanical properties. Generally, electroless Ni-P coatings can be divided into low-phosphorus (3-5%), medium-phosphorus (6-9%) and high-phosphorus (10-14%) content [27]. The properties of Ni-P coatings depend on the composition, which relies on the concentration and operating conditions of the electroless Ni-P solution. Therefore, a fundamental understanding of the reaction mechanisms is necessary to fully understand the properties of electroless Ni-P coating.

1.1.1 Pre-treatment for Electroless Ni-P Plating

Electroless Ni-P coatings can be deposited on a large number of metallic and nonmetallic substrates with different compositions. One of the most important characteristics for a coating is the adhesion between the substrate and the coating. Some of the most common plated substrate metals, such as steel and aluminum, are naturally active. On these metals, the deposition starts with displacement reactions between iron or aluminum and nickel ions. Other metals and nonmetallic substrates require sensitization and activation steps to initiate the deposition [28], [29].

In this study, the substrate used is pipeline steel. Steels are catalytic substrates since an immersion nickel layer forms on the surface from the displacement reaction during the plating. However, steels can be passive when they are contaminated or oxidized. To develop a strong bond between steels and the coating, a thorough surface preparation removing all contaminants and oxide layer is required [9]. Alkaline cleaning solutions can be used to remove the contaminants, while acid solutions can be used to remove the oxide layer. The selection of the alkaline and acid solutions depends on the type of the steel. For example, cast iron, which is porous, requires to be immersed in weak acid pickling solution to avoid exposing and loosening the graphite. Carbon steels and low alloy steels, which are used in this study, need deoxidizing using acid solutions. Hydrochloric acids (10-50%) and sulfuric acids (2-10%) are commonly used. High alloy steels are not naturally active, and they usually need hydrochloric acid for surface activation.

1.1.2 Ni-P Plating Solution Components and Functions

Typically, an electroless Ni-P bath should contain the following components [9, 28, 30]:

i) Main salt

Main salt is a source of nickel ions. In the process of Ni-P coatings, the most common main salt is nickel sulfate. Nickel chloride and nickel acetate are also used in limited applications. However, chloride anions can be harmful to aluminum substrates. Nickel acetate does not significantly influence the properties and deposit process compared with nickel sulfate; however, its high cost limits its use in industries [9].

ii) Reducing agent

Four kinds of reducing agents are used in electroless nickel plating, including sodium hypophosphite, sodium borohydride, dimethylamine borane and hydrazine. Sodium hypophosphite is the one used in Ni-P plating.

In a coating solution with nickel sulfate as main salt and sodium hypophosphite as reducing agent, an electroless Ni-P coating is deposited with the occurrence of the following reactions:

$$2H_2PO_2^- + Ni^{2+} + 2H_2O \rightarrow 2H_2PO_3^- + H_2 + 2H^+ + Ni$$

$$Ni^{2+} + H_2PO_2^- + H_2O \rightarrow Ni + H_2PO_3^- + 2H^+$$

$$H_2PO_2^- + \frac{1}{2}H_2 \rightarrow H_2O + OH^- + P$$

$$3H_2PO_2^- \rightarrow H_2PO_3^- + H_2O + 2OH^- + 2P$$

$$3NaH_2PO_2 + 3H_2O + NiSO_4 \rightarrow 3NaH_2PO_3 + H_2SO_4 + 2H_2 + Ni$$
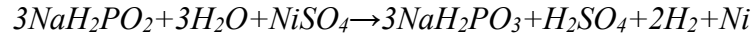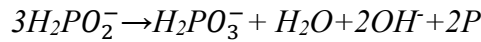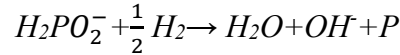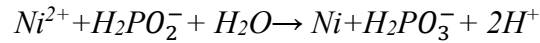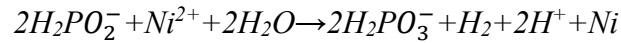
iii) Complexing agents

A Complexing agent is a necessary component in electroless Ni-P coating solution. It can reduce the concentration of free nickel ions, prevent the precipitation of nickel salts, and prevent the pH of the solution from decreasing too fast [9]. Commonly used complexing agents in electroless Ni-P solution are organic acids or their salts [27].

iv) Inhibitors and stabilizers

Inhibitors are usually used to control the pH (long term), and stabilizers can prevent the decomposition and breakdown of the electroless Ni-P coating solution. The most effective stabilizers include compounds of Group VI elements, heavy metal cations, and unsaturated organic acids and so on. The concentration of stabilizers in the coating solution can be very critical. Besides, air agitation can also significantly enhance the stability of electroless Ni-P coating solutions.

1.1.3 Main Plating Parameters

There are numerous parameters affecting the electroless Ni-P coating process, such as temperature, solution pH and nickel and hypophosphite ion concentrations. Since the coating solution used in this study contains nickel sulfate as the main salt and sodium hypophosphite as reducing agent, all the parameters discussed in this section are in a hypophosphite coating solution system.

i) Effect of pH

H^+ is involved in most of the reactions happening during the electroless Ni-P coating process, so the coating process is sensitive to the changes in the pH of the coating solution. In general, plating solutions with hypophosphite as reducing agent can be divided into acidic plating solution and alkaline plating solution. Alkaline solutions are only used in plating low-phosphorus Ni-P coatings in industry. The electroless Ni-P coating produced in this study is high-phosphorus content. Therefore, acidic plating solution is used here. The effect of pH on deposition rate in acidic solution proposed by G.O.Mallory [9] is shown in Figure 1-1. By increasing the pH of the solution, the reaction is accelerated and the deposition rate is increasing. When the pH is lower than 4.0, the deposition rate is found to be very low.
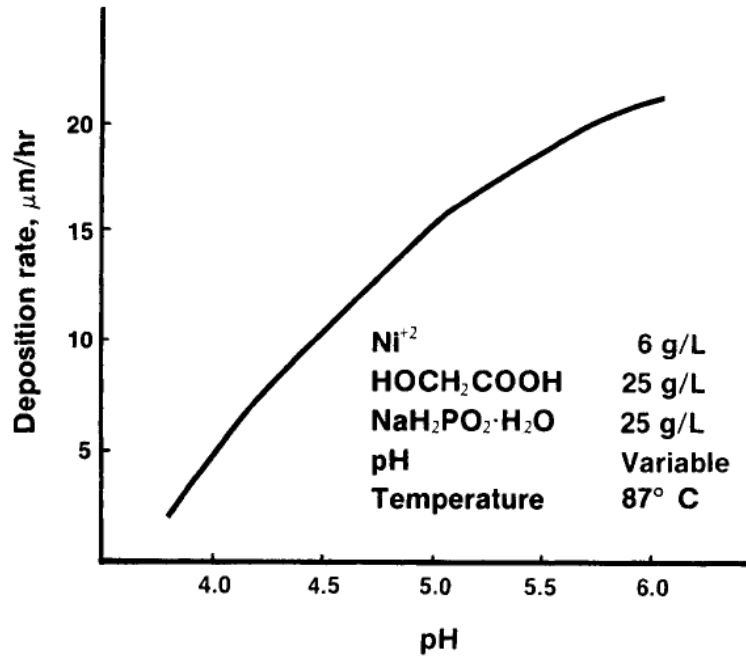
Figure 1-1 Effect of pH on the plating rate [9]

On the other hand, the phosphorus content decreases with the increasing pH (Figure 1-2). High pH retards phosphorus reductions, due to the production of hydroxide ions as a result of the phosphorus reduction reaction. Furthermore, Gutzeit [9] found that the adhesion of electroless Ni-P coating at pH 4.4 is two times higher than that plated at 6.0 on a ferrous substrate. To achieve high adherent coatings, the optimum pH range was found to be 4.5 to 5.2.
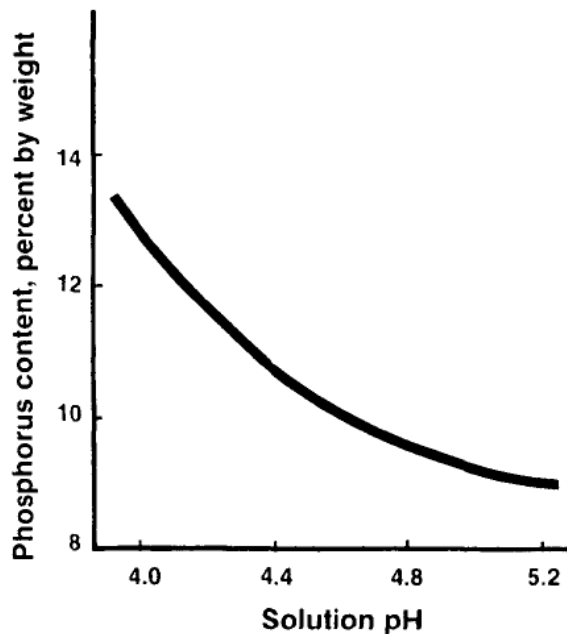
Figure 1-2 Effect of pH on phosphorus content in the coating [9]

ii) Effect of temperature

Temperature of the coating solution during plating is one of the most significant parameters that determine the deposition rate of electroless Ni-P coating. In an acid hypophosphite coating solution, the deposition rate rises exponentially as the temperature increases, since most of the reactions that happen during the deposition process are endothermic. The optimum temperature of an acid hypophosphite solution is between 85-90°C, and most of the acidic solutions are operated at 80-90°C. However, alkaline solutions can be operated at a lower temperature [9].

iii) Effect of concentration

To achieve optimum plating rate, the concentration of nickel ion and the $\frac{Ni^{2+}}{H_2PO_2^-}$ ratio needs to be controlled in a certain range. The nickel concentration in commercial solutions is usually within the range of 4.5 to 11 g/L [9]. It is found that it has little effect on the plating rate, when the

concentration is higher than 5 g/L. And when it is higher than 5.8 g/L, it has no effect on the phosphorus content in the deposited coating. When it is below 5.8 g/L, the lower it is, the higher the phosphorus content in the coating would be. According to the study of Riedel [31], the concentration of hypophosphite should be between 0.15 and 0.35 mol/L, and the optimum $\frac{Ni^{2+}}{H_2PO_2^-}$ ratio should be maintained between 0.25 and 0.6, preferably between 0.3 to 0.45 [30]. When the $\frac{Ni^{2+}}{H_2PO_2^-}$ ratio is too low, the lack of Ni ions in the solution increases the danger of solution decomposition. On the other hand, a high $\frac{Ni^{2+}}{H_2PO_2^-}$ ratio decreases the phosphorus content and slows down the plating rate.

iv) Effect of solution age

With the increasing of coating time, metal source and reducing agent are consumed and their concentrations are continuously decreasing [9]. To keep the Ni-P plating continuous and consistent, replenishing is required.

1.2 Microstructure and Effect of Heat-treatment

The microstructure of as-deposited electroless Ni-P coatings varies with the content of phosphorus. At low phosphorus, Ni-P coatings are nano-crystalline phosphorus supersaturated solid solution of nickel. Electroless Ni-P coatings with high phosphorus content have a semi-amorphous structure. Microstructure of medium phosphorus content coatings is a mixture of amorphous and microcrystalline [27, 32].

During heat-treatment, crystallization occurs and the microstructure of electroless Ni-P coating changes, so do the properties, which is discussed in next section. In general, Ni$_3$P and FCC nickel phases are formed when the annealing temperature is up to 350 °C, however, the crystallization behaviour also depends on the phosphorus content.

Hur, Jeong and Lee studied the crystallization behaviour of electroless Ni-P coatings with different phosphorus contents at relatively low annealing temperature [33]. For low and medium phosphorus content, the phosphorus content is lower than eutectic point (11wt%), so FCC nickel phase precipitated first. And when the phosphorus content in the amorphous Ni matrix increases to 11wt%, further transformation occurs by the simultaneous crystallization of nickel and nickel phosphide into an eutectic structure [34, 35]. Furthermore, during annealing of high phosphorus electroless Ni-P coating, which has an amorphous structure, intermediate precipitates such as Ni_5P_2 and $Ni_{12}P_5$ form first with Ni_3P and nickel followed. The XRD patterns of as-deposited and annealed electroless Ni-P coating with different phosphorus content are shown in Figure 1-3 [33].
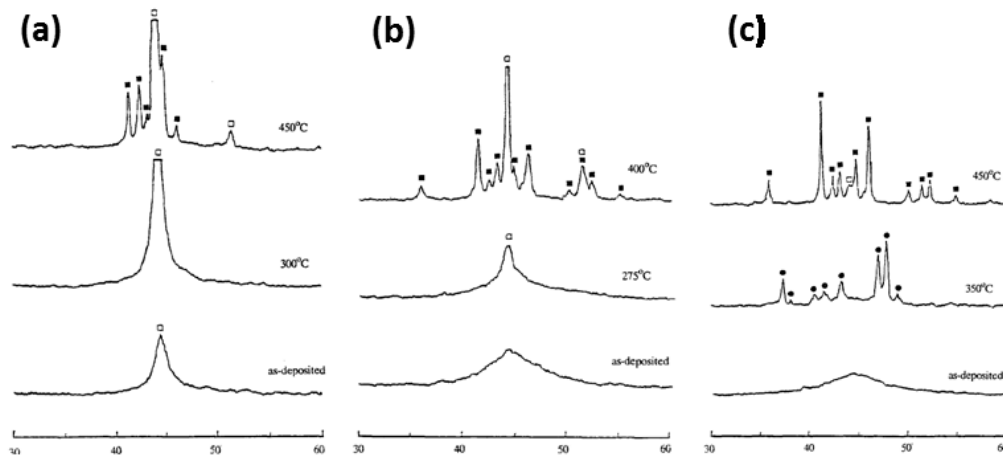
Figure 1-3 XRD patterns of (a) low phosphorus content (6%), (b) medium phosphorus content (10%) and (c) high phosphorus content (14%) Ni-P coating obtained various phases (●Ni5P2 □ Ni ■ Ni3P) before and after annealing [33]

The phosphorus content also influences the phase transition temperature of Ni-P coatings. For low phosphorus coatings with a crystalline microstructure, the crystallization of Ni_3P usually happens at around 400 °C. In medium phosphorus coatings, however, the nickel phase starts to precipitate at 200-300 °C, followed by crystallization of Ni_3P at 300-350 °C [11, 33]. High

phosphorus coatings tend to form Ni_3P and intermediate phases such as Ni_5P_2, $Ni_{12}P_5$ and Ni_2P at 300-350 °C. However, with an increasing temperature, decomposition of intermediate phases occurs at 400-500 °C [33]. The effect of high annealing temperature was also studied by many researchers. Keong and Sha found that the crystallization process completes at 600-800°C and at 800°C the coating is completely crystalized [36].Coarsening of nickel grains was observed in high temperature annealing [33, 37].

1.3 Properties of Electroless Ni-P Coatings

In general, the electroless Ni-P coatings are uniform, hard, relatively brittle coatings with high wear and corrosion resistance. The phosphorus content and the annealing temperature can greatly influence the coating properties. The properties of electroless Ni-P coatings are discussed in detail in this section.

1.3.1 Physical Properties

    1) Density and melting point

The existence of phosphorus content decreases the density of the Ni-P coatings. It varies from about 8.5 g/cm^3 for low phosphorus content coatings to 7.75 g/cm^3 for Ni-P coatings with a phosphorus percentage of 10 to 11wt% [27, 30].

Pure nickel has a melting point of 1455 °C and the existence of phosphorus decreases the melting point of Ni-P coatings. When the content of phosphorus is 11wt% (eutectic point), electroless Ni-P coatings have the lowest melting points of 880 °C. After the eutectic point, the melting point slightly increases with increasing phosphorus content [38].

    2) Uniformity and adhesion

The excellent uniformity is one of the most important reasons that elctroless Ni-P coatings have been widely used. Electroplating usually builds more coatings on the sharp edges while grooves and blind holes have lower thickness [27]. Electroless coatings avoid this shortcoming and can be deposited as a smooth coating with uniform thickness. Moreover, as mentioned above, the deposition starts with displacement reaction between nickel and other metal ions. So the adhesion of electroless nickel coatings to most metals is excellent. The initial displacement reaction allows the deposit to establish metallic as well as mechanical bonds with the substrate. Some non-catalytic metals, on where the initial displacement reaction does not occur, the adhesion is reduced [30].

3) Electrical and magnetic properties

The electrical resistivity of electroless Ni-P coating is higher than that of the pure nickel, which has a resistivity of $7.8×10^{-6}$ ohm cm [27]. With the increasing of phosphorus content, the resistivity of the coating increases as well. Heat treatment increases its conductivity.

As-deposited high phosphorus content electroless Ni-P coatings have non-magnetic properties due to its amorphous microstructure. The non-magnetic property is one of the most important physical properties of Ni-P coatings. Electroless Ni-P coatings are widely used as sub layer coating for computer memory disks due to the non-magnetic property [27].

Some other typical physical properties of electroless Ni-P coatings are summarized as Table 1-1 [27].

Table 1-1 Some typical physical properties of electroless Ni-P coatings [27]

Properties	Low Phosphorus Content	Medium Phosphorus Content	High Phosphorus Content
Internal stress (MPa)	-10	+40	-20
Coefficient of thermal expansion (mm/m°C)	12.4	13	12
Electrical resistivity (ohm cm)	30	75	100
Thermal conductivity (W/cmK)	0.6	0.05	0.08
Specific heat (J/kg K)	1000	-	460
Magnetic coercively (A/m)	10000	100	0

1.3.2 Mechanical Properties

1) Hardness, ductility and elastic modulus

The Vickers micro-hardness of as-deposited Ni-P coating is between 500-600 (4.9-5.9 GPa). Low temperature annealing significantly increases the hardness of Ni-P coatings. After annealing at 400 °C for 1 hour, the hardness of electroless Ni-P coatings can compare to that of hard chromium. The highest hardness reported is 1400 $HV_{0.1}$, typically 1000-1100 $HV_{0.1}$ (9.8-10.7 GPa)[18]. With increasing annealing temperature, the hardness of the annealed coatings decreases.

Electroless Ni-P coatings are found to be relatively brittle. They have high Young's modulus and limited ductility. The ductility of electroless Ni-P coatings varies with phosphorus content and the thickness. Low and medium phosphorus coatings, have low ductility below 0.7 due to the crystalline structure [27]. High phosphorus coatings, however, have higher elongation due to the amorphous structure and lack of lattice defects. Thin films of as-deposited high phosphorus coatings can be bent completely without fracture

[30]. As it can be expected, heat treatment, which causes crystallization, reduces the ductility of electroless Ni-P coatings.

Young's modulus of electroless Ni-P coatings with high phosphorus content is found to be around 170 GPa [12]. Low phosphorus coatings have a lower Young's modulus of around 130 GPa. Medium phosphorus content coatings, however, have the lowest Young's modulus. Heat treatment can slightly increase the Young's modulus of electroless Ni-P coatings.

   2) Frictional properties and wear resistance

The excellent wear resistance of electroless Ni-P coatings is one of its most important properties, and the wear behaviour of Ni-P coatings can be even further improved by heat treatment. High phosphorus content Ni-P coatings annealed at 400 °C for 1 hour have optimum hardness and wear resistance.

The frictional property of Ni-P coatings also vary with phosphorus content. The phosphorus content provides natural lubricity.

1.3.3 Corrosion Properties

Electroless Ni-P coatings can provide a pore-free barrier coating to protect the substrate from the corrosive environment. In neutral or acidic conditions, amorphous structure (high phosphorus content coatings) can provide better corrosion resistance due to its amorphous nature and the absence of grain or phase boundaries. Many applications of electroless Ni-P coatings are built up on the superb corrosion resistance in multitudinous corrosive environments. Corrosion rates of Ni-P coatings with a phosphorus content of 11-12% in different environment are shown in Table 1-2. Heat treatment, which results in the crystallization of FCC nickel and Ni_3P, decreases the corrosion resistance.

Table 1-2 Corrosion rates of electroless Ni-P coatings in different environment

Environment	Corrosion rate (μm/year)
Acetone	0.08
Ferric chloride	200
Nitric acid	25
Sodium carbonate, saturated	1
Sodium hydroxide, 50%	0.2
Sulfuric acid	9
Water, acid mine, pH=3.3	7

The corrosion of carbon steel in CO_2 environments (carbonic acid) has been a continuing problem in oil and gas industries [39]. Stainless or other high alloy steels are usually used as pipeline materials due to the corrosive environment where there are CO_2 and H_2S. If stainless steel can be replaced by electroless Ni-P coated low carbon steel, the corrosion resistance can be increased, and it is more economic efficient.

1.4 Electroless Ni-P Composite Coatings

Ni-P composite coatings with particle reinforcement can further improve the properties of plain Ni-P coating. Embedding particles in high phosphorus electroless Ni-P coating is found to be an efficient method to prepare composite coatings. Many newly developed Ni-P composite coatings are being used or tested. Particles such as Al_2O_3 [15, 40] , SiC [31, 41], diamond and PTFE [42] are commonly used. The existence of particles causes an increase in roughness and a decrease in thickness of Ni-P coating. SiC particles can increase the hardness and wear resistance of electroless Ni-P coatings. Moreover, wear resistance of electroless Ni–P–SiC composite coatings increases with the increasing of SiC content in coatings [31, 43]. Ni–P–Al_2O_3 deposits are also found to have higher hardness and wear resistance than plain Ni-P coating. Electroless Ni–P–PTFE coatings offer non-stick, higher dry lubricity, low friction, good wear and corrosion resistant surfaces.

As mentioned above, electroless Ni-P coatings are brittle coatings with relatively low roughness. Embedding particles reinforcement provides a potential way to improve the toughness of the coating. TiNi alloy, which exhibits shape memory and superelasticity at different temperatures is a possible choice. Shape memory effect of TiNi is achieved at low temperatures while superelasticity property can be gained at higher temperatures [21]. Superelastic TiNi alloys have high recoverable strain during deformation due to stress-induced martensitic transformation. During loading process, the austenite phase transforms to detwinned martensite while the reverse transformation from martensite to austenite occurs during unloading. Superelastic TiNi alloy can accommodate high impact load without permanent deformation. Therefore, it is widely used in a variety of industrial applications such as automotive, aerospace and biomedical industries. It also has high corrosion resistance. The superelasticity of TiNi makes it a good candidate to reinforce electroless Ni-P coatings.

However, the difficulty and high cost of producing TiNi have limited the usage of TiNi. If TiNi can be produced by adding titanium powder into electroless Ni-P coating and annealing, the properties of electroless Ni-P coatings can be significantly improved.

1.5 Indentation Fracture

In 1881, a new period of contact mechanics was opened by the publication of the paper *On the Contact of Elastic Solids* by Heinrich Hertz [44]. After that, indentation tests have been used to measure the hardness and Young's modulus of materials. It is also used to analyze and characterize fracture and deformation properties of brittle materials. Cracks occur in indentation contact are important features in many engineering applications, such as bearings and engine components [45]. Different types of indenters are used in indentation tests, such as Hertzian indenter, Vickers indenter and

Berkovich indenter. Compared with other indentation types, Hertzian indentation has a well-defined stress field until the point of fracture [46]. Therefore, in this study, the Hertzian-type indentation is used, and only Hertzian indentation features are discussed within this section. Before investigating the mechanism of cracking, a detailed knowledge of Hertzian stress field is required.

1.5.1 Hertzian Indentation and Stress Field

Hertzian-type indentation was first studied by Heinrich Hertz. To analyze the stress distribution of stress field between two elastic bodies in indentation contact, he assumed that the surfaces are non-conforming, frictionless, and the strains are small and within the elastic limit. Consider the radius of the sphere indenter is R. The effective elastic modulus is E^* and the applied load is P (Figure 1-4) [45].
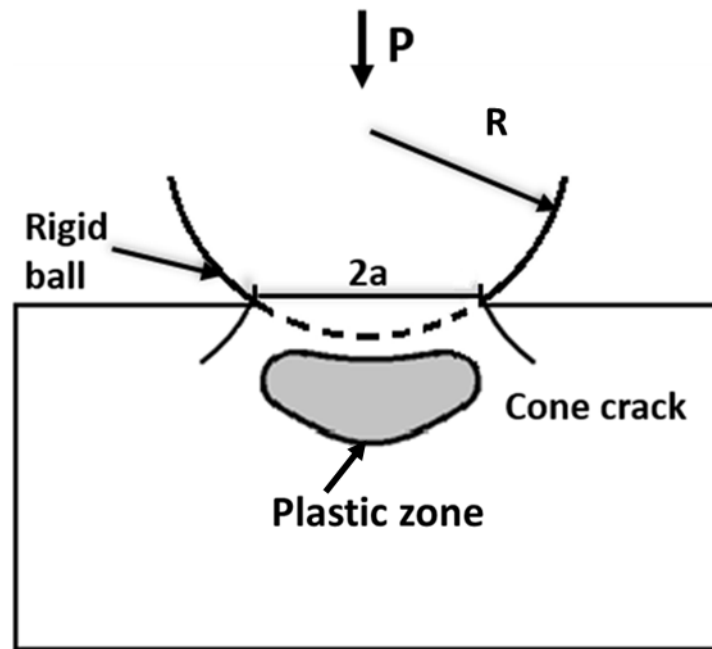
Figure 1-4 Schematics of the indentation process

It is found that the radius of the contact circle has following relation to E^*, P and R:

$$a^3 = \frac{3PR}{4E^*} \qquad\qquad \text{Equation 1}$$

where E^* is the combined modulus of the indenter and the specimen, given by:

$$\frac{1}{E^*} = \frac{(1-v^2)}{E} + \frac{(1-v'^2)}{E'} \qquad\qquad \text{Equation 2}$$

where E' and v', and E and v, are the elastic modulus and Poison's ratio of the indenter and the specimens, respectively [46]. The mean contact pressure, p_m, is given by:

$$p_m = \frac{P}{\pi a^2} = \left(\frac{4}{3}\frac{E}{\pi k}\right)\frac{a}{R} \qquad\qquad \text{Equation 3}$$

The mean contact pressure is considered as the indentation stress, and a/R, which is the ratio of radius of contact zone 'a' over the radius of indenter 'R', is used as indentation strain [47]. The principal stresses σ_1, σ_2 and σ_3 and maximum shear stress τ_{max} are given in the following equation and shown as Figure 1-5 [48, 49].

$$\sigma_{1,3} = \frac{\sigma_r + \sigma_z}{2} \pm \sqrt{\frac{(\sigma_r - \sigma_z)^2}{2} + \tau_{rz}^2} \qquad\qquad \text{Equation 4}$$

$$\sigma_2 = \sigma_\theta \qquad\qquad \text{Equation 5}$$

$$\tau_{max} = \frac{1}{2}(\sigma_1 - \sigma_3) \qquad\qquad \text{Equation 6}$$

where σ_r and σ_z are the redial and normal stress, respectively. τ_{rz} is the shear stress, σ_θ is the hoop stress. σ_1, which is on the flat surface, is compression under the indenter and tension in the interior. σ_2 is equal to σ_θ is a hoop stress, while σ_3 is compressive everywhere. In general, $\sigma_1 > \sigma_2 > \sigma_3$. The maximum shear stress is in the subsurface, and the value and location depends on the Poisson ratios. For a Poisson ratio of 0.33 ($v = 0.33$), the maximum shear stress locates at $\approx 0.5a$ underneath the indent with a value of $0.48p_m$.
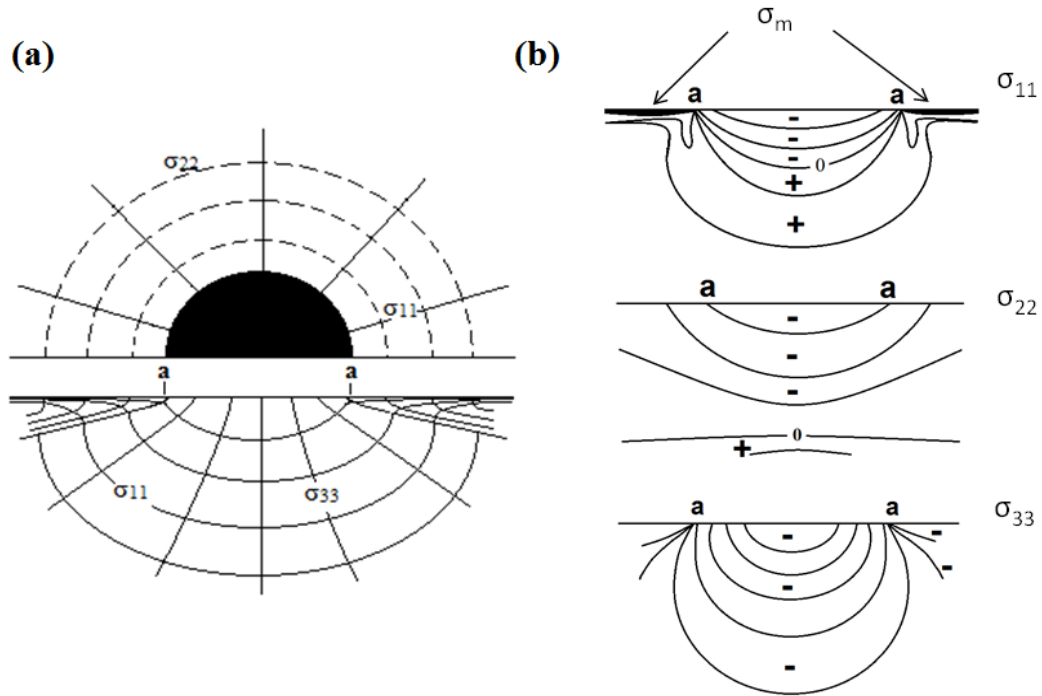
Figure 1-5 a) Schematic diagram of principal stress trajectories of near-
contact field, surface view (top) and side view (bottom), (b)
principal stress contours [49]

1.5.2 Fracture Mechanisms

Indentation tests have been widely used to study the micro-fracture in brittle
materials. Different types of cracks can be generated by indentation contact.
Robert Cook and George Pharr[22] identified five different crack types
occurring under sharp indenter and spherical indenter. They are cone,
radial, median, half-penny and lateral cracks (Figure 1-6)[22].
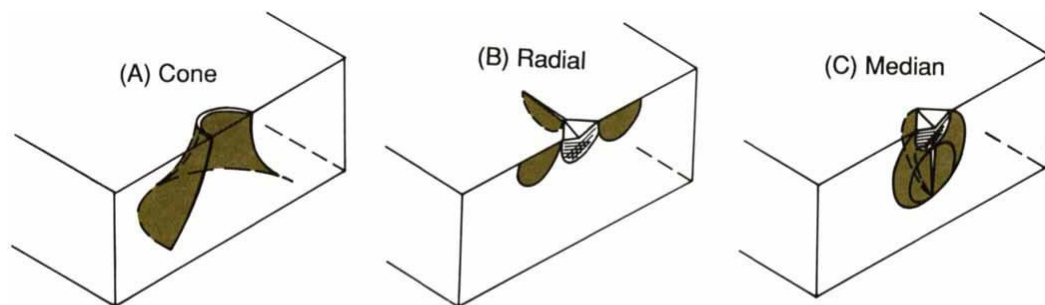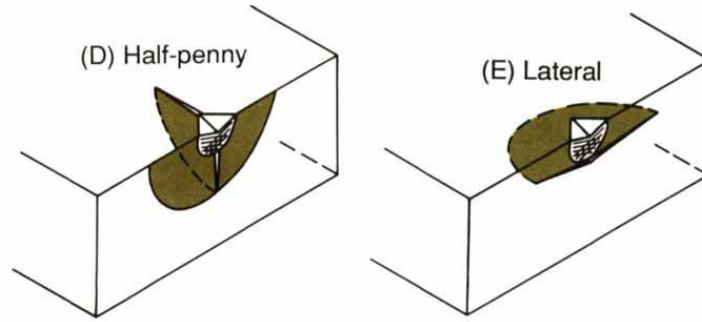
Figure 1-6 Idealized morphologies of five different kinds of cracks [22]

   1) Hertzian crack (cone crack)

Cone cracks and Hertizian ring cracks are typical in spherical indentation. A cone crack was first studied by Hertz in 1881 on silicate glass. The crack initiates as a surface ring crack at the edge of contact and then propagates downwards, forming a cone eventually. The angle of the cone where the crack extends depends on the Poisson's ratio of the material.

As mentioned above, the radius of the contact area can be calculated by Equation 1. And the maximum tensile stress occurs at the contact edge is given by

$$\sigma_{max} = (1 - 2v)\frac{P}{2\pi a^2} \qquad\qquad \text{Equation 7}$$

Substituting Equation 7 and Equation 3:

$$\sigma_{max} = \left(\frac{(1 - 2v)}{2\pi}\right)\left(\frac{4E^*}{3}\right)^{2/3} P^{1/3}R^{-2/3} \qquad\qquad \text{Equation 8}$$

This maximum tensile stress is responsible for the generation of Hertzian cone cracks.

After Hertz, a linear relation between the load and sphere size was established by Auerbach in 1891. He found that the force P required to initiate a Hertzian crack is related to the radius of indenter R and it can be presented by:

$$P = AR \qquad\qquad \text{Equation 9}$$

where A is a constant. This is well known as "Auerbach's law" and it led to the famous brittle fracture theory. The Auerbach's law proposes that the tensile strength of material depends on the radius of the indenter instead of Poisson's ratio of the materials. Subsequently, Griffith energy balance criterion for fracture was applied to the Hertzian contact in 1960s. This was followed by many refined theories.

2) Redial cracks (Palmqvist cracks)

Radial cracks can be observed in both spherical and sharp indentation. A radial crack is usually parallel to the load axis, radiating from the edge of the plastic contact [22]. The localized load generated due to the plastic deformation is the driving force for radial cracks. Radial cracks are first observed by Palmqvist on a WC-Co surface. Many studies showed that they exist under a wide range of contact loads. The plastic deformation generates a localized load, which is the driving force for a radial crack. Radial cracks usually grow during the loading segment of the cycle [22].

3) Median and half-penny cracks

Median cracks are also parallel to the load axis. However, they generate beneath the elastic-plastic zone. A median crack is usually observed in sharp indentation. The first real evidence of the existence of median cracks came from the work of Lawn and Swain in 1975 [50]. They predicted a linear dependence of the median crack depth on the indentation load. Their theory oversimplified the propagation of median cracks. Other researchers have extended the theory. Lawn and Fuller [51] later emphasized the role of residual stress associated with the deformation zone in expanding the median cracks to the surface during unloading. Evans and Charles [52], and other researchers, found that a simple but powerful means for determining the toughness of ceramics is needed. They measured the Kc values independently [53]. Other researchers also proposed equations to estimate the intensity factor based on the median/half-penny system.

A half-penny crack can be generated from a median crack grown toward the surface, a radial crack propagated downward, or a median and a radial crack coalesced. It was first observed by Peter [22] in 1964 in spherical and Vickers indentation in glass.

4) Lateral cracks

Lateral cracks, which are usually circular in shape, are found to be parallel to the surface and formed beneath the deformation zone. Comparing with other cracks, it only occurs during the unloading process, which indicates that the residual stress is the driving force for lateral cracks.

1.5.3 Contact and Fracture of Brittle Coatings

Brittle coatings such as electroless Ni-P coatings, thermal barrel coatings and hard chromium coatings are widely used to improve surface properties of ductile substrates. The stress field and indentation behaviour in such cases are more complicated than that in a monolith material. The thickness is a critical scaling factor in the fracture properties of the brittle coating/ductile substrate systems. A comprehensive understanding of stress field and crack system of the brittle/ductile bilayer system is essential in this work.

Location of crack initiation is consistent with stress distribution. Therefore, stress distribution analysis can help with locating stress concentrations at which cracking may occur. Stress distribution of Hertzian contact in a bilayer system is different from that of monolithic. The stress distribution in the coating is a combination of Hertzian elastic contact and residual stresses produced from substrate plastic deformation. The elastic-plastic contact can be treated using the expanding cavity model [28]. Expanding cavity model assumes that the contact area is a hemispherical core with a radius of a. The hemisphere is surrounded by an incompressible plastic zone of radius r_c, which is surrounded by an elastic zone. With the increase of applied load, the

contact area and hemispherical core increase by *da*, shown in Figure 1-7 [54]. The increase of the hemisphere results in the increase of the plastic zone.
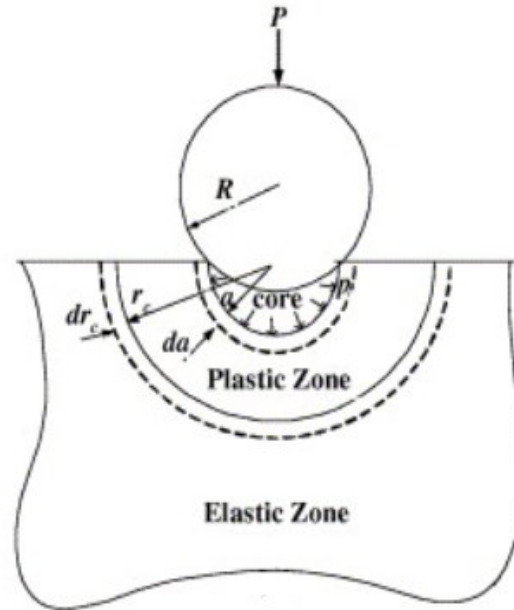
Figure 1-7 Schematic diagram of elastic and plastic zones under spherical indentation [54]

In addition to the five crack types introduced above, surface bend cracks (also called bend ring cracks) due to bending of the coating may occur on brittle coatings on compliant substrates. The plastic deformation in subsurface leads to the bend stresses in the coating, which initiate bend cracks on the coating surface and/or radial crack propagated from the interface (bottom face of the coating) [55, 56]. The difference between bend ring cracks and Hertzian cracks is that bend ring cracks form at a distance from the contact edge, and the radius of bend ring cracks is larger than that of Hertzian cracks.

Four typical crack systems under Hertzian indentation are summarized in Figure 1-8. The thickness of the coating is *d*, and the elastic modulus of coating and substrate are E_c and E_s, respectively. A load of *P* is applied on the bilayer system, resulting in a contact area with a radius of *a*. *R* is the

indenter radius and r is the radius of bend ring crack. Figure 1-8 (a) is a dominant surface Hertzian crack system; (b) shows a dominant bottom radial crack with outer bend ring cracks on top surface; (c) is a bottom radial crack dominant system with inner bend ring crack, and (d) shows through-thickness Hertzian ring cracks. These fracture modes of bilayer systems are highly influenced by the coating thickness. Hertzian cracks are dominant in thick and thin coatings, while bottom radial cracks and surface bend ring cracks are more common in intermediate coating thickness. The stress field and crack propagation are discussed in detail as follows.
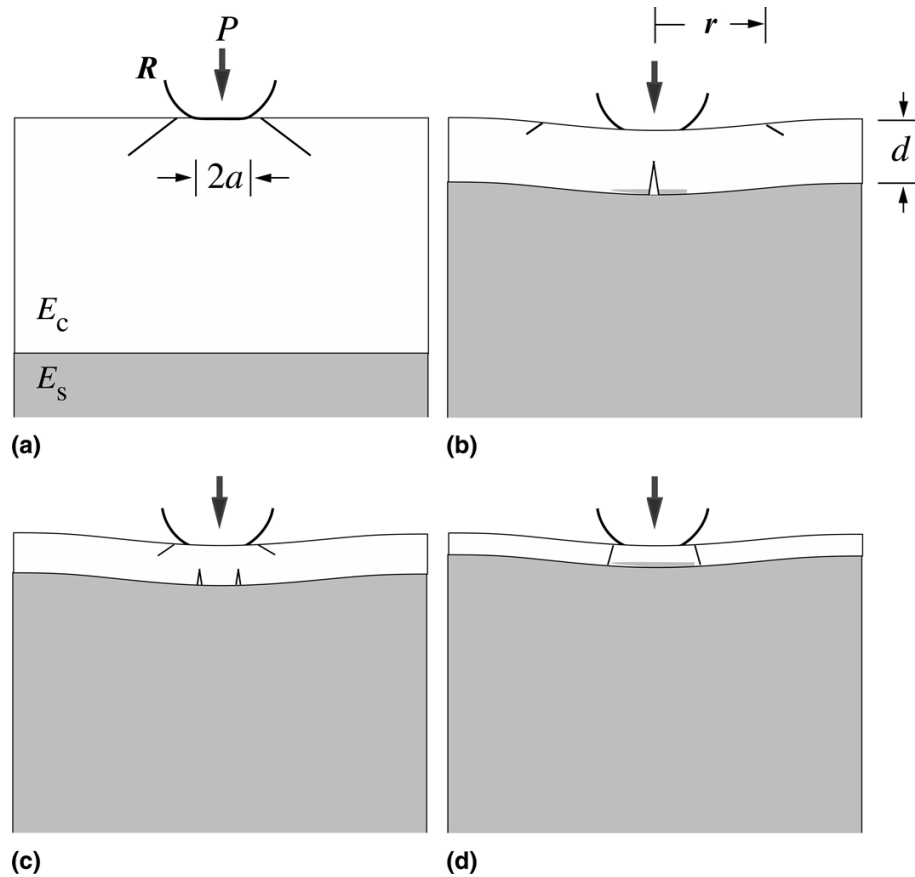
Figure 1-8 Crack types in bilayer systems [56]

   1) Thick coatings (d>>a)

When the thickness of the coating is much higher than the contact area, the load applied is mainly supported by the coating, and the stresses are

concentrated on the contact edge. In this situation, the coating is considered as a monolith. The maximum tensile stress causes Hertzian crack propagation in the coating. The stress field is similar to classical Hertzian field in monolith. The maximum stress is concentrated on the contact edge. The maximum tensile stress is

$$\sigma_c = P/Aa^2 \qquad \text{Equation 10}$$

where A is a proportionality coefficient which can be calculated by $A = 2\pi/(1 - 2v_c)$. The critical load to initiate surface crack is

$$P_{ring} = AS_ca^2 \qquad \text{Equation 11}$$

where Sc is the strength of the coating as a in monolith.

2) Intermediate thickness coatings

Intermediate thickness is the most complicated case. Both damage modes (b) and (c) happen in intermediate thickness. The stress distribution in intermediate coating is shown as Figure 1-9. Radial cracks propagate from the bottom are primary in this thickness region. The maximum tensile stress at the center lower coating surface can be obtained by:

$$\sigma_c = \left(\frac{P}{Bd^2}\right) \log(\frac{CE_c}{E_s}) \qquad \text{Equation 12}$$

where B and C are constants. And the critical load for radial crack is

$$P_{rad} = Bd^2 S_c / \log(\frac{CE_c}{E_s}) \qquad \text{Equation 13}$$

Bend ring cracks also initiate in intermediate coating thickness. The critical load for bend ring cracks can be calculated by:

$$P_c = \frac{(B' S_c d^2)}{\log(C' E_s/E_c)} \qquad \text{Equation 14}$$

where B' is a coefficient and d is coating thickness. The radius of bend ring crack can be determined using the following equation [30],

$$R = b\, d\, log\, c\, E_c/E_s \hspace{3cm} \text{Equation 15}$$

where b and c are constant coefficients. In addition to bend ring cracks and radial cracks, Hertzian cracks are also observed in this thickness region. The difference between bend ring cracks and Hertzian cracks can be distinguished by looking at the cross section. Hertzian ring cracks extend downward and outward and form cone-shaped cracks, while surface bend ring cracks extended downward vertically. This region has a mixed mode where Hertzian-type contact and coating flexural cracks both activate simultaneously [49].

a/d = 10
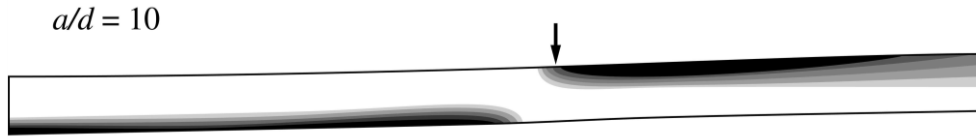
Figure 1-9 Stress distribution in coating when a/d is 10 [56]

3) Thin coatings

In this region, coatings are thin, and the load is essentially supported by the substrate. The stress distribution of substrate can be analyzing using Hertzian contact stress fields of monolithic material. And the coating can be considered as a membrane with a uniform section stress. Ring cracks in thin coatings can initiate if the applied load (P) exceeds the critical load (P_c), where P_c can be calculated using the following equation [16]

$$P_c = A\, S_c a^2 \left(\frac{E_s}{E_c}\right) \hspace{2cm} \text{Equation 16}$$

where E_s and E_c are the Young's modulus of the substrate and coating, respectively. A is a proportionality coefficient and is given by $A = 2\pi/(1 - 2v_c)$ in Hertzian contact. Hertzian ring cracks may extend all the way through the coating. When cracks reach the substrate, they stop propagating. Bend stress concentrates at the edge of the indentation resulting in bend cracks to form in conjunction with the Hertzian cracks. For

this reason, no ring or radial cracks due to bending are observed. The applied load is mostly supported by the substrate so plastic deformation of the substrate is dominant.

Other less common damage modes may occur in coatings. Delamination at the coating/ substrate interface may occur when the coating exhibits weak bonding to the substrate or when higher loads are applied [24, 25]. Delamination generally occurs due to compressive residual stress developed by the substrate during the unloading cycle as the substrate elastic recovery occurs [14, 26].

1.6 Toughness Measurement

As mentioned above, the hardness of the substrate is a less important factor in erosion behaviour of brittle materials. Toughness, however, plays a more important role in erosion. Brittle fracture is the dominant mechanism of erosion on brittle material, and toughness measures the ability of a material to resist the growth of a crack. Toughness of a material also shows its ability of a material to absorb energy during deformation up to fracture [25]. Compared with fracture toughness, which only counts energy required to enable the crack from propagation to fracture, toughness includes the energy that creates and enables the crack to propagate until fracture [25]. Toughness of bulk materials can be easily measured according to ASTM standards. However, measurement of toughness of thin films is more complicated and there are no standards to follow. Different methods have been employed to measure toughness for thin film and coatings, and the most commonly used methods include bending, scratching, nanoindentation, and tensile tests. In this study, bend tests are used to measure the elastic modulus and toughness of electroless Ni-P coatings.

A bend test is a common mechanical test to measure the Young's modulus and flexural strength of materials [24, 25]. It is more suitable for brittle materials such as ceramic, plastic and some powder metallurgy processed metals than tensile tests, since brittle tensile samples tend to break around gripping during tensile tests. A smooth beam specimen is used for three-point or four-point bending tests. Figure 1-10 shows schematics diagrams of three-point and four-point bending tests, respectively.
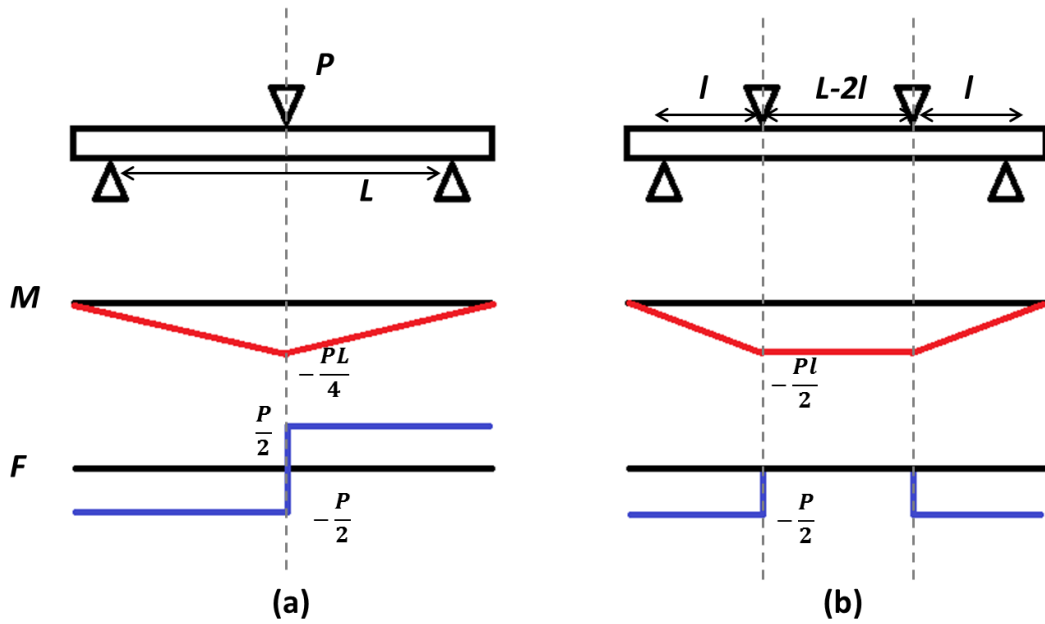
Figure 1-10 Schematic diagram of three-point or four-point bending tests

Here, P is the load applied; L is the distance between two supports on the bottom; and l is the distance between two upper supports (only for four-point bending test); H is the thickness of the specimen and the width of the specimen is presented as b.

For three-point bending tests, the bending moment M is

$$M = \frac{PL}{4} \qquad \qquad \text{Equation 17}$$

The moment of inertia I is

$$I = \frac{bH^3}{12} \qquad \qquad \text{Equation 18}$$

The bend stress σ is

$$\sigma_b = \frac{MY}{I} = \frac{\frac{PL}{4}\frac{H}{2}}{\frac{bH^3}{12}} = \frac{3PL}{2bH^2} \qquad \qquad \text{Equation 19}$$

where Y is the vertical distance away from the neutral axis. The bend strain is

$$\epsilon = \frac{6Hb}{L^2} \qquad \qquad \text{Equation 20}$$

And the elastic modulus is

$$E = \frac{kL^3}{4bH^3} \qquad \text{Equation 21}$$

where k is the slope of the initial straight portion of the load-deflection curve.

For four-point bending test the bending moment M is

$$M = \frac{Pl/2}{2} \qquad \text{Equation 22}$$

The moment of inertia I and the bending stress σ are also depend on the relationship between L and l. For example, when the loading span is 1/2 or 1/3 of the support span, the bending stress is shown as Equation 23 and 24, respectively [57].

$$\sigma_b = \frac{3Pl}{4bH^2} \qquad \text{Equation 23}$$

$$\sigma_b = \frac{Pl}{bH^2} \qquad \text{Equation 24}$$

Bend tests can also be used to measure toughness for bilayer system. When the load P is the load that enables the first crack, the fracture strength of the coating can be calculated. The toughness can be calculated by measuring the area of the curve from start until fracture.

In addition to toughness, other mechanical properties such as Young's modulus and fracture strength can also be calculated from bend tests. The mechanical response is related to the elastic modulus of both the substrate and the coating. The Young's modulus of the substrate and coating-substrate bilayer system are calculated, respectively, from [58, 59]:

$$E_s = \frac{L^3 k}{4bH^3} \qquad \text{Equation 25}$$

$$E_b = \frac{L^3 k}{4b(H + h)^3} \qquad \text{Equation 26}$$

where E_s is the Young's modulus of the substrate, E_b is the Young's modulus of the coating-substrate bilayer system, b is the width of the specimen; and H

and h are the thicknesses of the coating and substrate, respectively. l is the distance between the two supports of the bending apparatus and k is the slope of the initial straight part of the force-displacement curve. To separate the Young's modulus of the coating from the bilayer system, different models are used by researchers. Selected theories are discussed below.

Bao et al. [60] developed the composite plate theory using the difference in deflection of coated and uncoated samples and in the theory the Young's modulus is calculated by following equations:

$$E_f = \frac{-A + \sqrt{A^2 + C}}{2(\frac{h}{H})^3} E_s \qquad \text{Equation 27}$$

where,

$$A = 4(\frac{h}{H})^2 + 6\frac{h}{H} + 4 \qquad \text{Equation 28}$$

$$C = 4(\frac{h}{H})^2(F - 1) \qquad \text{Equation 29}$$

$$F = (1 + \frac{h}{H})^3 \frac{E_c}{E_s} \qquad \text{Equation 30}$$

$$E_c = \frac{L^3 k}{4b(H + h)^3} \qquad \text{Equation 31}$$

A. Rouzaud [58] provided a way to calculate the Young's modulus and fracture strength. In his model, the specimen must be a flat beam specimen with one-side coating, and the coated side is in tension during the test. The substrate is much thicker than the film. The beam ratio (length/thickness) should be large. He also assumed that the Poisson's ratio of the substrate and coating are similar. Furthermore, there is no coating delamination when the substrate is subjected to elastic bending. Under these assumptions, the Young's modulus of the coating is determined from Equation 32, which is derived from an energy balance of the system (Equation 33).

$$\frac{E_c}{E_s} = \frac{H}{3h}\frac{F_2 - F_1}{F_1}$$

Equation 32

$$U = W = U_c + U_s$$

Equation 33

where U is the energy consumed during bending of the bilayer system, U_c is the energy of bending the coating and U_s is the bending energy of the substrate. E_c is the Young's modulus of the coating. F_2 is the force required to initiate the first crack and F_1 is the force in the substrate corresponding to the same deflection in the coating. Furthermore, the fracture strength of the coating is calculated from

$$\sigma_f = \frac{E_c}{E_s}\frac{F \times L/2 \times h/2}{2I}$$

Equation 34

where σ is the fracture strength of the coating, F is the applied force that corresponds to the initiation of the first crack, and I is the moment of inertia of the specimen.

Li et al. calculated the Young's modulus based on the neutral axis maintaining its original position [61]. In his theory, the specimens have coating on both sides. The following formula is used to calculate the Young's modulus:

$$E_f I_f + E_s I_s = \frac{Pl^3}{48d}$$

Equation 35

Where I is inertia moment, P and d is the load and corresponding displacement in the elastic scope during the bend test. l is the span. The subscript f and s represent film (coating) and substrate, respectively. The inertia moment of are calculated as follows:

$$I_s = \frac{bH^3}{12}$$

Equation 36

$$I_f = \int_H^{H+h} y^2 b dy = \frac{b}{3} \left((H+h)^3 - H^3 \right) \qquad \qquad \text{Equation 37}$$

1.7 Solid Particle Erosion

Solid particle erosion is a progressive material loss from a solid surface due to the mechanical impingement between the surface and solid particles. Solid particle erosion, which is generally classified as wear, is a severe degradation problem in many engineering systems [41]. In oil and gas industries, solid particle erosion is expected since it is unavoidable that there are sands or stones entrained in a gaseous or oil at a significant velocity. Wear and erosion problems cost millions of dollars every year in oil and gas industry [39, 62]. Erosion damage in some specific area such as joint and welded parts can be more drastic [2]. Amongst all methods proposed to protect pipes, internal coating such as fusion bonded epoxy [6], polymer tapes [7, 63] and numerous composite coatings [8, 64], is proved to be the most effective way [6]. To have a better understanding of the effect of electroless Ni-P coating on erosion behaviour of the steel, brief introduction of the erosion mechanisms of both ductile (pipeline steel in this study) and brittle materials is required.

1.7.1 Solid Particle Erosion of Steel

As mentioned above, erosion damage costs millions of dollars every year. Therefore, erosion has received significant attention in recent years [2, 3, 39, 65, 66]. It is well known that erosion is a complicated phenomenon affected by numerous factors. Erosion damage can vary widely depending on the impact parameters and materials properties. Factors affecting erosion damage include impact angle, impact velocity and size, shape and properties of the erosive particles. For the substrate, the hardness and ductility of the material are also significant factors that affect erosion mechanisms. In this

study, API pipeline steel is used as the substrate. Therefore, a compressive view of some main erosion mechanisms is provided in this section.

There are many different erosion mechanisms involved during erosion processes. These mechanisms often coexist in one specific situation. Though there are many factors affect, the impact angle plays a significant role in erosion mechanisms of steel. In the case of ductile materials, such as steel, the maximum erosion rate is usually found to occur at a low impact angle between 15° and 30°, while in brittle materials it occurs at approximately 90° [13, 67]. The dominant mechanisms of erosion of steel are summarized in Table 1-3,

Table 1-3 Erosion mechanism in the erosion of steel

Erosion mechanism	Impact angle(^{o})
Ploughing	Low
Low angle metal cutting	Low
Microcutting	Low to medium
Secondary metal cutting	Medium to high
Delamination	High
Plastic deformation and fracture	High

Ploughing is the dominant erosion mechanism of low impact angle. Erosive particles move materials to the front and side of the particle. Repeated impacts can cause removal of materials from the edge of the crater.

Depending on the impact angle and particle velocity, there are four different kinds of cutting in the erosion process: low angle metal cutting, mircocutting mode II, microcutting mode I and secondary metal cutting. In low angle metal cutting, instead of embedding themselves deeply into the surface, abrasive particles attain the required critical energy to cut the metal in the form of small metallic chips. In cutting mode II, abrasive particles slide on the surface and squeeze the metal ahead to form ridges, which are then removed due to repeated impacts. In cutting mode I, abrasive particles

36

penetrate deeper into the metal surface, forming a sharp edge vulnerable to subsequent coming particle impact. Secondary metal cutting is described as particles striking the surface and being deflected by the previously embedded particles and eroding a small portion of metal.

Plastic deformation is the dominant mechanism at high angles. It means that the steel surface deforms plastically, and material is removed by fracture due to the repeated impact by the abrasive particles.

1.7.2 Solid Particle Erosion of Brittle materials

It is well known that the effect of impact angle on erosion rate varies between different materials (Figure 1-11). Ductile material such as steel, as discussed above, shows the highest erosion rate at a low angle [13]. Most brittle materials are eroded most rapidly at a high angle. Erosion mechanism of brittle materials is mainly brittle fracture, which happens at a high impact angle. The impact of erosive particles causes cracks on the surface of the brittle coating.
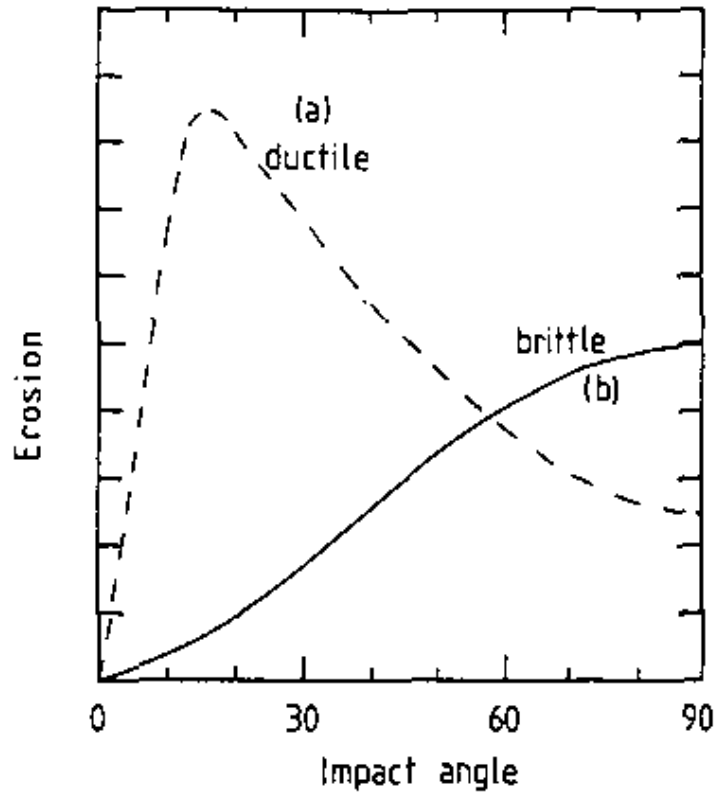
Figure 1-11 The effect of impact angle on erosion rate of ductile and brittle materials [67]

Similar to indentation, different types of cracks are generated during solid particle erosion of brittle material. The size and crack type depend on many factors such as the size, shape, hardness and velocity of the particles [68]. Two types of fractures are commonly observed, Hertzian cone cracks are associated with round particles and preceded only by elastic deformation. Lateral cracks, on the other hand, are usually caused by the contact of sharp angular particles and proceed by local plastic indentation and deformation of the subsurface. Only sharp particles are used in this study, and the velocity and particle size are constant, therefore lateral cracks are to be expected.

Lateral cracks are driven by the residual stresses associated with the plastic zone beneath the indent. When a brittle material is impacted by a sharp angular particle, plastic deformation and radial cracks form, shown in Figure 1-12 [69]. After the impact, plastic deformation and residual stress lead to

tensile stress in the area. The tensile stress results in lateral cracks and material removal.
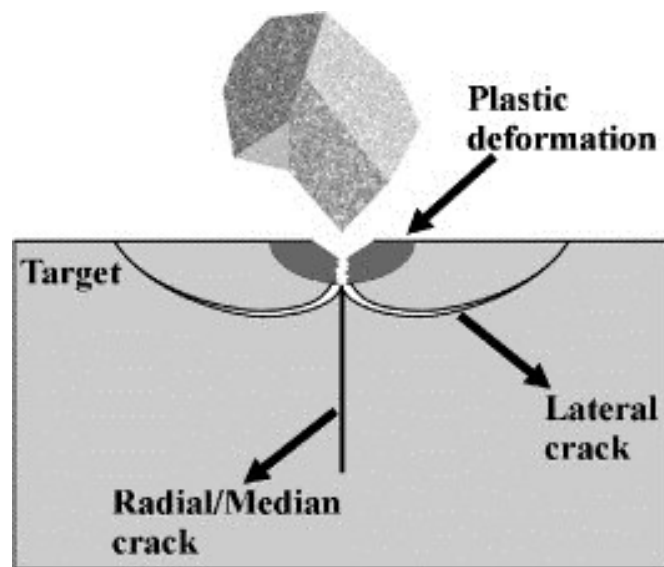
Figure 1-12 Schematics of crack propagation and material removal in erosion of brittle material [69]

Chapter 2

Experimental Details

This chapter presents the preparation, materials characterization, equipment setup and operating conditions employed in this study.

2.1 Coating Preparation

API 5L X100 steel disks (15mm in diameter and 6mm thick) were used as substrate material in all experiments. Specimens were ground using 240, 320, 400 and 600 grit SiC abrasive papers, then polished using 9, 3, 1 μm diamond paste. Following polishing, each specimen was degreased by acetone for 30s. Before plating, pre-treatment process including alkaline cleaning and acid etch was conducted on each specimen (Figure 2-1). Alkaline cleaning was performed in a solution consisting of 50g/L sodium hydroxide, 30g/L sodium carbonate and 30g/L sodium phosphate at 80±5 ºC for 5 minutes and then rinsed with deionized water. Specimens were then etched using a 15% aqueous H_2SO_4 solution for 15s and rinsed with deionized water again before plating.

After pre-treatment, specimens were hung vertically in 1L of electroless Ni-P solution. The coating setup is shown in Figure 2-2. The heating mantle used in this study is Digimantle from Electrothermal Inc.. The coating solution used in this study was a standard commercial grade, Nichem 2500 from Atotech Inc., with nickel sulfate as the main salt and sodium hypophosphite

as the reducing agent. To vary coating thickness, electroless Ni-P coatings were deposited for 1, 4, 6, 8 and 10 hours at a temperature of 88±1 ℃ and pH of 4.7±0.1.

Degrease by acetone t = 30s, room temperature	Alkaline cleaning t = 5 min, T = 80 ± 5 ℃	Acid-etch t = 15s, room temperature	Electroless Ni-P plating t = 1, 2, 4, 6, 8, 10 hrs, T = 88 ± 1 ℃, pH= 4.7 ± 0.1
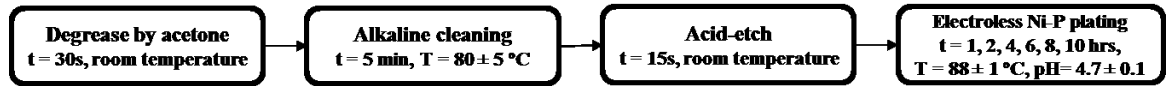
Figure 2-1 Procedure of electroless Ni-P plating
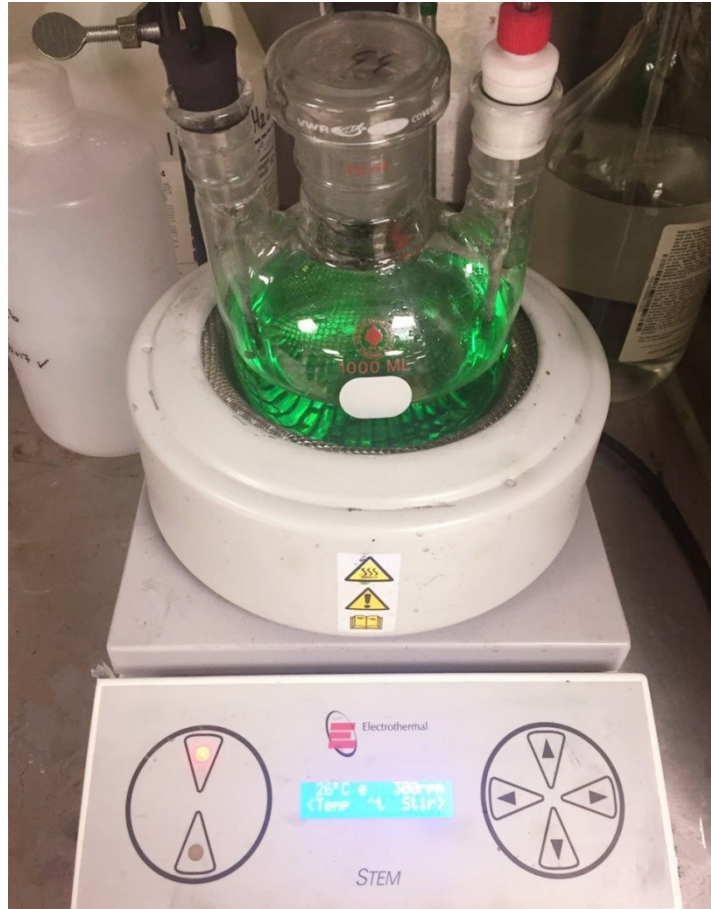
Figure 2-2 Heating mantle and electroless Ni-P coating solution

The experimental procedure to produce electroless Ni-P-Ti coating is similar to that of Ni-P coating. Nichem 2500 solution is used as coating solution as well. 1g of titanium nano-particles were added to a liter of the plating solution. The titanium particles used in this study have a diameter of 70 nm (US Research Nanomaterials Inc.). The composite solution was first mixed using an ultrasonic disperser from Fisher Scientific for 20 min and then stirred at 300 rpm during plating using a magnetic stirring system. 30 mins

41

of plain Ni-P pre-coating is required to increase the interface strength between the substrate and the Ni-P coating. The composite coatings were then deposited for 10 hours at a temperature of 88±1℃ and a pH of 4.7±0.1. A stirring system was used during the entire coating process. A flow chart of electroless Ni-P-Ti plating procedure is shown as Figure 2-3.
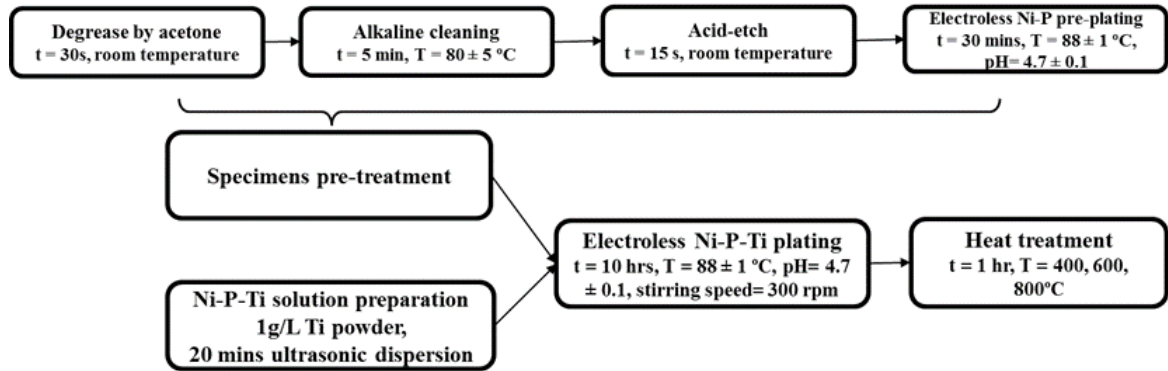
Figure 2-3 Procedure of electroless Ni-P-Ti plating

After plating, specimens coated for 10hrs were then annealed in a vacuum furnace (WEG®) at 400, 600 and 800℃ for 1 hour, with heating rates of 20°C/min. Specimens were placed in a graphite crucible surrounded by alumina particles. The pressure employed was under 1×10^{-6} Pa. The annealing process of 400 ℃ is shown in Figure 2-4 as an example. After heat treatment, specimens were left in the furnace to cool slowly.
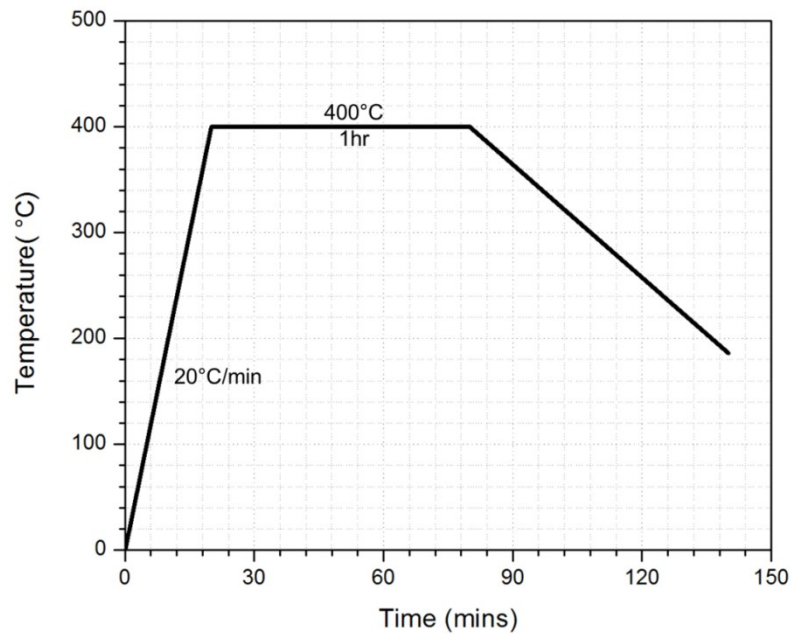
Figure 2-4 Heat treatment curve for 400 ℃ annealing process

2.2 Coating Characterization

After coating preparation, surface morphology, microstructure and mechanical properties of Ni-P and Ni-P-Ti coatings were examined. Indentation and erosion tests were then conducted on the specimens. The test parameters are discussed in this section in details.

2.2.1 Surface Morphology and Microstructure

The surface morphology of electroless Ni-P and Ni-P-Ti coatings are studied using scanning electron microscope (SEM). A Hitachi S-4700 SEM operating at 10 KV and 15μA was used to examine coating morphology and an Energy Dispersive Spectrometry (EDS) coupled to the SEM was used to determine the chemical composition of the coating. An optical 3D profilometer (Figure 2-5) built in our lab was employed to investigate the roughness of the coating.
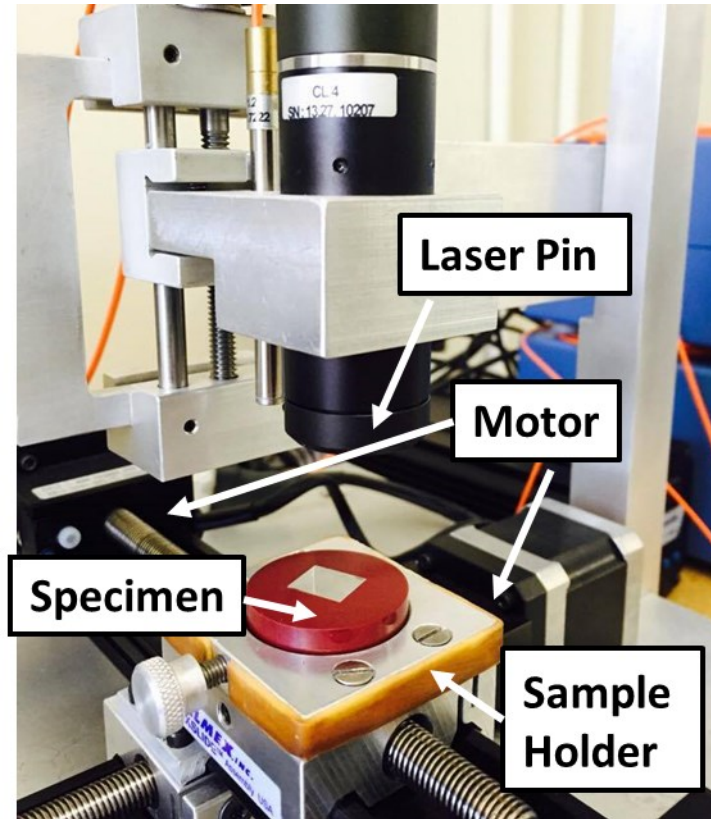
Figure 2-5 The profilometer used in this study

To check the thickness and deposition rate, specimens coated with different deposition times were sectioned using Buehler isomet 1000 precision saw with silicon carbide blade at a speed of 150 rpm. Thicknesses were measured using Olympus Model BX-51 optical microscope, and the deposition rate was calculated as coating thickness per unit time.

As mentioned above, the chemical composition is studied by Energy Dispersive Spectrometry (EDS). Meanwhile, inductively coupled plasma mass spectrometry (ICP) was also employed to analyze the composition of coatings. The equipment used is iCAP 7000 from Thermo Scientific Inc.

Phase transition temperatures of electroless Ni-P coating was identified by Differential Scanning Calorimetry (DSC). The DSC measurement was recorded using a Q600 SDT V8.1 simultaneous DSC from TA Instrument Inc.. Specimens were heated to 800°C at a heating rate of 20 °C/min and then cooled at same rate. An alumina crucible was used as container and high

purity (> 99.999%) argon was allowed through the furnace at 100 mL/min for the entire process. A Bruker D8 Advance X-ray diffraction system (XRD) was used to study the microstructure of the electroless Ni-P and Ni-P-Ti coatings. Cu-Kα radiation with a wave length of 1.54 Å was employed and operated at 40 KV and 40 mA. Specimens were scanned through 2θ of 20º to 120º at a scan rate of 0.2°/s.

2.2.2 Hardness

MicroMet micro-indentation hardness tester was employed to measure Vickers hardness. In each hardness test, a diamond pyramid indenter was forced into the surface with a load of 100g for 30s. The Vickers hardness was taken from five different locations on each specimen, and the hardness values were then averaged. The Vickers hardness is determined from Equation 38, where P is the force applied to the indenter in kilograms-force and d is the average length of the diagonal of the indent in millimeter.

$$HV = \frac{1.8544P}{d^2}$$
Equation 38

To eliminate the effect of the substrate, each specimen was sectioned and Vickers hardness tests were conducted on the cross-sections of the specimen as shown in Figure 2-6.
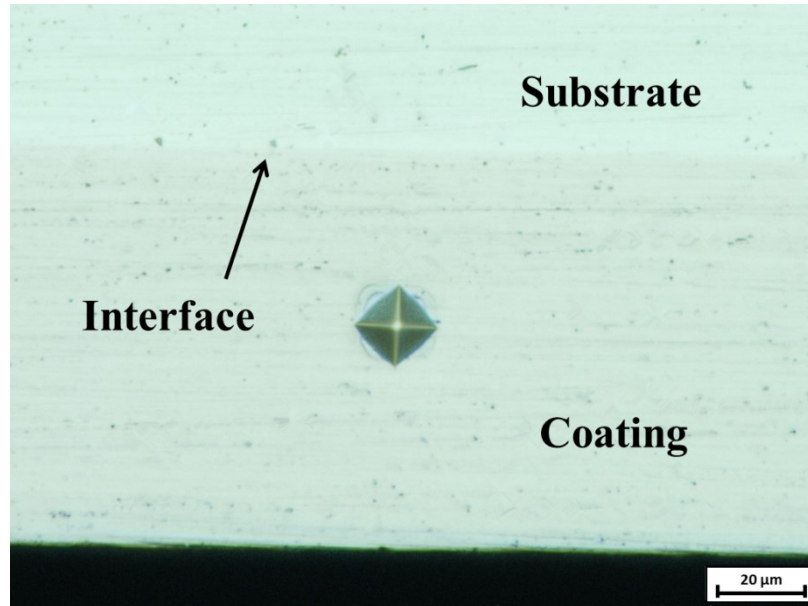
Figure 2-6 Vickers indent on cross-section of a specimen

2.2.3 Toughness and Elastic Modulus

Three-point bending tests were performed on samples using a PASCO ME-8236 apparatus to measure the toughness and Young's Modulus of specimens. The width and thickness of the API steel bending specimens were 19mm and 1.16mm, respectively. Figure 2-7 is a schematic of the three-point bending test set-up, where P is the load applied at the center, L is the support span length, and b is the width of the specimen. The thickness of the substrate is H and the thickness of the coating is h. The load $'P'$ and the associate displacements were recorded automatically during the test.
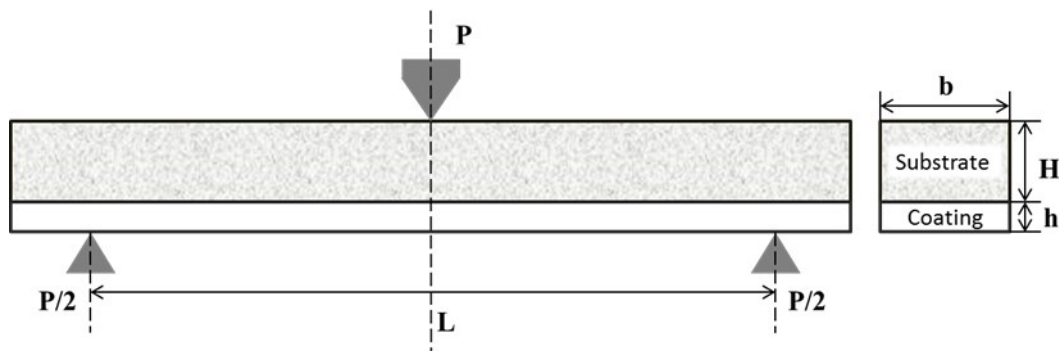
Figure 2-7 Schematic diagram of three-point bending tests

The Young's modulus of the substrate and coating-substrate bilayer system can be calculated using Equation 25 and 26. Equation 32, derived by Rouzaud [58], can be used to calculate fracture strength. It has been known that this method yields accurate results [59, 70, 71]. This equation is derived from an energy balance of the system (Equation 33). In addition, the fracture strength 'σ_f' of the coating can be calculated from Equation 34. Toughness was also calculated using the area under the bending curve from the start of the bend test to the initiation of the first crack. Bend strength of the substrate/coating bilayer system (σ_b) is calculated using Equation 19.

2.2.4 Indentation Tests

An indentation study was carried out using PASCO ME-8236 testing apparatus to characterize the Ni-P and Ni-P-Ti coatings and investigate the effect of coating thickness and annealing. A spherical WC-Co indenter having a diameter of 1.59 mm was used as an indenter. Table 2-1 shows the specifications of the indenter [72]. Wide contact load range from 400 to 2500N was applied to specimens with different thickness. A schematic of the indentation setup is shown in Figure 2-8. Figure 2-8 (a) shows the spherical indenter, while Figure 2-8 (b) shows the contact geometry during indentation. Where P is the applied load; R is the radius of the indenter ball; and $2a$ is the diameter of the contact area. The grey area represents the subsurface plastic zone. Load-displacement data was collected using PASCO Capstone V1.4.1 data acquisition system during the indentation tests. After indentations, the surface and cross-sectional views of indents were studied using SEM and optical microscopy.

Table 2-1 Properties of the WC-CO indenter ball

Properties			Properties	
Composition	C2 grade-6% Co, 94% WC		Surface roughness	0.05 µm
Density	14.95 g/cm³		Young's modulus	650 GPa
Grain size	-1.0 µm		Compressive strength	5.17 GPa
Vickers hardness	1620		Impact strength	1.36 Nm
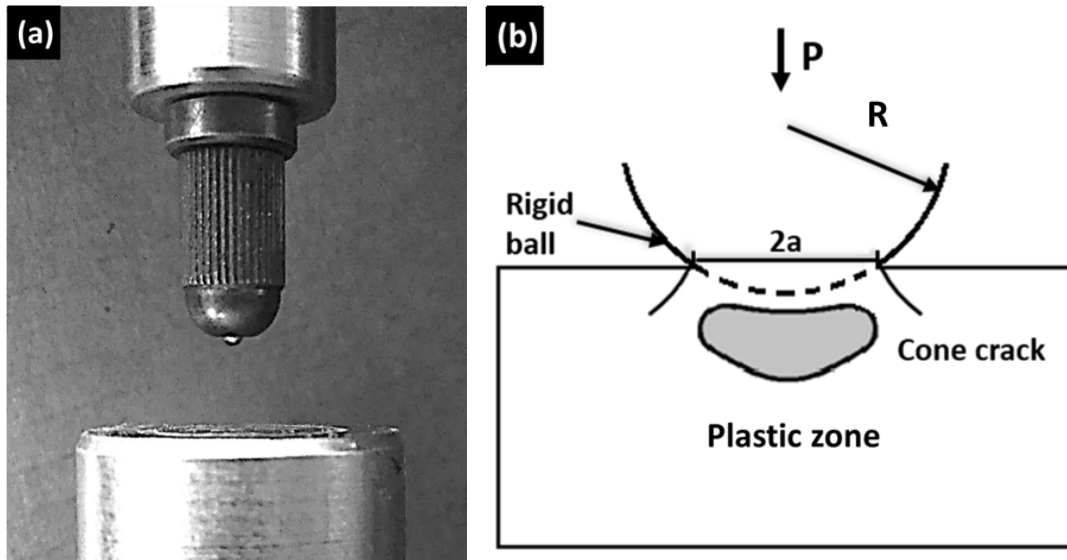
Figure 2-8 (a) spherical indenter in indentation tests, (b) schematic of Hertzian indentations tests

In order to gain an understanding of the indentation elastic-plastic behaviour and crack formation, microscopic circles were drawn on 10hrs coated specimen using FB-2000A focused ion beam (FIB) from Hitachi. Circles with a diameter of 64µm, width and depth of 1µm were milled on the surface and cross-section of two specimens. For the surface specimen, a 2 mm × 2 mm area was covered by 100 circles. For the cross-section specimen, one row of circles was placed on the coating, one row on the coating/substrate interface and three rows on the substrate, as shown in Figure 2-9. Deformation and shape changes of the FIB circles after indentation were examined in details.
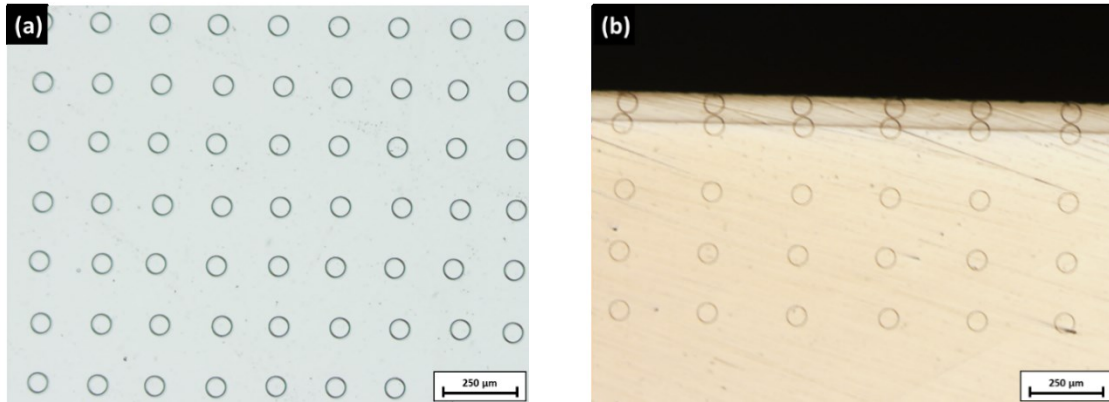
Figure 2-9 FIB circles on (a) surface and (b) cross-section of specimens

2.2.5 Erosion Tests

Erosion tests were performed on 10hrs as-deposited and annealed specimens using a solid particle blast-type erosion tester shown in Figure 2-10. Particle velocity, impact angle and distance between nozzle and specimen can be fully controlled. To investigate the effect of erosion on electroless Ni-P, specimens were eroded using aluminum oxide powder for different time intervals.
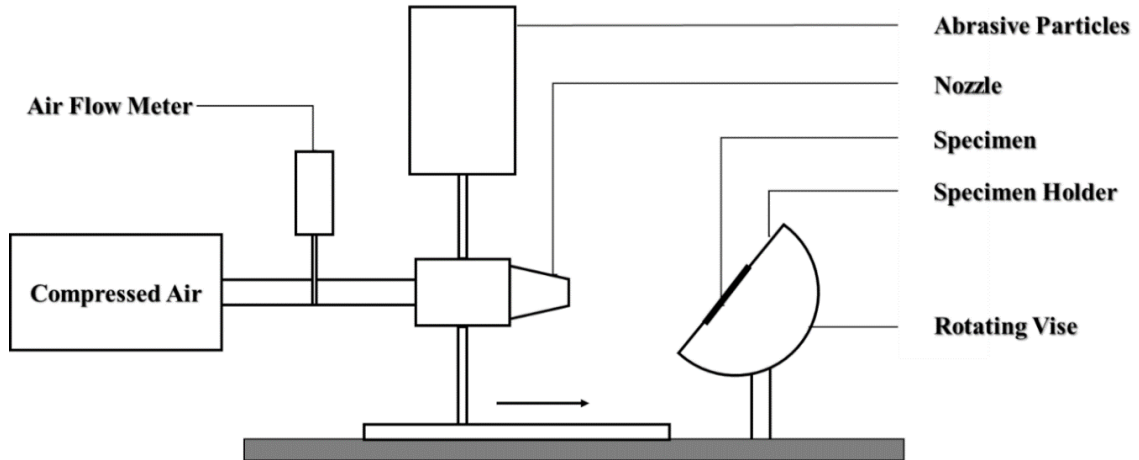
Figure 2-10 Schematic diagram of erosion tester

To study the effect of impact angle on the erosion rate of eletroless Ni-P coating, the as-deposited Ni-P coatings were eroded at 30°, 45°, 70° and 90°. The operating conditions for erosion tests are given in Table 2-2 and the properties of aluminum oxide particles from suppliers are summarized in Table 2-3. Each specimen was weighed using a high precision digital balance before and after erosion tests. After erosion tests, the normalized erosion rate was calculated

using Equation 39 [73]. To study surface and subsurface erosion damage, eroded specimens were examined under SEM.

$$Normalized\ erosion\ rate, E = \frac{Erosion\ rate\ (mg/s)}{Particle\ flow\ rate\ (mg/s)}$$

Equation 39

Table 2-2 Erosion test parameters

Nozzle diameter	2.3 mm
Distance between nozzle and specimen	3 mm
Test gas	Dry compressed air
Test temperature	Room temperature
Angle	30°, 45°, 70°, 90°
Particle velocity	36 m/s
Test duration	5, 10, 15, 30, 60, 180, 300, 420, 600s.

Table 2-3 Properties of aluminum oxide particles

Properties	
Crystal phase	α
Specific gravity	3.95 g/cm^3
Particle shape	Angular
Particle size	57 µm
Hardness	2000 Knoop

2.2.6 Acoustic Emission Monitoring

Crack types can accurately be identified using optical microscope. However, to investigate the fracture process and detect crack propagation, an acoustic emission sensor is necessary. A 1283 USB AE Node AE sensor was used in this study. A schematic of AE sensor is shown in Figure 2-11. When cracks form, fracture energy is released. The sensor attached onto the coating surface detects the released energy and records the acoustic emission waves emitted during crack formation. Different parameters such as amplitude, counts and energy, can be collected using the sensor. It is established in literature that the acoustic emission energy, which is related to fracture energy, is the best parameter to investigate crack propagation [74-76]. Thus, acoustic emission energy spikes were collected and used to indicate crack

formation in the Ni-P and Ni-P-Ti coatings during indentation and bend testing.
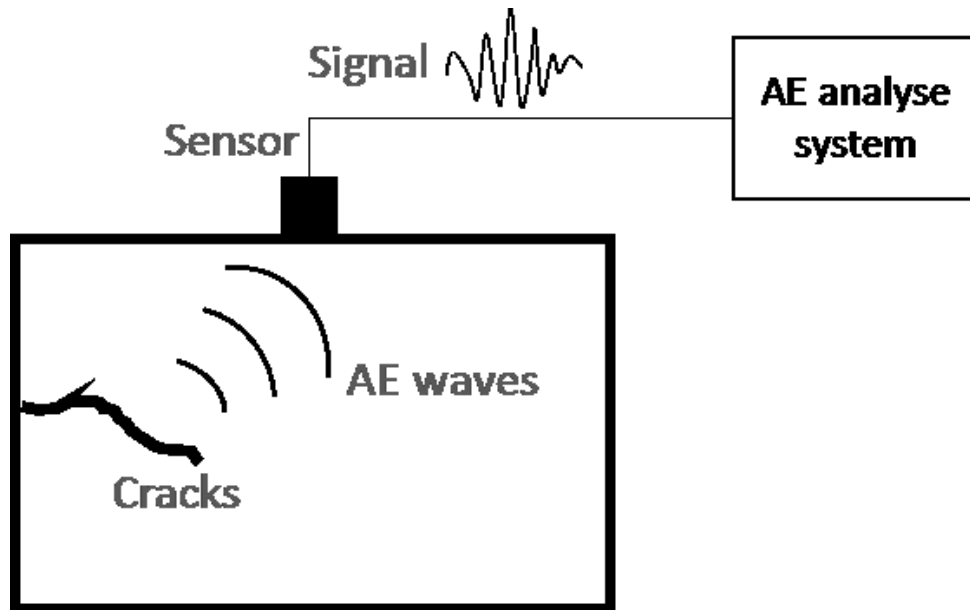
Figure 2-11 Schematic diagram of mechanism of AE sensor

Chapter 3

Results and Discussion

In this chapter, the morphology, microstructure, mechanical properties and indentation behaviour of as–deposited and annealed electroless Ni-P and Ni-P-Ti coatings are discussed. The erosion behaviour of as-deposited electroless Ni-P coatings is also discussed in this chapter. An attempt has been made to evaluate relationships between microstructure and mechanical and indentation properties.

3.1 Coating Characterization

In this section, test specimens were characterized to determine the microstructure, composition and mechanical properties. ICP, SEM and optical microscopy were performed to characterize the materials.

3.1.1 Properties of the Substrate and the Titanium Powder

API X100 pipeline steel is used as substrates in this study. The composition of API X100 steel analyzed by inductively coupled plasma mass spectrometry (ICP-MS) is summarized in Table 3-1, and the mechanical properties are given in Table 3-2. The microstructure of API X100 steel consists of very fine bainite and lath-like ferrite.

Table 3-1 Composition of substrate and coatings

Composition (wt%)	C	P	Cr	Si	Cu	Ti	V	Mn	Fe
API X100	0.103	0.010	0.070	0.121	0.009	0.018	0.036	1.221	Balance

Table 3-2 Properties of API X100 steel

Properties	Yield strength (MPa)	Elongation (%)	Young's modulus (GPa)	Density (g cm^{-3})	Vickers hardness (GPa)	Average grain size (μm)
	690	15.2%	210	7.87	2.50	5±2

The morphology of the nano-titanium particles was investigated. Figure 3-1 shows a SEM micrograph of as-received nano-titanium particles. The average size of the titanium particles is 70 nm. The titanium particles are spherical in shape and some particles appeared to agglomerate.
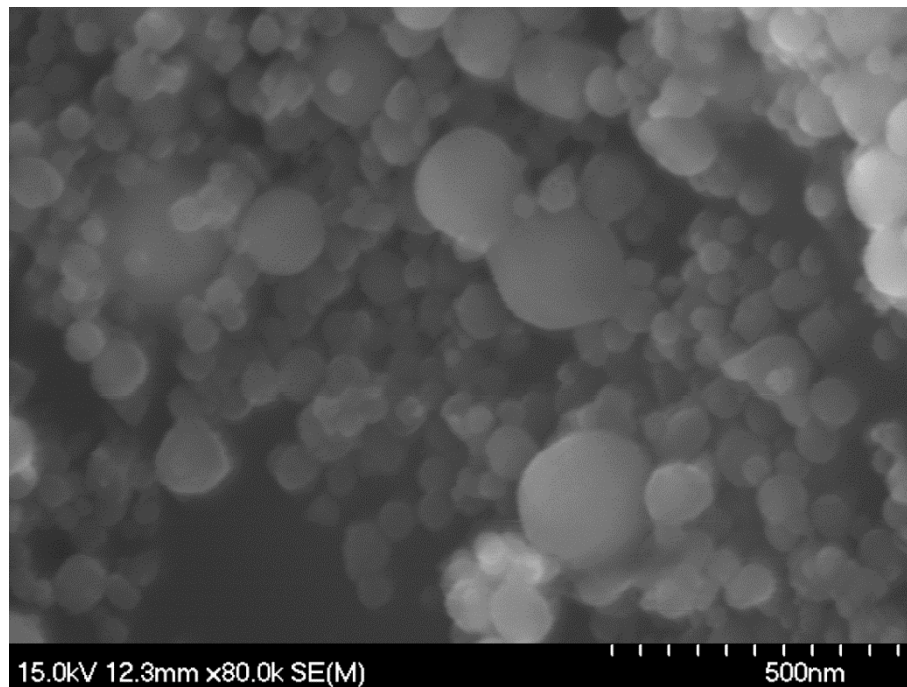
Figure 3-1 SEM micrographs of nano-titanium particles

Figure 3-2 shows the XRD pattern of the as-received titanium powder. Both titanium and titanium oxide peaks were observed.
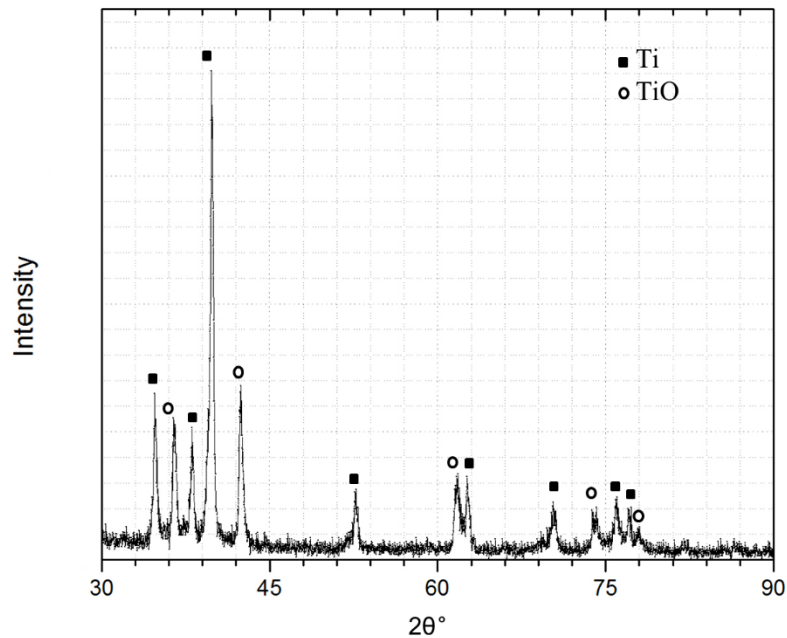
Figure 3-2 XRD pattern of titanium particles

3.1.2 Surface Morphology of Ni-P-based Coatings

Smooth, uniform and dense coatings were successfully deposited on API X100 steel. The relationship between thickness and plating time for electroless Ni-P coating was studied. The measurement of coating thickness versus plating time is plotted as shown in Figure 3-3. Linear and polynomial functions were used to fit the data and the best fit equations are also provided in Figure 3-3. As indicated by the R^2 value, the experimental data seems to fit a polynomial relationship. It can be clearly seen from Figure 3-3 that the deposition rate decreases with increasing deposition time. The deposition rate for plating times up to 4 hours is reasonably constant and has a value of 15 μm/hr. The deposition rate begins to drop gradually when plating time is increased to 8 hours. For plating time over 8 hrs, the deposition rate decreases rapidly to a value of 1 μm/hr. During plating, the metal and the reducing agent are consumed in the electroless plating reaction. As a result, their concentrations in the bath continuously decrease. Gutezit and Kring found that when $H_2PO_2^-$ concentration drops to a certain

54

critical amount and the ratio of $\frac{Ni^{2+}}{H_2PO_2^-}$ is higher than 0.45 [77], the deposition

rate decreases rapidly. Hence, it can be concluded that the drop in deposition

rate with increasing time is due to the depletion of the plating solution.
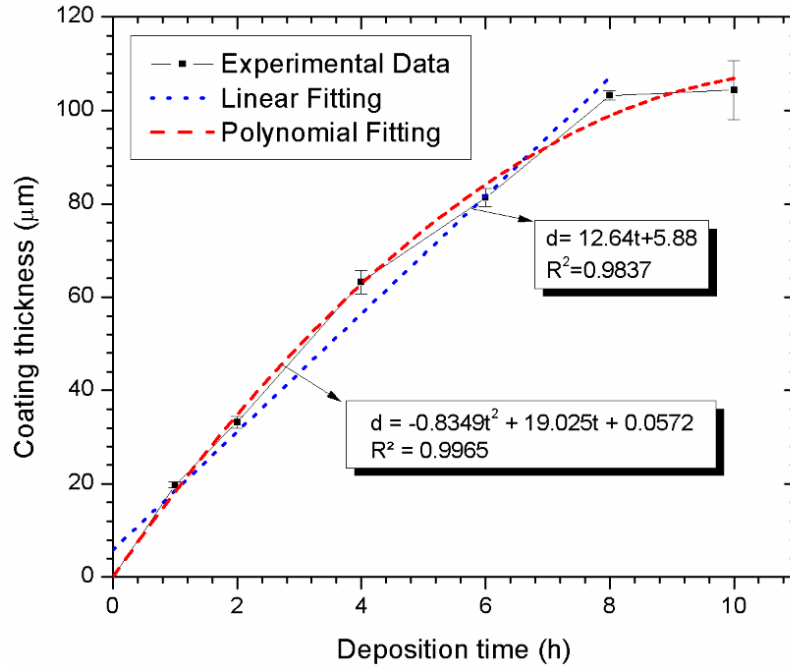
Figure 3-3 Variation plot of Ni-P coating thickness with deposition time

The surface morphology was studied using SEM. Figure 3-4 and Figure 3-5

are SEM micrographs of surface and cross-section morphologies of Ni-P and

Ni-P-Ti coatings, respectively. Figure 3-4 (a) is a surface view of electroless

Ni-P coating. Ni-P coating surface shows few pores with sizes ranging

between 1 to 4 µm. Figure 3-4 (b) is a SEM cross-sectional view of 105µm

thick coating. The interface between the coating and the API X100 steel

indicates that the Ni-P coating is well adhered to the substrate.

The surface and cross-section of the Ni-P-Ti are shown in Figure 3-5. The

surface of the plain Ni-P coating is smoother and more uniform than the Ni-

P-Ti coating. Agglomeration of nano-titanium particles is found on the

surface. The existence of titanium particles led to an increase in roughness.

The surface roughness of Ni-P and Ni-P-Ti coatings are found to be 4 and

12µm, respectively. Figure 3-5 (b) shows the EDS color map of as-deposited

Ni-P-Ti coating. The light (green) color represents titanium and the dark phases are Ni-P matrix (red) and substrate (blue). Titanium particles are well distributed in the coating. The coating/substrate interface was found to be smooth and uniform, identical to plain electroless Ni-P [4]. However, coating delamination was observed during the cutting process, which suggests that the addition of titanium powder decrease the interface strength.
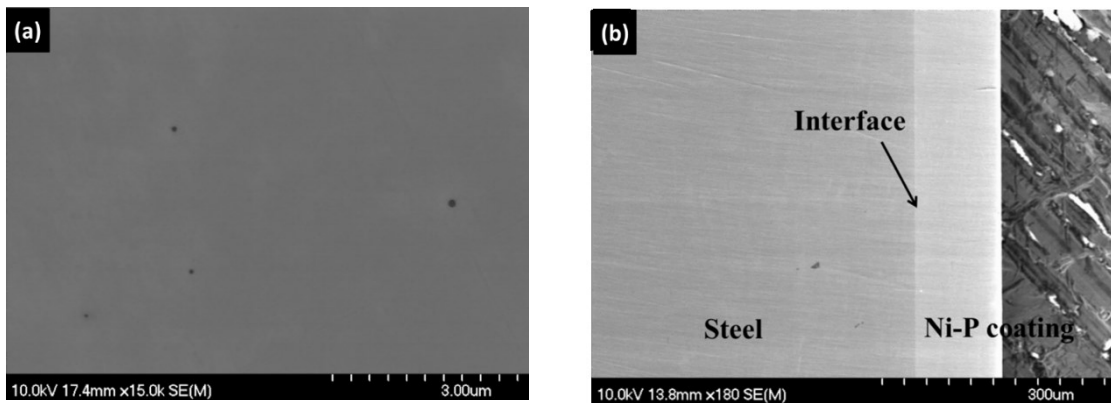
Figure 3-4 SEM micrographs of the (a) surface and (b) cross-section of the electroless Ni-P coating
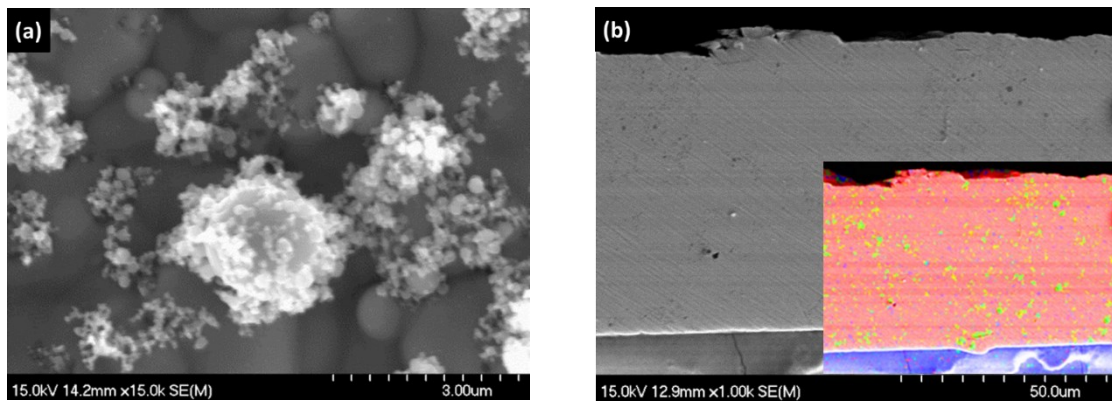
Figure 3-5 SEM micrographs of the (a) surface and (b) cross-section of the electroless Ni-P-Ti coating

3.1.3 Composition and Microstructure

The compositions of the electroless Ni-P and Ni-P-Ti coatings analyzed by inductively coupled plasma mass spectrometry (ICP) are summarized in Table 3-3. The equipment used is iCAP 7000 from Thermo Scientific Inc. In

electroless Ni-P coatings, the phosphorus content of the coating is found to be 10.1wt%, which is considered as high phosphorus content. And in Ni-P-Ti coating, the titanium content was found to be 6.6 wt%. The error margins of phosphorus and nickel elements are 5% and it is 10% for titanium. EDS data of Ni-P coating shows that the average P content is about 10.3 wt% (Figure A 0-1), which is considered similar to the results from ICP tests. However, EDS analysis on Ni-P-Ti coatings shows different results from that of ICP. The titanium content varies from nearly 0 wt% to 60 wt% due to the agglomeration and random distribution of titanium particles.

Table 3-3 Composition of Ni-P-based coatings

Composition	Ni (wt%)	P (wt%)	Ti (wt%)
Ni-P coating	89.89	10.11	---
Ni-P-Ti coating	83.8	9.6	6.6

The effect of coating thickness on crystal structure is studied. The XRD spectra of the substrate and the electroless Ni-P coatings with different thickness are shown as Figure 3-6. For the substrate, the XRD pattern reveals three iron peaks, (110), (200) and (211) as expected. Coating having thicknesses of 63 µm and 105 µm have a broad amorphous peak at a 2θ position of 45°. However, for 18 µm coating, the XRD pattern shows two low iron peaks corresponding to (110) and (211). It is evident that 18µm coating is too thin, and X-ray penetrates to the steel substrate. For thick coatings, the thickness has no effect on its semi-amorphous structure.
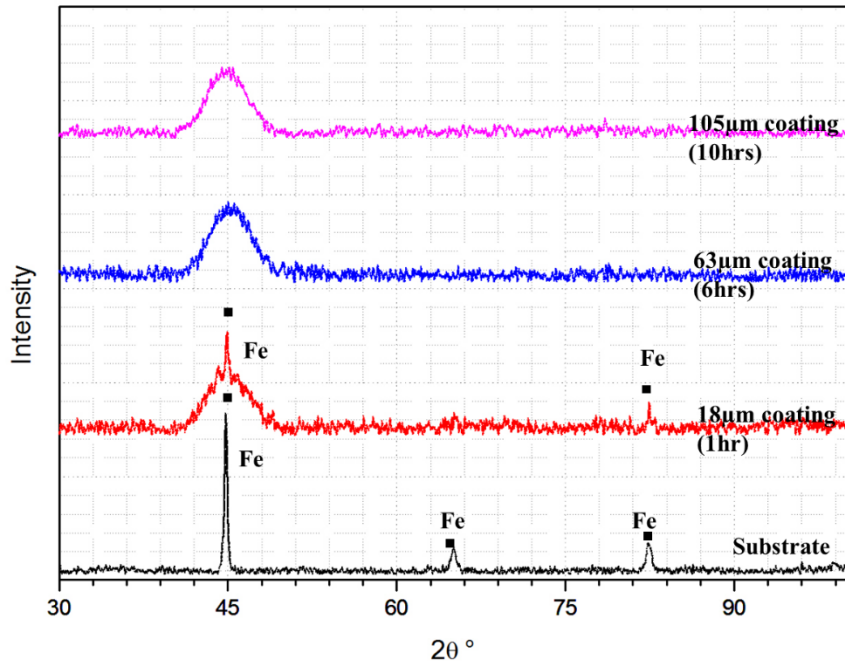
Figure 3-6 XRD spectra of substrate and electroless Ni-P coating with different thickness

The effect of annealing temperature on the microstructure of Ni-P coatings is studied. The XRD patterns of the as-deposited and annealed Ni-P coatings are shown in Figure 3-7. It is clear that annealing results in the crystallization of Ni and precipitation of Ni_3P, and the amount of FCC nickel and Ni_3P vary with increasing temperature. The as-deposited coating has a broad amorphous peak at the 2θ position of 45°. The Ni-P coating annealed at 400°C shows nickel and Ni_3P peaks in the XRD pattern. Duncan [11] indicated that semi-amorphous Ni-P phase transforms to Ni_3P and FCC nickel at 310-330°C. In Ni-P coatings with phosphorus content greater than 11wt%, Ni_3P grows into the amorphous matrix during annealing, until the phosphorus content of the latter falls to 11wt%. On the other hand, in alloys with P<11wt%, amorphous nickel crystallizes first. When the phosphorus content of the amorphous Ni matrix increases to 11wt%, further transformation occurs by the simultaneous crystallization of nickel and formation of Ni_3P into eutectic structure [34, 35]. Therefore, in the present

work, with a phosphorus content of 10.1% and an annealing temperature of 400°C, diffraction peaks of both nickel and Ni_3P appear in the XRD pattern.

When the annealing temperature increases to 600°C, the diffraction peaks of nickel and Ni_3P both increase, with nickel peaks exhibiting higher intensity than Ni_3P. With increasing annealing temperatures of up to 800°C, the peaks are sharper and the nickel peaks become much higher than those of Ni_3P. Similar results were also found in Staia and Keong's work [36, 78]. In summary, nickel crystallization becomes dominant with increasing annealing temperatures, resulting in more crystalline nickel phase in the annealed coatings. In addition, the peaks of coatings annealed at a low temperature (400°C) are broader compared to coatings annealed at a high temperature. In general, the peak in the XRD broadens as crystallite size decreases. Therefore, the grain sizes of the coating annealed at high temperature (600 and 800°C) are larger. The growth of grain size with increasing annealing temperature is also reported by Tien [37], Hur [33] and other researchers.
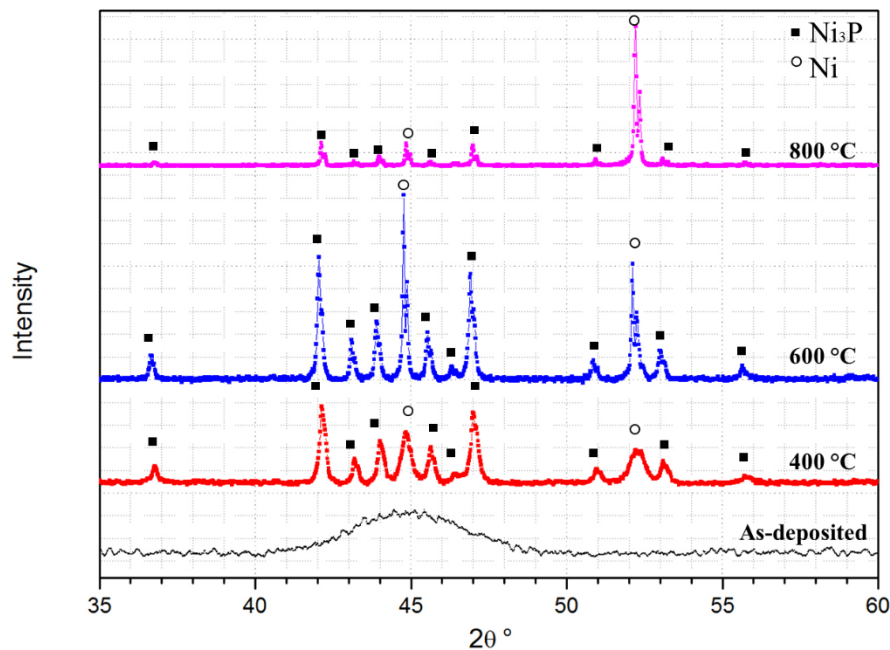
Figure 3-7 XRD patterns of electroless Ni-P coatings under different annealing temperature

The effect of annealing temperature on the microstructure of Ni-P-Ti coatings is also studied. The XRD patterns of the as-deposited and annealed Ni-P-Ti coatings are shown in Figure 3-8. The as-deposited Ni-P-Ti coating also has an amorphous peak at the 2θ position of 45°. Titanium peaks were not identified in the XRD pattern of the as-deposited Ni-P-Ti, which may be due to the low amount and the fine nano–size of the titanium particles. It is well known that nano-particles tend to have broad XRD peaks. The main peak of titanium is at the 2θ position of 40°, which overlaps with the peak of amorphous Ni-P coating. It is clear that annealing results in the crystallization of Ni and precipitation of Ni_3P. Similar results have been obtained in XRD analysis of plain Ni-P coating (Figure 3-7). Furthermore, there were no titanium related peaks observed at low annealing temperature (400°C). At high annealing temperature, however, the presence of Ni_3Ti was identified. Meanwhile, the addition of titanium particles affected the percentage of FCC nickel phase in Ni-P-Ti coatings. It has been confirmed by several researchers [31, 34, 36] that the amount of nickel and nickel phosphide vary with temperature. Keong [36] indicated that at low annealing temperatures under 500°C, the crystallization is not completed and there is still an amorphous phase in the Ni-P coating. The crystallization ends at 600-800°C and at 800°C the coating is completely crystallized. Therefore, in plain Ni-P coating, the percentage of crystalline phase increases with an increasing annealing temperature. Nevertheless, in Ni-P-Ti coatings, there were no significant changes in intensities of nickel and Ni_3P with the increasing temperature. The existence of titanium particles results in the formation of Ni_3Ti during annealing and retardation of nickel crystallization in high temperature annealed coatings.
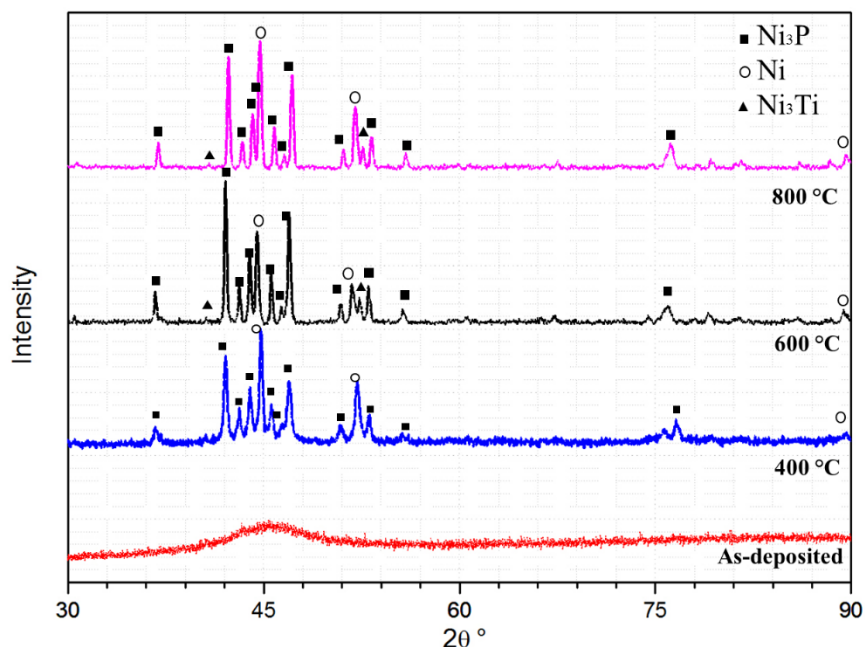
Figure 3-8 XRD patterns of electroless Ni-P-Ti coatings under different
annealing temperatures

3.1.4 Mechanical Properties

Mechanical properties such as hardness, Young's modulus and toughness of electroless Ni-P and Ni-P-Ti coatings were measured. Young' modulus and toughness were measured using three-point bending tests, and bend strength of bilayer systems and fracture strength of coatings are discussed as well.

3.1.4.1 Hardness

The Vickers hardness values of the as-deposited Ni-P coatings was found to be within a range of 4.5-6.0 GPa, which is in good agreement with published literature [10, 79-82]. On the other hand, Vickers hardness of the substrate under the same load was found to be 1.7 GPa. Thus, the results suggest that electroless Ni-P coating can greatly improve surface hardness of API steel.

The relationship between the Vickers hardness of Ni-P and Ni-P-Ti coatings and annealing temperature is examined. Vickers hardness of as-deposited and annealed Ni-P and coatings are summarized in Figure 3-9. The hardness is significantly influenced by the microstructure of the coating. It is found

that annealing increases the hardness due to phase transition [10, 18, 42]. The as-deposited coating, which has an amorphous structure, has a relatively low hardness. The hardness of Ni-P coating annealed at 400°C is found to be the highest (9.7 GPa) due to precipitation of nano-crystalline Ni_3P. With an increasing annealing temperature, the hardness of annealed Ni-P coating decreases. The increasing temperature raises the amount of crystalline Ni_3P and nickel phases in the coating, so do the grain sizes. The increasing percentage of crystalline nickel phase causes a drop in hardness and the coating annealed at a high temperature has a lower hardness than as-deposited coatings. At an annealing temperature of 800°C, the coating is fully crystallized, and it has a lower hardness than that of as-deposited coatings. In general, amorphous or semi-amorphous metallic materials have superior mechanical properties compared to their crystalline counterparts, due to the lack of dislocation and defects [83, 84].

The Vickers hardness of both as-deposited and annealed Ni-P-Ti coatings are shown in Figure 3-9. It was found that the as-deposited Ni-P-Ti coating has the lowest hardness of 6.68 GPa (HV 681), and it is higher than that of Ni-P coating. The hardness of annealed Ni-P-Ti coatings follows the same trend as that of annealed Ni-P coatings. The 400°C annealed Ni-P-Ti has the highest hardness of 12.63 (HV 1287) GPa. Similar to the Ni-P coating, the hardness of annealed Ni-P-Ti coating drops with increasing annealing temperatures. The increasing percentage of crystalline phases and the growth of the grain size may contribute greatly to the drop in the hardness with the increasing annealing temperature. Additionally, it is also found that the hardness of Ni-P-Ti coatings is higher than that of Ni-P coatings. As mentioned above, it was found that the 800°C annealed Ni-P coating has a lower hardness than as-deposited Ni-P coating. Nevertheless, the hardness of the 800°C annealed Ni-P-Ti coatings have a hardness of 8.3 GPa, which is much higher than as-deposited Ni-P and Ni-P-Ti coatings. The formation of Ni_3Ti reduced the percentage of crystalline nickel phase in high temperature annealed Ni-P-Ti

coatings. The absence of crystalline nickel phase results in the increase of hardness of high temperature annealed Ni-P-Ti coating.
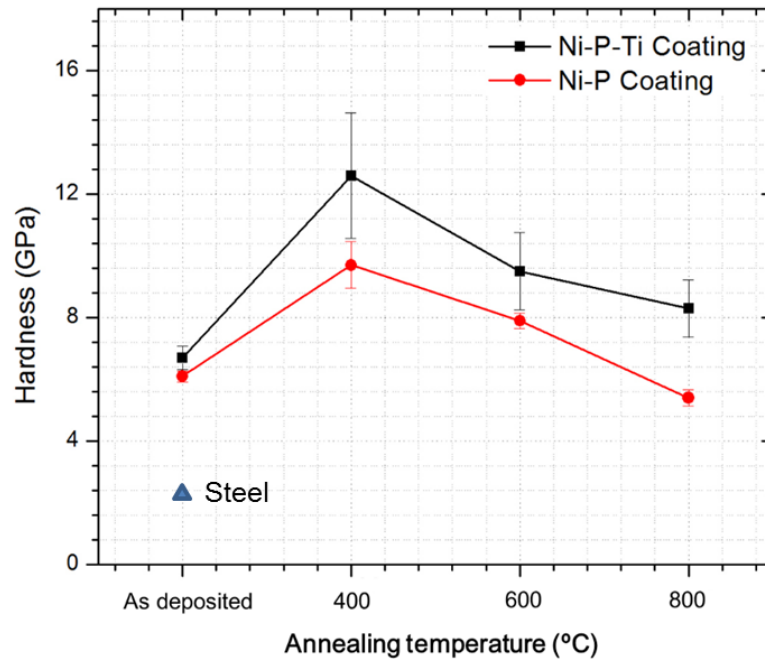
Figure 3-9 Hardness of Ni-P and Ni-P-Ti coatings as a function of annealing temperature

3.1.4.2 Young's Modulus

To measure Young's modulus and toughness of electroless Ni-P and Ni-P-Ti coatings, three-point bending tests were conducted on the substrate and as-deposited and annealed coatings. An acoustic emission detection system was used to monitor acoustic energy changes associated with crack initiation during bending. Figure 3-10 shows the force-displacement curve and acoustic emission data of the as-deposited Ni-P coating and steel substrate. When a crack forms, the acoustic emission sensor registers a spike in energy. The force required to initiate the crack can be estimated by superimposing the force-displacement and acoustic emission curves.
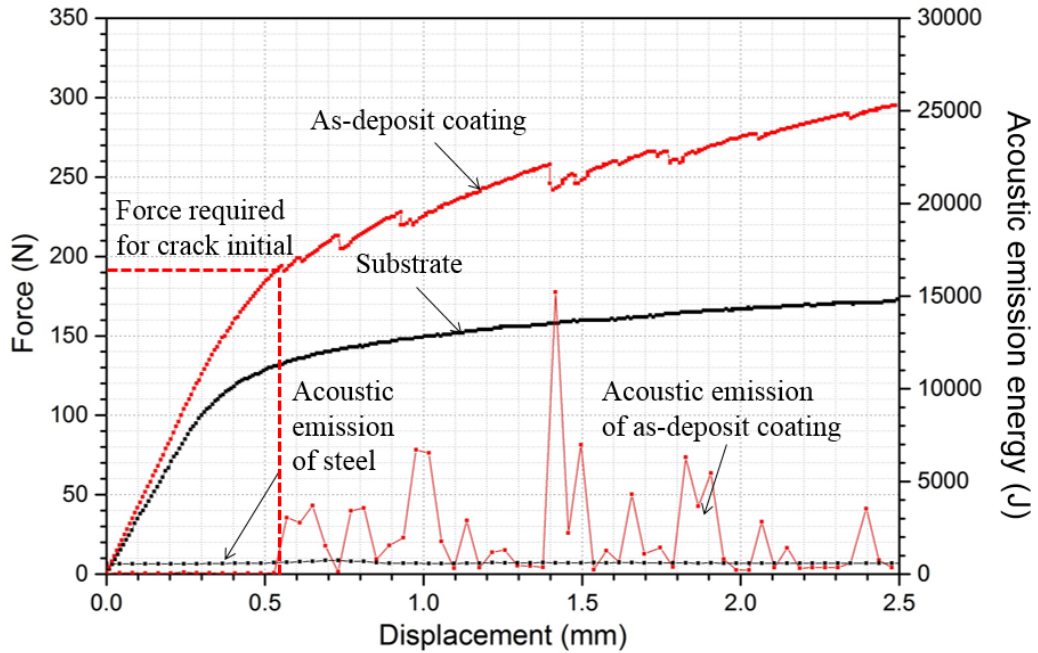
Figure 3-10 Force-displacement curve and acoustic emission data collected during bend tests of as-deposited Ni-P coating and substrate

From the curves in Figure 3-10, it is evident that the as-deposited Ni-P coating significantly increases the force required to induce a given deflection, as compared to the steel substrate. In comparison to the "smooth" curve of the steel substrate, the bending curve of the as-deposited coating is relatively noisy. According to the acoustic emission data, the acoustic emission energy of the substrate released during bending is minimal and constant. However, for as-deposited Ni-P coating, the localized drop in bending force associated with acoustic energy spikes provides evidence of crack formation. The first peak of acoustic energy, which occurs at a deflection of 0.54 mm and under a force of 188N, indicates the initiation of the first crack in the Ni-P coating.
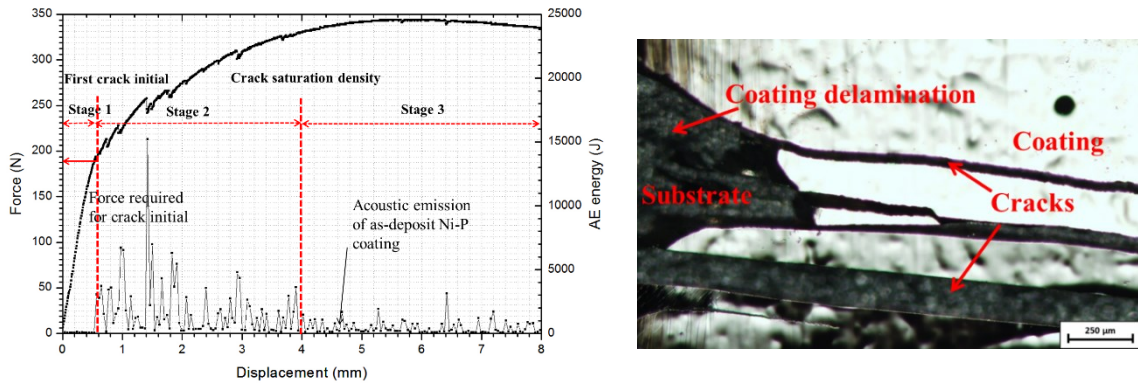
Figure 3-11 Different Stages of as-deposited Ni-P coating failure process during bending; (b) cracks and coating delamination of as-deposited Ni-P coating

By examining the optical microscopy and acoustic emission data of the cracked coating during bending, a Ni-P coating failure process is proposed and outlined next. The failure process is divided into three stages [85, 86], shown in Figure 3-11 (a). In the first stage, the Ni-P coating shows no cracks. And there was no acoustic emission data collected. With an increase in the applied tensile bending force on the bottom surface, a crack forms and a drop in bending force can be observed. The initiation of the first crack is associated with the first peak in acoustic emission energy. After the initiation of the first crack, more cracks form on the coating during the second stage. With the generation of these cracks, the distance between any two consecutive cracks decreases. With increased loading, the crack density (i.e. the number of cracks over a given length) reaches a constant maximum value, known as the crack saturation density. Once crack saturation density is reached, no more cracks are generated. Between the generation of the first crack and when cracks reach saturation density, large number of cracks propagate in a very short time. So the acoustic emission energy show many sharp peaks in stage 2. As deformation continues, cracks grow into the coating and propagate along the coating/substrate interface, giving rise to

65

delamination (stage 3) (Figure 3-11 (b)). And in this stage, the acoustic emission energy curve is relatively smooth with very few spikes.
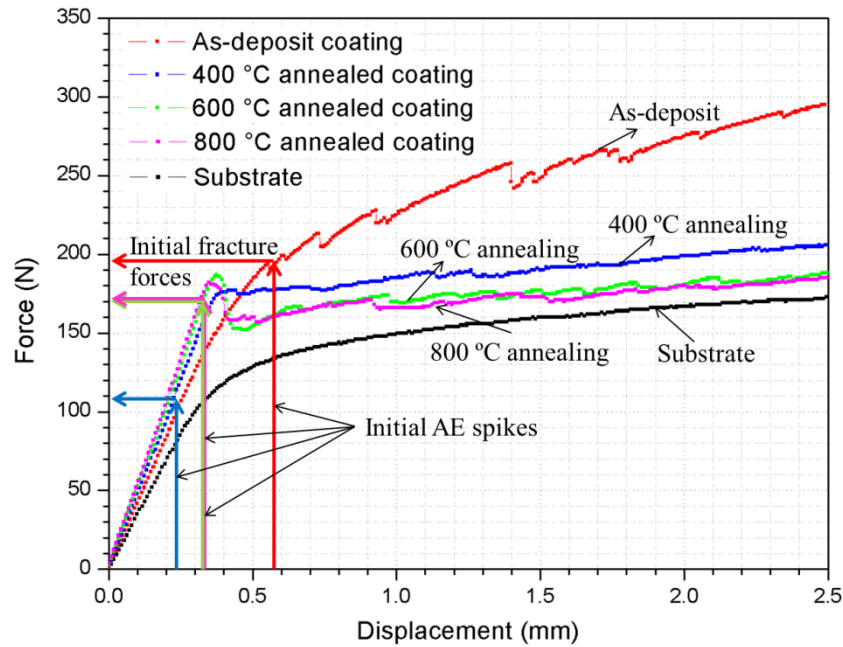
Figure 3-12 Force-displacement curve and fracture force associated with acoustic emission of substrate and Ni-P coatings annealed at different temperatures

Similarly, the effects of annealing temperature on bending behaviour were also evaluated. Figure 3-12 illustrates the load–displacement curves obtained from three-point bending tests. The slope of the elastic deformation in the force-displacement curve is related to the Young's modulus. In correlation with increasing annealing temperature, the slope of the elastic deformation (in the force-displacement curve) increases as well, indicating a rise in the Young's modulus of electroless Ni-P coating during the annealing process. Using the acoustic emission data, the force that initiated the first crack (initial fracture force) was measured and marked in Figure 3-12. It can be observed that the fracture force, which is related to the facture strength of the annealed specimens, is much lower than that of the as-deposited coating. Additionally, only the as-deposited coating exhibits a sudden drop in the bending force. Meanwhile, it can be observed that the bend strength of the

66

coating decreases post-annealing. The relationship between the hardness, toughness and fracture strength of the specimens are discussed in next section.
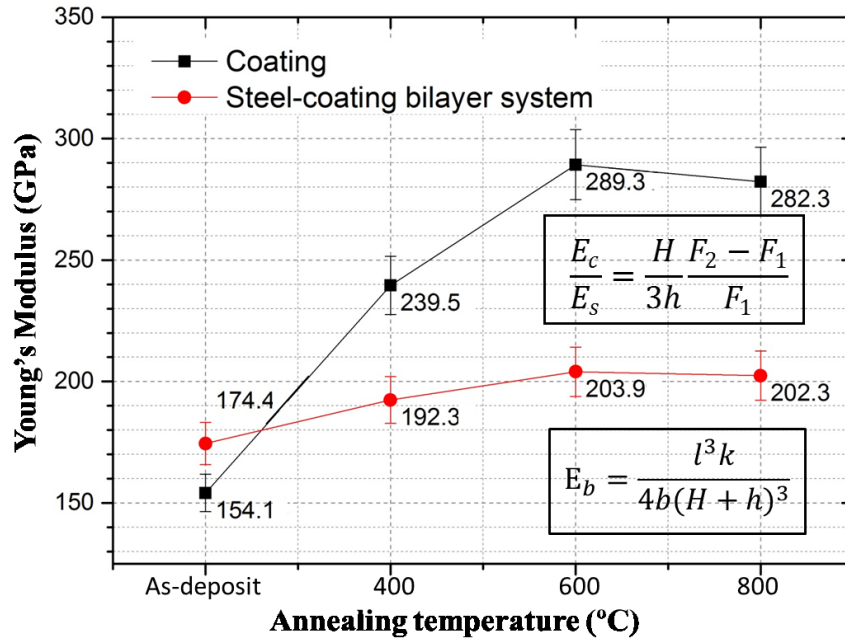
Figure 3-13 Young's modulus of Ni-P coatings and bilayer systems as a function of annealing temperature

The Young's moduli of as-deposited and annealed Ni-P coatings, are calculated using Equation 26 and 32 as shown in Figure 3-13. The Young's modulus of the coating was found to increase significantly because of phase transitions during annealing. Generally, amorphous or semi-amorphous metallic materials exhibit lower Young's modulus compared with crystalline metals [87, 88]. Crystallization during annealing is attributed to the partial removal of the plastic instabilities in as-deposited Ni-P coating [18]. Coatings annealed at a high temperature exhibit higher Young's modulus than those annealed at a low temperature, due to the rise in crystallization with annealing temperatures. For annealing temperatures higher than 600°C, the Young's modulus appears to remain constant, as the semi-amorphous nickel matrix becomes fully crystallized. The Young's modulus of the annealed bilayer is found to be higher than that of the steel substrate.

The Young's moduli of as-deposited and annealed Ni-P-Ti coatings was also investigated using three-point bending tests. Similar to electroless Ni-P coatings, acoustic emission energy changes during bending and these changes were detected using an acoustic emission detection system. The force initiated the first crack was also measured by superimposing the force-displacement and acoustic emission curves. To study the effect of titanium powder on the bending behaviour of the Ni-P coating, plain as-deposited Ni-P coating was also tested. Figure 3-14 shows the force-displacement curves and acoustic emission data of the substrate and as-deposited Ni-P and Ni-P-Ti coatings. Compared to the steel substrate, it is evident that both as-deposited Ni-P and Ni-P-Ti coatings increase the required force to induce a given deflection.
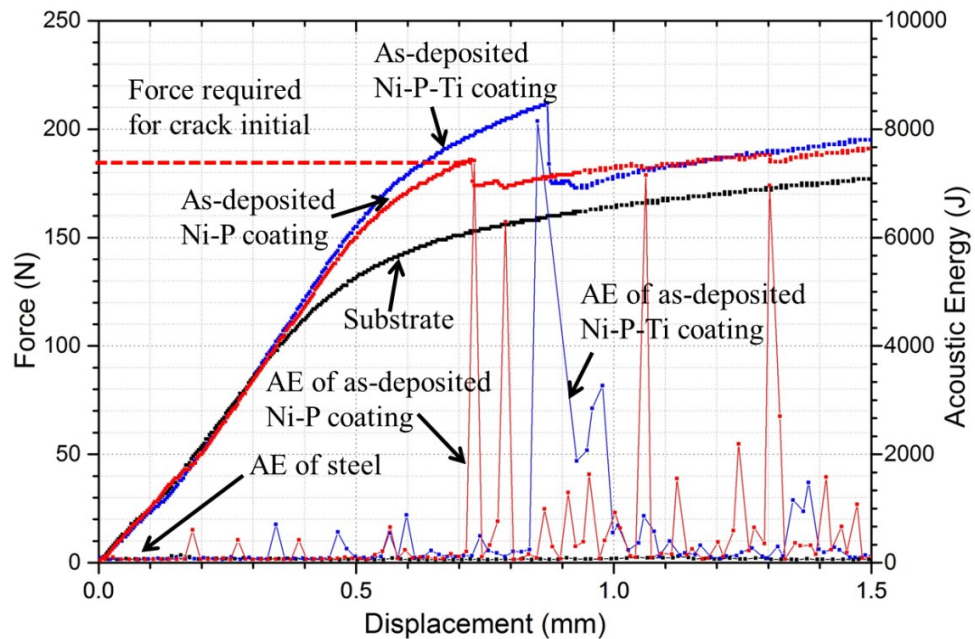
Figure 3-14 Force-displacement and acoustic emission data collected during bend tests of as-deposited Ni-P-based coatings and substrate

In Figure 3-14, a localized drop in bending force can be observed in both Ni-P and Ni-P-Ti coatings. This drop is associated with acoustic energy spikes, providing evidence of crack formation. It can be observed that both Ni-P and Ni-P-Ti coatings have similar elastic behaviour, but the required force for

crack initiation for Ni-P-Ti is higher than that of Ni-P coating. In addition, the deflection of Ni-P-Ti coatings (where the crack happens), is higher than that of Ni-P coatings as well.
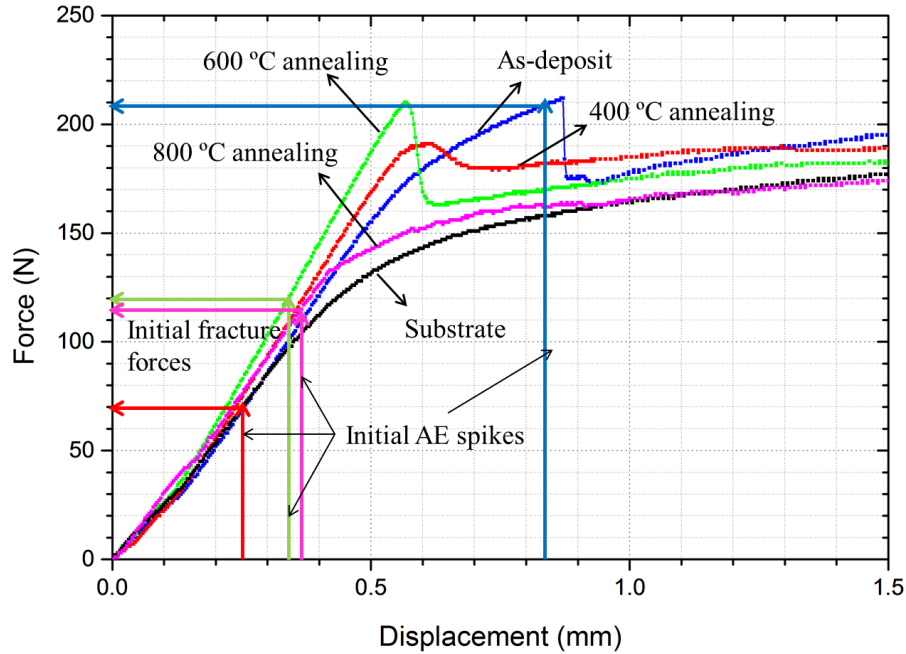
Figure 3-15 Force-displacement and fracture force associated with acoustic emission of bend tests on Ni-P-Ti coatings and substrate

The effect of annealing temperature on the bending behaviour of Ni-P-Ti coating is evaluated. Figure 3-15 illustrates the load–displacement curves of as-deposited and annealed Ni-P-Ti coatings recorded through three-point bending tests. The force that initiated the first crack (initial fracture force) was measured with the help of the acoustic emission energy changes, as shown in Figure 3-15.
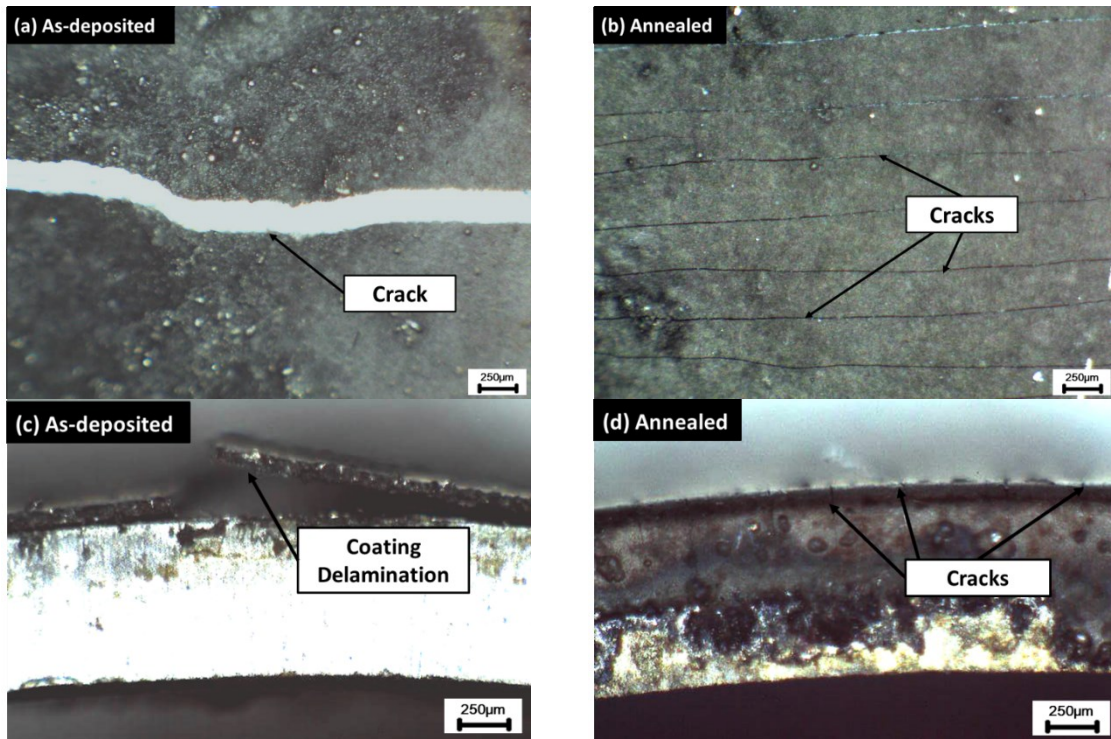
Figure 3-16 Cracks after bend tests on (a) (c) as-deposited Ni-P-Ti and (b (d)) 800 ℃ annealed Ni-P-Ti coatings

From Figure 3-15, it can be observed that only the as-deposited coating exhibits a sudden drop in the bending force after generation of cracks. To investigate the fracture morphology of as-deposited and annealed Ni-P-Ti coating, specimens were observed using an optical microscope. A large crack and coating delamination can be observed on the as-deposited coating (Figure 3-16 (a)). From cross-sectional view of the bending specimen, coating delamination was observed on the as-deposited coating (Figure 3-16 (c)). The delamination is associated with the drop of bending force in force-displacement curves in Figure 3-15. In comparison to the as-deposited coating, no large cracks were observed on the annealed coatings and some fine cracks formed on the bending specimens (Figure 3-16 (b)(d)). The crack morphology of Ni-P-Ti coating indicates that diffusion may have occurred on the interface during annealing, and resulted in increasing interface strength of the Ni-P-Ti coating.

The slope of the elastic deformation in the force-displacement curve is related to Young's modulus. The Young's modulus calculated using Equation 32 is summarized and discussed in Figure 3-17.

The equation shown in the figure:

$$\frac{E_c}{E_s} = \frac{H}{3h}\frac{F_2 - F_1}{F_1}$$
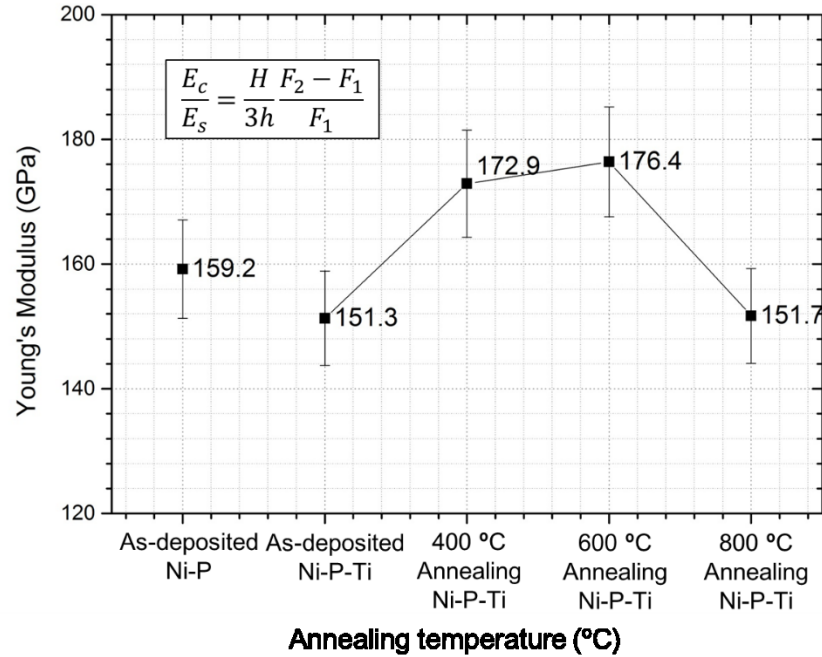
Figure 3-17 Young's modulus of Ni-P-Ti coatings as a function of annealing temperature

The Young's moduli of the substrate, Ni-P and Ni-P-Ti coatings are shown in Figure 3-17. The Young's moduli of the as-deposited Ni-P and Ni-P-Ti coating is found to be similar within a small margin of error. On the other hand, the effect of the annealing on the Young's modulus is more significant. Coatings annealed at 400 and 600°C exhibit higher Young's moduli because of phase transitions during annealing. Generally, amorphous or semi-amorphous metallic materials exhibit lower Young's modulus compared with crystalline metals [87, 88]. Crystallization during annealing is attributed to the partial removal of the plastic instabilities in as-deposited Ni-P coating [18]. The Young's modulus appears to decrease at an annealing temperature of 800°C.

3.1.4.3 Toughness
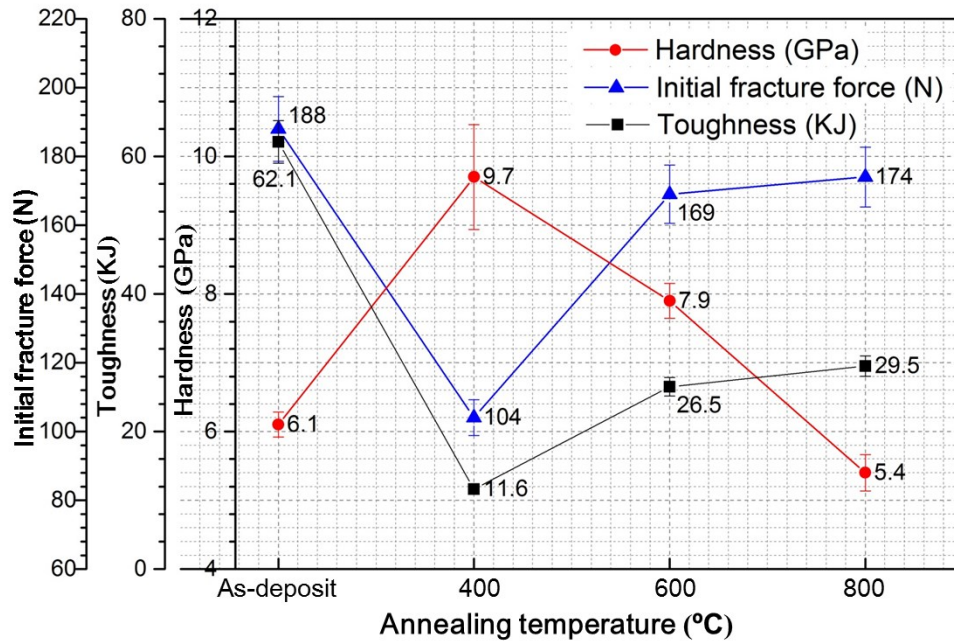
Figure 3-18 Toughness, fracture force and hardness of Ni-P coatings annealed at different temperatures

Toughness was also calculated from the force-displacement curves (Figure 3-12), using the area under the bending curve from the start of the bend test to the first crack initiation. It is found that the force required to initiate the first crack is highly dependent on the hardness and microstructure of annealed coatings. The trend in the variation of the initial fracture force, as a function of annealing temperatures, is opposite to that of the hardness, as shown in Figure 3-18. On the other hand, the 400°C annealed specimen, which has the highest hardness, was found to have the lowest initial cracking force at 104N. The as-deposited Ni-P coating exhibits the highest initial cracking force. These results suggest that annealing increases the brittleness of Ni-P coating, with the 400°C annealed coating being the most brittle coating. The toughness calculated based on fracture force, has a similar trend to that of fracture force. The 400°C annealed coating was found to have the lowest toughness, while the as-deposited coating exhibited the highest.

According to the XRD data, the dominant phase in the 400°C annealed coating is Ni$_3$P with relatively small grain sizes. This microstructure has a high hardness, but lower toughness. Furthermore, the lower toughness in the 400°C annealed Ni-P coating makes cracks form easier (low initial fracture force). Coatings annealed at higher temperatures contain a higher percentage of crystalline nickel phase than Ni$_3$P phase. The high nickel percentage decreases the hardness of the coating and decreases the brittleness, as indicated by the rise in toughness and high initial fracture force. Comparatively, the semi-amorphous microstructure of as-deposited Ni-P coating is characterized by low hardness and high toughness.

$$\sigma_b = \frac{3PL}{2b(H + h)^2}$$
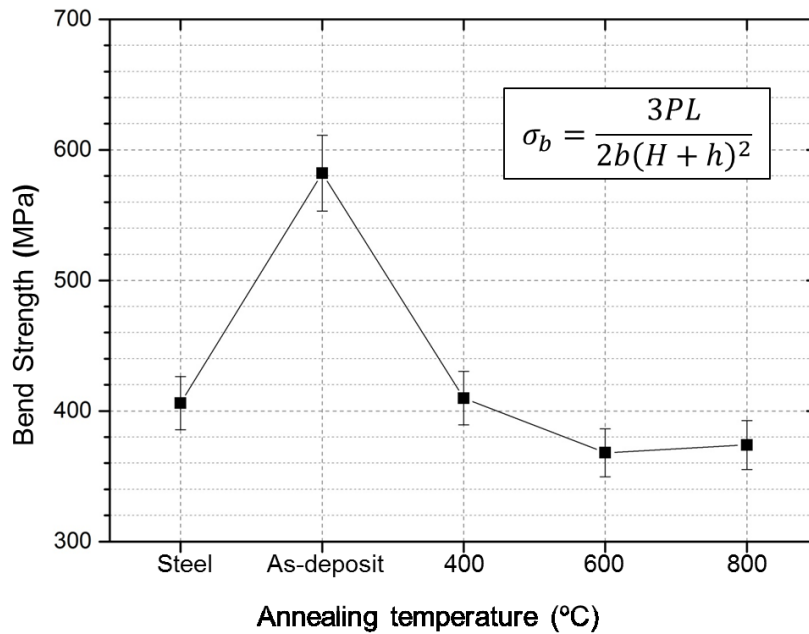
Figure 3-19 Bend strength of steel and Ni-P coatings as a function of annealing temperature

In Figure 3-19, bend strength of substrate and Ni-P coatings bilayer system is calculated using Equation 19. The 'P' in the equation is the force applied to cause same deflection at 2.5mm of each specimens. Here, it can be observed that the as-deposited Ni-P coating significantly increases the bend strength of the steel. However, annealed coatings exhibit a drop in the bend strength of the steel. The bend strength of bilayer system annealed at 600

and 800ºC drops significantly, indicating that under these conditions, Ni-P coatings are less capable of supporting the steel substrate during bending. Bend strength of the Ni-P coating annealed at 400ºC is only slightly lower than that of the substrate. High bend strength of the as-deposited coating is due to its high toughness.

The graph shows fracture strength (MPa) versus annealing temperature with the equation:

$$\sigma_f = \frac{E_c}{E_s} \frac{F \times L/2 \times h/2}{2I}$$
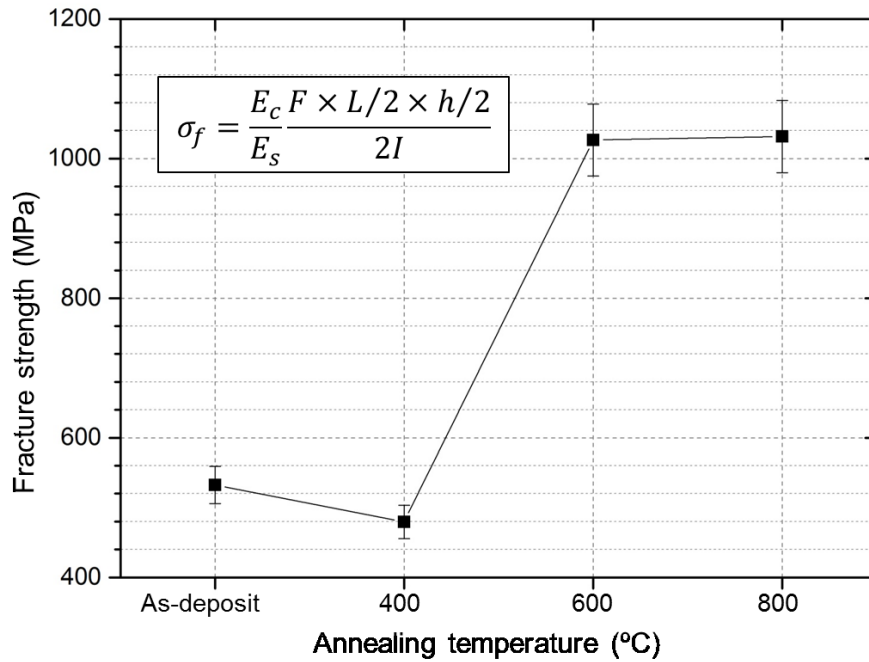
Figure 3-20 Fracture strength of Ni-P coatings as a function of annealing temperature

Fracture strength is a commonly used property in assessing brittle materials and it is well known that the fracture strength of brittle materials is characterized by a large variability [89]. Fracture strength is sensitive to size, shape, loading rate and test environment [90]. Different methodologies have been developed for measuring the fracture strength and most of these methods equate the fracture strength to the flexural stress at fracture. Fracture strength, in this study, is calculated using Equation 34 and the force used to calculate the fracture strength is the initial fracture force (Figure 3-20). The coating was found to exhibit high fracture strength when annealed at a high temperature. The effect of the annealing temperature on the fracture strength can be explained by the change in the microstructure of

the coating. The coating with a Ni₃P microstructure, at an annealing temperature of 400°C, is the most brittle and has the lowest fracture strength. The as-deposited coating, however, has relatively low fracture strength due to its low Young's modulus.
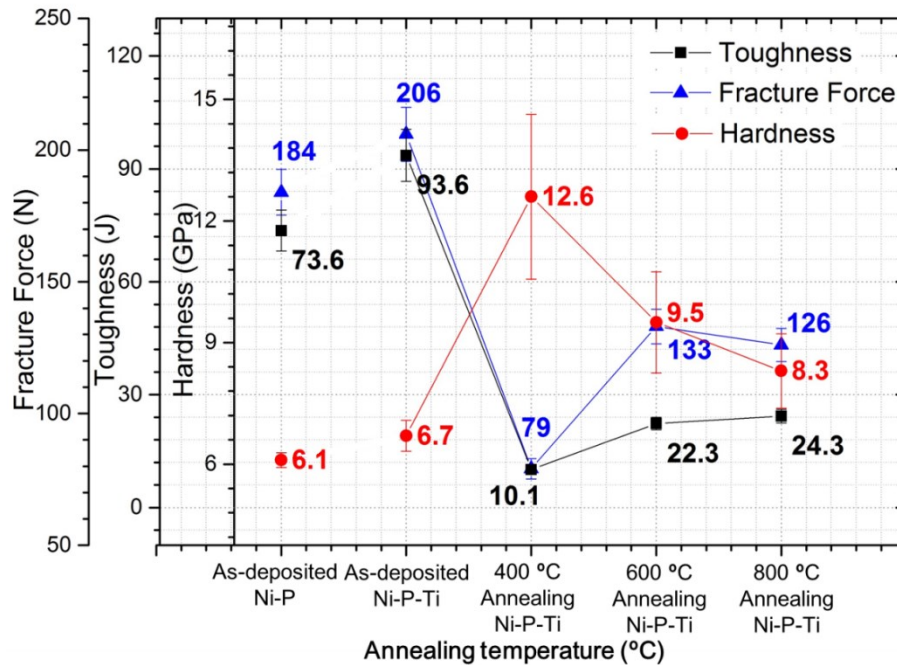
Figure 3-21 Toughness, fracture force and hardness of Ni-P-Ti coatings annealed at different temperatures

The toughness of as-deposited and annealed Ni-P-Ti coatings were calculated in the same way as Ni-P coatings, integrating the area under the curve from the start of the bend test until the first crack initiation. Similar to Ni-P coating, the fracture forces of annealed coatings are lower than those of as-deposited coatings. Figure 3-21 shows the relationship of toughness, fracture force and hardness for both Ni-P and Ni-P-Ti coating. Comparing as-deposited Ni-P with Ni-P-Ti coatings, it is found that the addition of titanium particles in the coating increases the hardness, fracture force and toughness. It is evident that the fracture force is highly dependent on the hardness and microstructure of Ni-P and Ni-P-Ti coatings. Both as-deposited Ni-P and Ni-P-Ti coatings have higher toughness compared to the annealed coatings due

75

to the semi-amorphous structure of as-deposited coatings. The trend in the initial fracture force, as a function of annealing temperatures, is opposite to that of hardness, as shown in Figure 3-21. The 400°C annealed specimen, which has the highest hardness, has the lowest initial cracking force and toughness. These results suggest that annealing increases the brittleness of Ni-P-Ti coating, with the 400°C annealed coating being the most brittle coating.

The relationship between the hardness and toughness of Ni-P and Ni-P-Ti coating is related to microstructural transitions in the coating during annealing. The semi-amorphous microstructures of as-deposited Ni-P and Ni-P-Ti coatings are characterized by low hardness and high toughness. In the 400°C annealed coating, nickel phosphide is the dominant phase. The nickel phosphide XRD peak is broad compared to coatings annealed at higher temperatures, which indicates that a 400°C annealed coating has relatively small grain sizes. This microstructure has a high hardness, but lower toughness. Coatings annealed at temperatures of 600 and 800°C contain nickel, Ni_3P and Ni_3Ti and they are well crystalized. The structure causes the drop in hardness, but a slight increase in toughness.

The figure shows a plot of Bend Strength (MPa) on the y-axis (ranging from 300 to 420) versus Annealing temperature (°C) on the x-axis with data points:

- Steel: 366
- As-deposited Ni-P: 374
- As-deposited Ni-P-Ti: 378
- 400 °C Annealing Ni-P-Ti: 364
- 600 °C Annealing Ni-P-Ti: 347
- 800 °C Annealing Ni-P-Ti: 334

$$\sigma_b = \frac{3PL}{2b(H+h)^2}$$
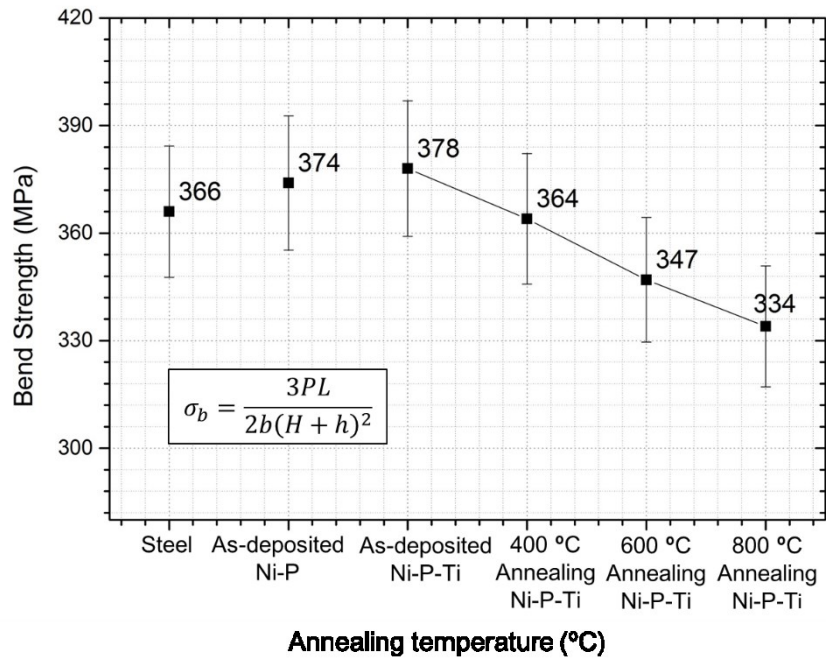
Figure 3-22 Bend strength of steel and Ni-P and Ni-P-Ti bilayer systems as a function of annealing temperatures

In Figure 3-22, it can be observed that the as-deposited Ni-P-Ti coating increases the bend strength of the steel. However, the annealed coatings exhibit a drop in the bilayer bend strength. The formation of nickel phosphide phase during annealing results in a drop of toughness and causes a drop in bend strength.

77
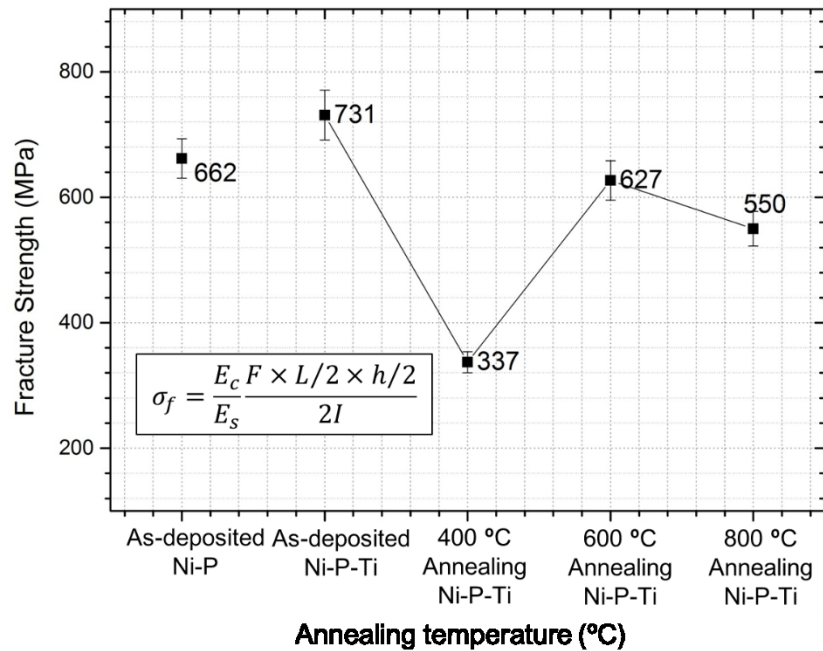
Figure 3-23 Fracture strength of Ni-P-Ti coatings as a function of annealing temperature

Fracture strength, is calculated using Equation 34 and the force used to calculate the fracture strength is the initial fracture force. The effect of the annealing temperature on fracture strength can be explained by the change in the microstructure of the coating. The as-deposited coating was found to exhibit high fracture strength due to the high toughness of its amorphous structure. The coating annealed at of 400°C are the most brittle and have the lowest fracture strength due to the nano-crystalline structure. High temperature annealed coatings which are fully crystallized and contain Ni_3Ti particles, have higher toughness.

In summary, the effect of titanium particles on mechanical properties of as-deposited coatings, as well as the effect of annealing temperature on mechanical properties of Ni-P and Ni-P-Ti coatings were studied. The results are summarized in Table 3-4. Comparing the as-deposited Ni-P and as-deposited Ni-P-Ti coatings reveals that the addition of the titanium can increase the hardness, toughness, fracture strength of the coating and bend strength of the bilayer system. However, it decreases the Young's modulus.

78

The effect of annealing temperature is also shown in Table 3-4. The effects of annealing temperature on Ni-P and Ni-P-Ti are similar. As mentioned above, with an increasing temperature, the percentage of crystalline phases in the coating increases, as well as the grain size. The change in microstructure causes a drop in hardness, but it increases toughness and fracture strength of the coating. Young's moduli of Ni-P and Ni-P-Ti coatings also increases with annealing temperatures. In general, annealed Ni-P and Ni-P-Ti coatings have higher hardness, higher Young's modulus and lower toughness than that of as-deposited Ni-P and Ni-P-Ti coatings due to the semi-amorphous microstructure of as-deposited coatings.

Table 3-4 Effect of titanium particles and annealing temperature

	Hardness	Young's modulus	Toughness	Fracture strength	Bend strength of the bilayer system
The addition of titanium particles	↑	↓	↑	↑	↑
Low temperature annealing vs as-deposited coatings	↑	↑	↓	↓	↓
Low temperature annealing vs high temperature annealing coatings	↓	↑	↑	↑	↓

3.2 Indentation Behaviour

In this section, indentation behaviour of electroless Ni-P and Ni-P-Ti coatings are discussed. The effect of coating thickness, load and annealing temperature on indentation behaviour of Ni-P coating are investigated. Indentation morphology and cracking damage of Ni-P coatings with different thicknesses under different loading conditions were analyzed. For Ni-P-Ti composited coatings, the effect of annealing temperature on indentation behavior of coatings with a thickness around 100 µm under a load of 1500N was studied.

3.2.1 Indentation Behaviour of Ni-P Coatings

Indentation behaviour of plain Ni-P coatings is discussed. Substrate and as-deposited Ni-P coatings with 3 different thickness, namely 18, 63, 105 μm were tested. Moreover, dent resistance of Ni-P coatings annealed at 400, 600 and 800 ºC was investigated as well.

3.2.1.1 Effect of Coating Thickness

To investigate the indentation behaviour of electroless Ni-P coating, indentation morphology and cracking damage of coatings with different thicknesses under different loading conditions were examined. Each specimen was tested using 600, 1000, 1500, 2000 and 2500N load. The surface and cross-section morphologies of Ni-P coatings with different thickness under different loads are summarized in appendix (Table A-0-1).

Figure 3-24 shows the depth-load curve of 18 μm, 63 μm and 105 μm coatings under 1000N and 2000N loads, respectively. It is interesting to note that, the maximum indentation depths of coatings are higher than the substrate. Maximum indentation depths are 331 and 337 μm under 2000N for the substrate and the thin coatings, and 380 and 389 μm for intermediate and thick coatings, respectively. Figure 3-25 (a) shows cross-sectional view of indentation of 105 μm coating under 2500N load. It was observed that under indentation load the coating was compressed and pushed to the edges of contact. No coating was observed on the substrate at the center of the indent, resulting in high indentation depth. With increasing coating thickness the indentation depth increases as coating is removed to the sides of the indent. To further validate this observation, the fracture pattern on the coating was examined. Figure 3-25 (b) shows a FIB circle on the cross-section. Here, it is observed that, the coating cracked and the circle is split into two parts. The upper part appears compressed and is squeezed to the edge of indentation. The FIB circle confirms that the coating being pushed to the edge of contact is the reason for larger indentation depth with increasing thickness. This

phenomenon is less pronounced at low loads as can be seen from max indentation depth of indentation under 1000N (Figure 3-24).
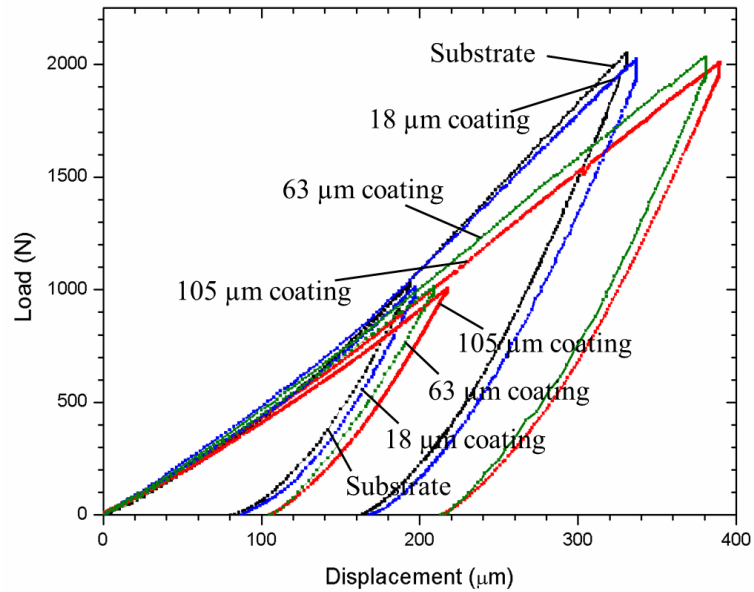
Figure 3-24 Displacement-load curves of substrate, 18 μm, 63 μm and 105 μm coatings
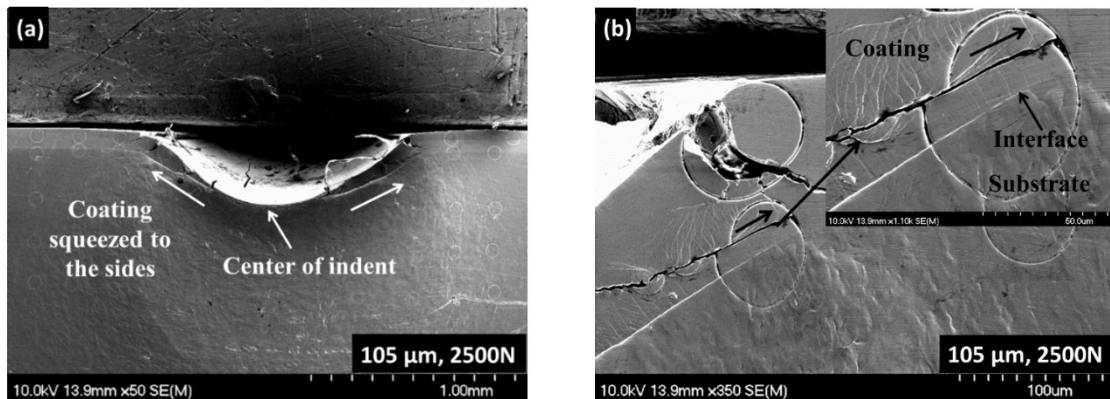
Figure 3-25 SEM micrographs of (a) cross-sectional view of indentation and FIB circles under a load of 2500N (b) FIB circles showing coating being sheared under a load of 2500N.

In this study, the 18 μm coating is classified as thin coating. Coating with a thickness between 63 μm to 105 μm is classified as thick coating. Crack types of thin and thick coatings are summarized in Figure 3-26.

Thin coating

(a)

Pile-up

Coating

Pile-up

Substrate

Thick coating

(b)

Bend cracks

Radial cracks

Surface bend cracks

Coating

Hertzian cracks

Bottom bend cracks

Substrate

(c) 18 μm, 2000N

Coating delamination

Pile-up

250 μm

(d) 105 μm, 2000N

Bend crack

Radial crack

250 μm

(e) 18 μm, 2000N

Substrate material pile-up

Coating delamination

250 μm

(f) 105 μm, 2000N

Surface bend crack

Bottom bend crack

Hertzian crack

250 μm

Figure 3-26 (a)(b) schematics of crack types on thin and thick coatings, respectively; (c)(d) top view of indentation on thin and thick coating, respectively; (e)(f) cross-sectional view of indentation on thin and thick coatings, respectively; (g) SEM micrographs showing delamination of the thin coating; (h) SEM micrographs of fine surface cracks on the thick coating

1) Thin coating

Significant pile-up and coating delamination were observed on thin coating as shown in Figure 3-26 (c) and (e). Figure 3-26 (g) is SEM micrograph of crack morphology of 18 µm coating under 2000N load. Here, the coating is too thin to support the load, so it could be considered a membrane. The load is essentially supported by the substrate. Instead of cracks, plastic deformation of substrate and coating delamination are observed. The delamination of the coating is due to pile-up of the substrate at the edge of contact. The pile-up lifts the coating and results in decohesion and delamination followed by cracking near the edge of contact. The bending of the delaminated coating indicates that the thin coating exhibits some plasticity. It is also interesting to note that surface texture of the Ni-P coating follows that of the substrate.

2) Thick coating

With the increase of the coating thickness, the indentation morphology significantly changed. Figure 3-26 (d) (f) show micrographs of indentation on 105 µm coating under 2000N load. Hertzian, radial and bend cracks were

83

observed on the coating surface. Compared to thin coating, no pile-up was visible under optical microscopic examination. Surface of the coatings were smooth with fine circular patterns around indentation, which were identified as bend cracks in SEM observation.

As clearly seen in Figure 3-26 (d), radial cracks propagated from the edge of the contact zone. They propagate parallel to the axis of the load starting from the edge of the plastic impression left by the indenter, and extended outwards. Hertzian and bend cracks were observed in the cross-section of indentation in Figure 3-26 (f). For Hertzian crack, it was observed that the initial direction of the crack was 45 degrees from the surface. And it grew inwards into the contact zone as the load increased. Bottom bend cracks were found at the bottom surface of the coating, while surface bend cracks were found outside of the contact edge. SEM observation was employed to identify the damage mode of the fine circular cracks. Under high magnification, it is found that the fine cracks are bend cracks with a depth of 1-2 μm as shown in Figure 3-26 (h). Hertzian cracks were found to start at these cracks sites.

To summarize, based on the spherical indentation and FIB work, it can be concluded that the coating is brittle. The 105 μm thick coating shows sever cracks due to indentation (Figure 3-26 (d)). However, the 18 μm coating does not crack but it delaminates as a result of substrate pile-up (Figure 3-26 (e)). The reason that the 18 μm thick coating does not crack is because of its small thickness, which results in low stiffness and makes the coating more flexible. The 18 μm thick coating would bend like a membrane and subsequently fractures in a brittle manner (Figure 3-26 (g)). Furthermore, the FIB experiment confirms the brittle nature of the 105 μm coating as the FIB circles show minimal plastic deformation and features normally associated with brittle fracture (i.e. sharp fractures).

3.2.1.2 Effect of Annealing Temperature

To investigate the effect of annealing on indentation behaviour of electroless Ni-P coating, the indentation morphology and cracking damage were studied. Cracks types of as-deposited and annealed coatings at low and high annealing temperatures are summarized in Figure 3-27.
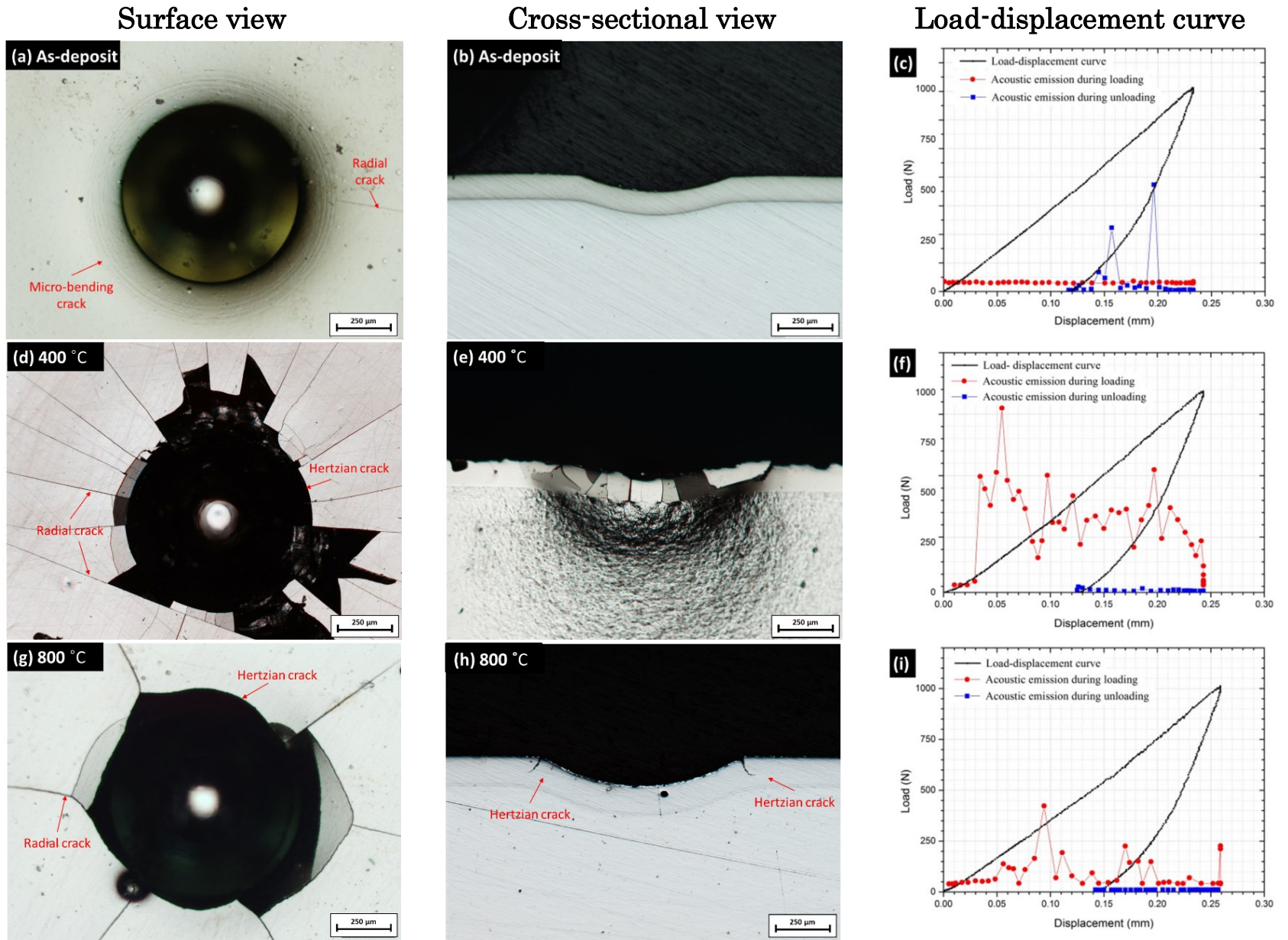
Figure 3-27 Indentation behaviour and load-displacement curves of specimen

Figure 3-27 (a) and (b) represent the top and cross-sectional views of the indentation on as-deposited Ni-P coating, while Figure 3-27 (c) represents the load-displacement curve of indentation. Radial and circular shaped cracks were observed on the plane of the coating, but no visible cracks were detected on the cross-section. This suggests that the circular cracks observed from the top view are not Hertzian cracks. As mentioned above, SEM observation identified these circular cracks to be micro-bend cracks. Changes in acoustic emission energy during loading and unloading are also presented (by the red dots and blue squares) in Figure 3-27 (c). Interestingly, according to the acoustic emission data, no cracks formed during loading. However, micro-bend and radial cracks were generated during unloading, under a load of 550N. The radial cracks may be caused by residual stresses in accordance with the expanding cavity model [91]. Robert and George [92] have found that the stress required to form a radial crack σ_{radial} is constant during loading and increases during unloading. This could explain why cracks formed during unloading. During the loading process, the radial stress is not high enough to initiate a radial crack, but increases during unloading. At a certain force, the radial stress reaches a critical value where radial cracks are generated.

As discussed above, the specimen annealed at 400°C was found to have the highest hardness and lowest toughness. Hertzian cracks and a high density of radial cracks were observed in the top view of the indentation impression, shown in Figure 3-27 (d). High density of bend cracks was also visible in the cross-sectional view. Figure 3-27 (f) shows the load-displacement curve and changes in acoustic emission energy during the indentation process. During unloading, there were no cracks generated. Crack initiation happened during loading, under a load of 110N, which is the lowest in comparison to specimens annealed at different temperatures. The acoustic emission peaks were higher than other annealing condition, which suggests that the fracture energy released during indentation of specimen annealed at 400°C was also

the highest. The acoustic emission analysis confirms that the coating annealed at 400°C has the lowest toughness and highest crack density.

The indentation views and load-displacement curve of the coating annealed at 800°C are shown in Figure 3-27 (g) (h) (i). Hertzian and radial cracks with lower crack density than those that formed on the coating annealed at 400°C are evident. In the cross-sectional view, only Hertzian cracks were observed. According to the acoustic emission data, during the loading process the force that initiated the crack was found to be 210N. The peak of acoustic emission energy was found to be lower than the coating annealed at 400°C.

In summary, annealing significantly changes the indentation behaviour of electroless Ni-P coatings. The as-deposited coating is more flexible and has a lower Young's modulus and hardness, which means it also has a lower resistance to deformation under load and can explain why there is no crack formation during loading. The annealed coatings, however, become more brittle due to phase transition. The Ni_3P phase increases the hardness and causes the drop in toughness. According to the bend test results, the toughness of the coating rises as the annealing temperature increases. The coating annealed at 400°C shows the lowest toughness, as it begins to crack under a load of only 110N. For a coating annealed at high temperatures, the percentage of Ni_3P in the coating decreases, which causes the decrease in hardness and the increase in toughness. Hence, the dent resistance of the coating increases and crack density drops.

3.2.2 Indentation Behaviour of Ni-P-Ti Coatings

The indentation morphology as well as the load-displacement curves of as-deposited annealed electroless Ni-P-Ti coatings are summarized in Figure 3-28. The acoustic emission associated with the crack propagation is also shown in Figure 3-28.

Hertzian and radial cracks are found on the as-deposited coating. Similar to bending cracks, the as-deposited coating has a low density of cracks. However, the cracks are larger. According to the acoustic emission data, cracks that appeared on the as-deposited coating released more energy than cracks on the annealed coatings. Interestingly, acoustic emission energy spikes were also recorded during unloading of the as-deposited Ni-P-Ti coating, which was not evident on annealed coatings. The radial cracks may be caused by residual stresses in accordance with the expanding cavity model [91]. This means more energy was absorbed and stored during loading because the high toughness of Ni-P-Ti coating. In the former study [4], it was found that there were no Hertzian cracks observed under load of 2000N and only micro-bend cracks were observed around the contact edge. The agglomeration of titanium particles in Ni-P-Ti coatings may results in premature localized failure during indentation.

Coatings annealed at temperatures of 400 and 600°C appears to have a high density of micro-cracks. According to the acoustic emission data, the sensor detected crack formation at a low load under 100N and energy spikes were detected during the loading process. The acoustic emission energy spikes are lower compared to as-deposited coatings. During unloading, there were no cracks generated. As previously discussed the specimen annealed at 400°C was found to have the highest hardness and lowest toughness, which explain the low indentation resistance of the annealed coatings.

The load-displacement curve and indentation views of the coating annealed at 800°C are shown in Figure 3-28 (d). The coating annealed at 800°C shows Hertzian and radial cracks of lower density compared to the coating annealed at 400 and 600°C. However, bend ring cracks away from the contact edge were also found on the surface. According to the acoustic emission data, an energy spike associated with the initiating crack force was

found at a load of 394N. Additionally, spikes released more energy than the energy spikes of the 400 and 600°C annealed coatings.
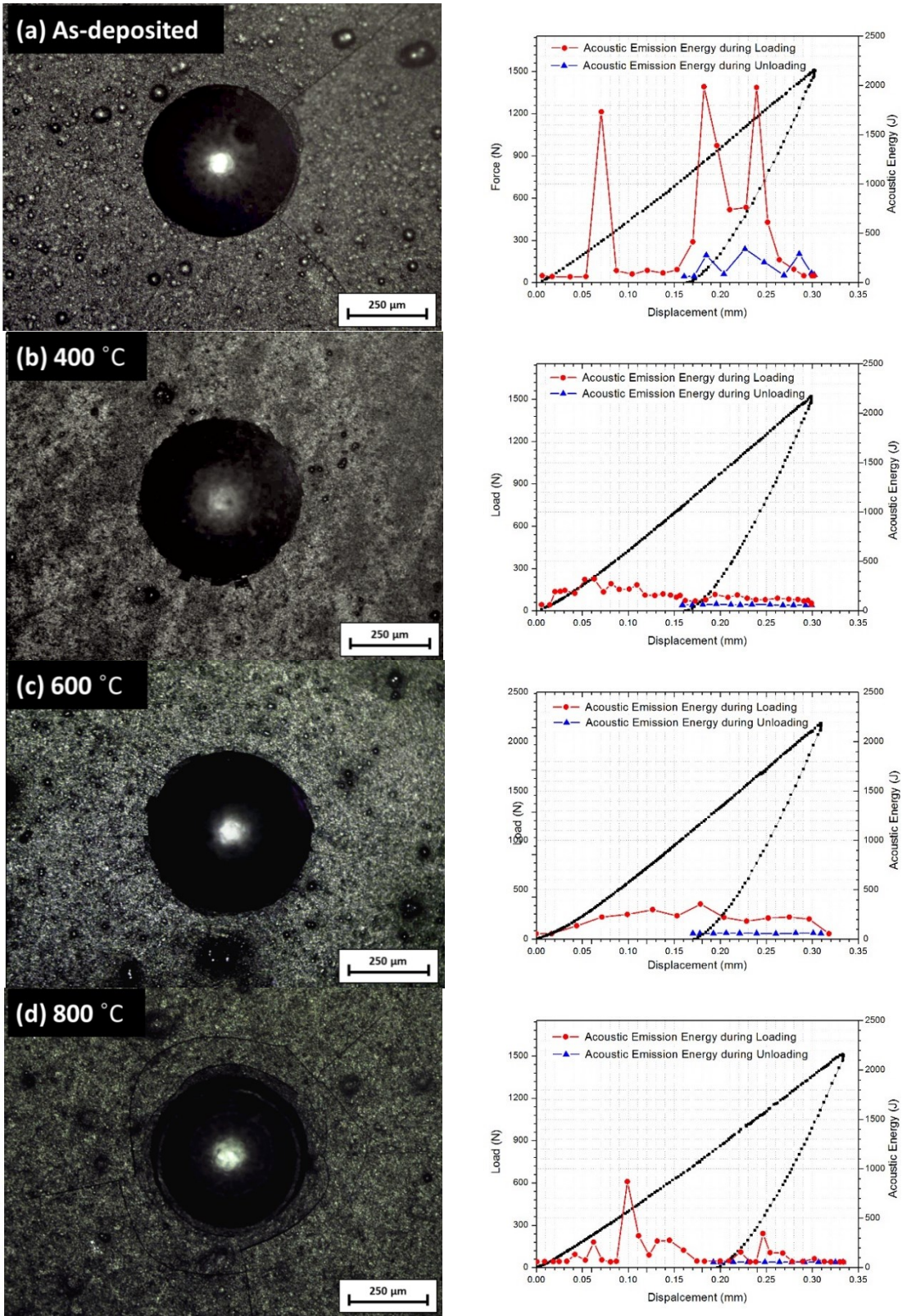
Figure 3-28 Indentation fracture and load-displacement curve of the as-deposited and annealed specimens

In summary, the effect of titanium particles on the indentation behaviour of the as-deposited Ni-P coating can be evaluated by comparing this study's results with the previous study [4]. Radial cracks and coating delamination were observed on Ni-P-Ti coating, while only micro-bend cracks were observed on Ni-P coating under a load of 1500N. Data from bend tests has indicated that adding titanium particles increases the bend strength and toughness, in general. However, the agglomeration of titanium particles may results in premature localized failure during indentation. The effect of annealing on the indentation behaviour of Ni-P-Ti coating was also studied. Annealing significantly changes the indentation behaviour of Ni-P-Ti coating. The as-deposited coating has the lowest hardness and the highest toughness. Annealing increases hardness and lowers toughness. The annealed coatings become more brittle due to phase transition and precipitation of hard Ni_3P particles. The coating annealed at 400 and 600°C formed to cracks under a load of 100N and showed a large density of micro-cracks. For coatings annealed at high temperatures, the changed percentage of crystalline nickel and nickel phosphide phase caused the decrease in hardness and increase in toughness. Hence, the dent resistance of the coating increases and crack density drops.

3.3 Erosion Behaviour of As-deposited Ni-P Coatings

The erosion resistance of as-deposited electroless Ni-P coating having a thickness of 105 μm was investigated. Effect of test duration and impact angle on weight loss of Ni-P coating and substrate API X100 steel were investigated.
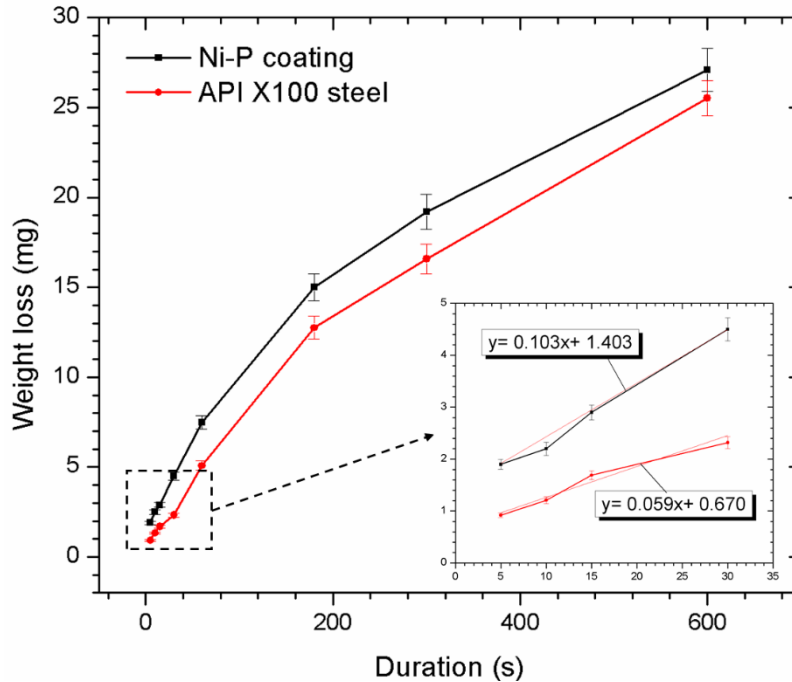
Figure 3-29 Weight loss versus duration for API X100 steel substrate and Ni-P coatings at 36m/s and 90°

Figure 3-29 is a plot of weight loss of electroless Ni-P coating and API X100 steel versus time. Specimens were eroded using a velocity of 36m/s for 5, 10, 15, 30, 60, 180, 300 and 600s at 90° impact angle. Both curves show similar trend and weight loss of the coating is slightly higher than the steel substrate. It is evident that after 60s, the slope of the curves gradually drops with increasing time. The cross-sectional views of eroded specimens were observed using SEM to assess coating integrity (Figure 3-30). SEM micrographs show that after 10s of erosion, the coating thickness dropped from 100µm to 65 µm (Figure 3-30 (a)), and after 30s, the depth of the erosion scar is the same as the coating thickness (Figure 3-30 (b)). Hence, coating material removal rate is found to be 3.2µm/s. When the erosion duration time rises over about 30 seconds, the erosion rate becomes a combination of contributions from both the coating and the substrate. This explains the similarity in both curves in Figure 3-29.

93

Figure 3-30 SEM micrographs of cross-sectional view of eroded specimens after (a) 10s and (b) 30s

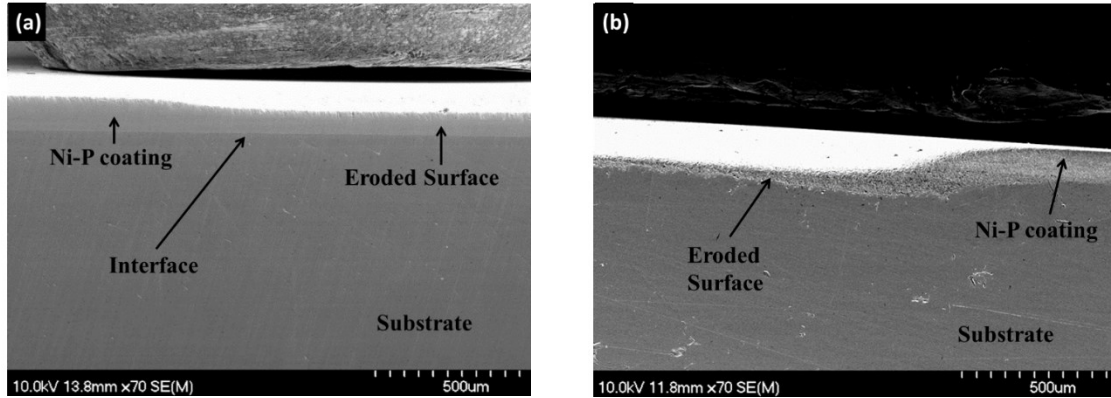Therefore, the erosion rate of electroless Ni-P coating was calculated using the weight loss of the specimen in the first 30 seconds. Erosion rate is measured from the slope of the weight loss versus time in the first 30 seconds. The normalized erosion rate was calculated by dividing erosion rate (mg/s) by the abrasive particle flow rate (mg/s). In this study, gas pressure was measured and particle velocity was determined as a function of pressure using a double-disc method [66]. And abrasive particle feed rate is accurately determined by measuring the weight of the abrasive particles coming through the nozzle per unit time and is constant for a given velocity. The gas pressure used in this study is 20 psi, and the particle velocity and abrasive particles feed rate in this case are 36 m/s and 2.1 g/s, respectively. Using Figure 3-29 and Equation 39, the normalized erosion rate of electroless Ni-P coating is determined as 0.49×10^{-4}. The erosion rate of the substrate API X100 steel is calculated in the same way, and it has a value of 0.28×10^{-4}. It is interesting to note that, the erosion rate of the coating is higher than the substrate. This may be attributed to the brittle nature of Ni-P coating compared to steel, which is discussed below.

The effect of impact angle on erosion resistance was investigated and is shown in Figure 3-31. Ni-P coating and API X100 steel substrate were eroded at 30°, 45°, 70° and 90° for 10s. It is evident that the weight loss of coated specimen significantly increases with increasing impact angle.

However, weight loss of API X100 steel is slightly higher at low angle of 30° and drops with increasing angle. The behaviour is consistent with a previous work for similar steel, which shows that at a relatively low particle velocity, the amount of erosion at low angle is slightly higher than 90° impact angle and increases with particle velocity [3]. Hutchings [73] proposed that the effect of impact angle on erosion rate depends on the ductility of the material. Ductile materials have a maximum erosion rate at low angles of incidence, while the maximum erosion rate is at or near 90° for brittle materials. For ductile material at low impact angle, ploughing and cutting actions dominate, and this results in high erosion [65, 67]. At high impact angle, brittle materials fracture and experience high material loss, whereas ductile materials experience heavy plastic deformation. From Figure 3-31, it can be concluded that Ni-P coating behaves in a brittle manner under the present current conditions.
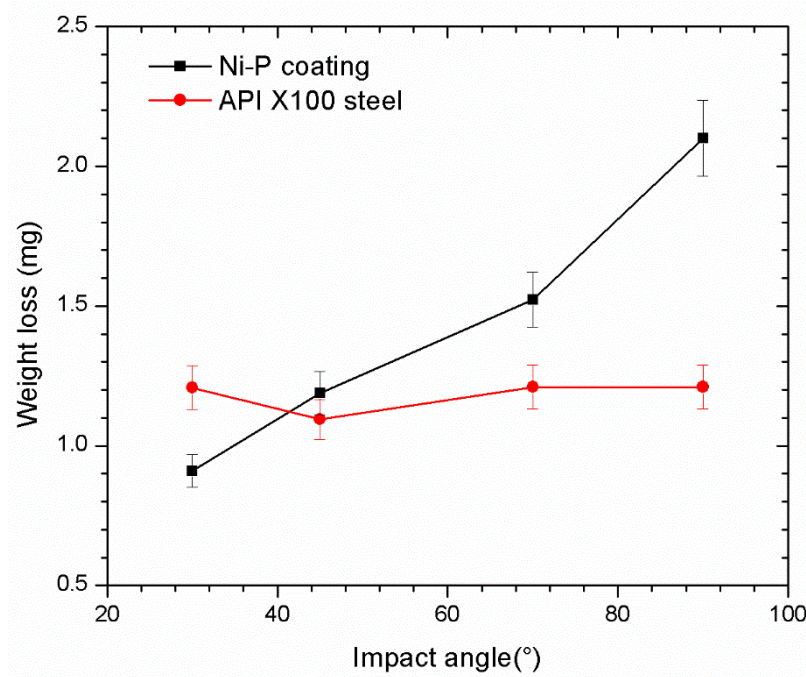

Figure 3-31 Weight loss versus angle for API X100 steel substrate and Ni-P coatings at 36m/s for 10s

To identify operative erosion mechanisms, SEM examination was carried out at the center of the erosion scar (heavily damaged region) and at the less

damaged regions. Generally, the erosion mechanism for brittle material is brittle fracture [13, 68], and at low velocities lateral and median cracks are commonly observed when using angular particles as erodent. Figure 3-32 (a) and (b) show erosion scar and brittle fracture on the surface of the 10s eroded specimen. It is evident that penetration and removal of abrasive particles has occurred on the surface of the 30s eroded specimen as shown in Figure 3-32 (c) and (d). Penetration and removal of abrasive particles are normally observed in the erosion of the ductile materials. Aminul et al. [3] found that for API series pipeline steel, most of the abrasive particles kinetic energy is used to penetrate the surface resulting in dimple formation and penetration by solid particles at high impact angle (90°) and low particle speed (36 m/s). The abrasive particles seem to break the coating and embed in the substrate.
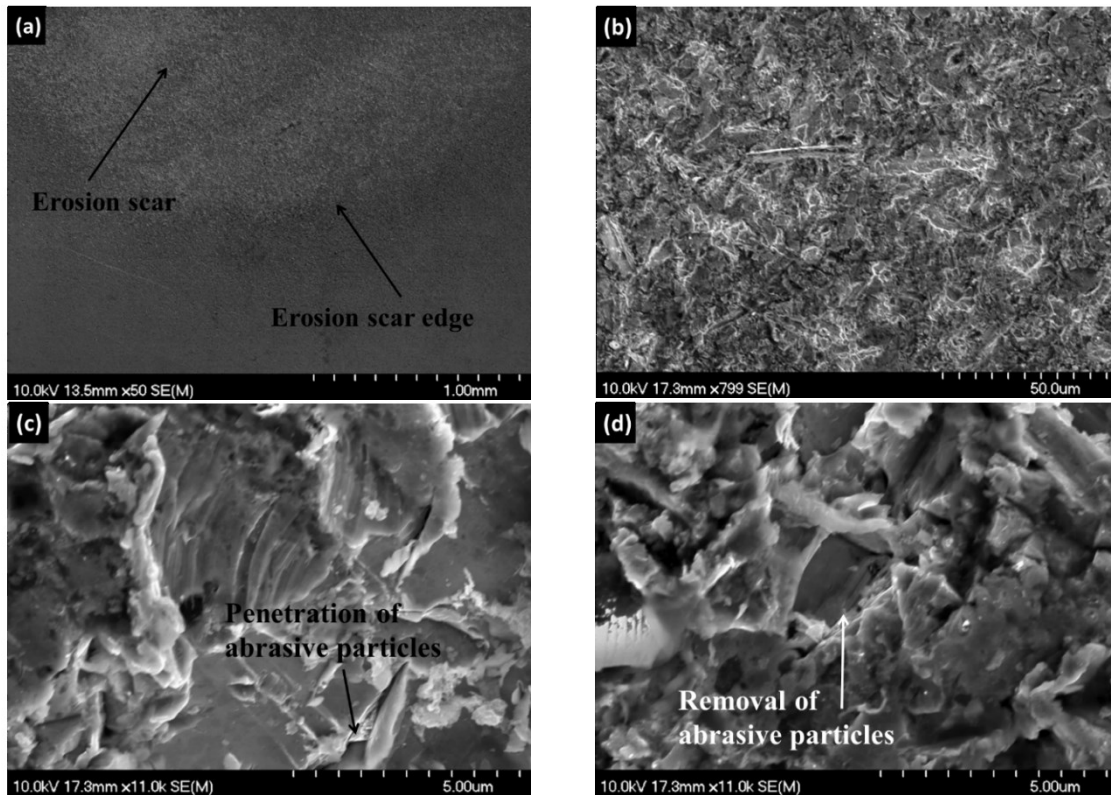

Figure 3-32 SEM micrographs of (a) erosion scar; (b) brittle fracture on the eroded sample; (c) penetration of abrasive particles observed on the 30s eroded surface; (d) removal of abrasive particles observed on the 30s eroded surface

Chapter 4

Conclusions

In this study, electroless Ni-P and Ni-P-Ti coatings were prepared and characterized. Three-point bending tests were employed to study the toughness of as-deposited and annealed Ni-P and Ni-P-Ti coatings. And indentation tests were performed on as-deposited and annealed Ni-P and Ni-P-Ti coatings. The relationship between microstructure and indentation behaviour was investigated. Erosion tests were conducted on as-deposited Ni-P coatings and the effect of impact angle on erosion behaviour was studied. The following conclusions can be drawn from the current work:

1. Electroless Ni-P coatings have smooth and uniform surfaces with strong interfaces. The addition of nano-titanium particles increases surface roughness.

2. As-deposited Ni-P coatings have an amorphous structure and the microstructure changes from amorphous into crystalline nickel and Ni_3P after annealing to 400°C. As the annealing temperature increased, the percentage of nickel phase increases, while that of Ni_3P decreases. The addition of nano-titanium particles does not change the amorphous structure of as-deposited coatings. Crystalline nickel and nickel phosphide phases are also identified in annealed Ni-P-Ti coatings, and Ni_3Ti is observed in Ni-P-Ti coatings after 600 and 800 °C annealing.

3. In Ni-P coatings, coating annealed at 400°C exhibits the highest hardness, followed by a decreasing hardness as annealing temperature continues to increase. The addition of titanium particles increases the hardness of as-deposited and annealed electroless Ni-P coating.

4. Toughness of annealed Ni-P coatings was investigated through bend tests. The coating annealed at 400°C shows the highest hardness and the lowest toughness, whereas the as-deposited coating is found to have the highest toughness. Toughness of Ni-P-Ti coating has a similar trend. As-deposited Ni-P-Ti coatings have the highest toughness, while coating annealed at 400°C is found to have the lowest toughness. The addition of titanium particles increases the toughness of as-deposited coatings.

5. The effect of thickness on indentation behaviour of Ni-P coatings is studied. Two thickness regions in which different damage types were identified in the study. Coating delamination due to substrate pile-up was observed in the thin coating. It is found that the thin coating is brittle, but it flexs due to low stiffness. For the thick coating, Hertzian, radial, bend cracks are observed.

6. Annealed electroless Ni-P coatings are more brittle than as-deposited coatings. Hertzian cracks and a high density of radial cracks are observed on the coating annealed at 400°C, which has a high percentage of Ni_3P and the highest hardness. Hertzian cracks and a low density of radial cracks are found on the coating annealed at a higher temperature. Radial cracks and micro-bend cracks form on as-deposited coating during unloading.

7. Hertzian cracks and radial cracks were observed on the as-deposited and Ni-P-Ti coatings annealed at low temperatures. For

coatings annealed at high temperatures, Hertzian, bend ring and radial cracks were found on the surface. However, annealing increases the interface strength between the coating and the substrate. Through bending and indentation fracturing of as-deposited coatings, coating delamination was identified

8. Normalized erosion rate of electroless Ni-P coating is 0.49×10^{-4}, while it is only 0.28×10^{-4} for the substrate, API X100 steel. The electroless Ni-P coating has a high erosion rate due to its brittleness. Dominant erosion mechanism was found to be brittle fracture.

9. Acoustic emission technique is found to be useful in detecting cracking initiation during indentation. Using acoustic emission technique, it is possible to determine the applied force that initiates the first crack during indentation. Acoustic emission is instrumental in identifying cracks during both loading and unloading.

10. Focused Ion Beam (FIB) technique was developed and found to be useful in explaining cracking patterns during indentation. Using the FIB technique, it was possible to explain how the Ni-P coating was compressed and squeezed to the sides of the contact area during indentation.

Publications generated from the present work include:

- **Published (Accepted)**

1. Wang, Chuhong, et al. "Indentation and erosion behaviour of electroless Ni-P coating on pipeline steel." Wear 376 (2017): 1630-1639.

2. Wang, Chuhong, et al. "Investigation of Fracture Behaviour of Annealed Electroless Ni-P Coating on Pipeline Steel using Acoustic Emission Methodology." Surface& Coating Technology.

- **Under Review**

3. Wang, Chuhong, et al. "Indentation and Bending Behaviour of Electroless Ni-P-Ti Composite Coating on Pipeline Steel." Surface& Coating Technology.

- **Conference**
  (21st International Conference on Wear of Materials (26-30 March 2017, Long Beach, California, USA))

  Presentation: Indentation and erosion behaviour of electroless Ni-P coating on pipeline steel.

  Poster: Ni-P coatings on pipeline steel: characterization and degradation behaviour analysis

Based on the results of the present study, the following work can be recommended for further studies:

1. Vary the amount of titanium powder in the Ni-P-Ti coating and assess its mechanical properties.

2. Vary the annealing temperature using narrow intervals for Ni-P-Ti coating and monitor microstructural evolution using TEM.

3. Study the erosion behavior of annealed Ni-P and Ni-P-Ti coatings.

4. Study the corrosion behavior of Ni-P-Ti coatings.

5. Developed a method for quantitative analysis of dent and bending resistance and fracture using acoustic emission data.

6. Monitor microstructural evolution during annealing for the presence of TiNi using SEM/EDS.

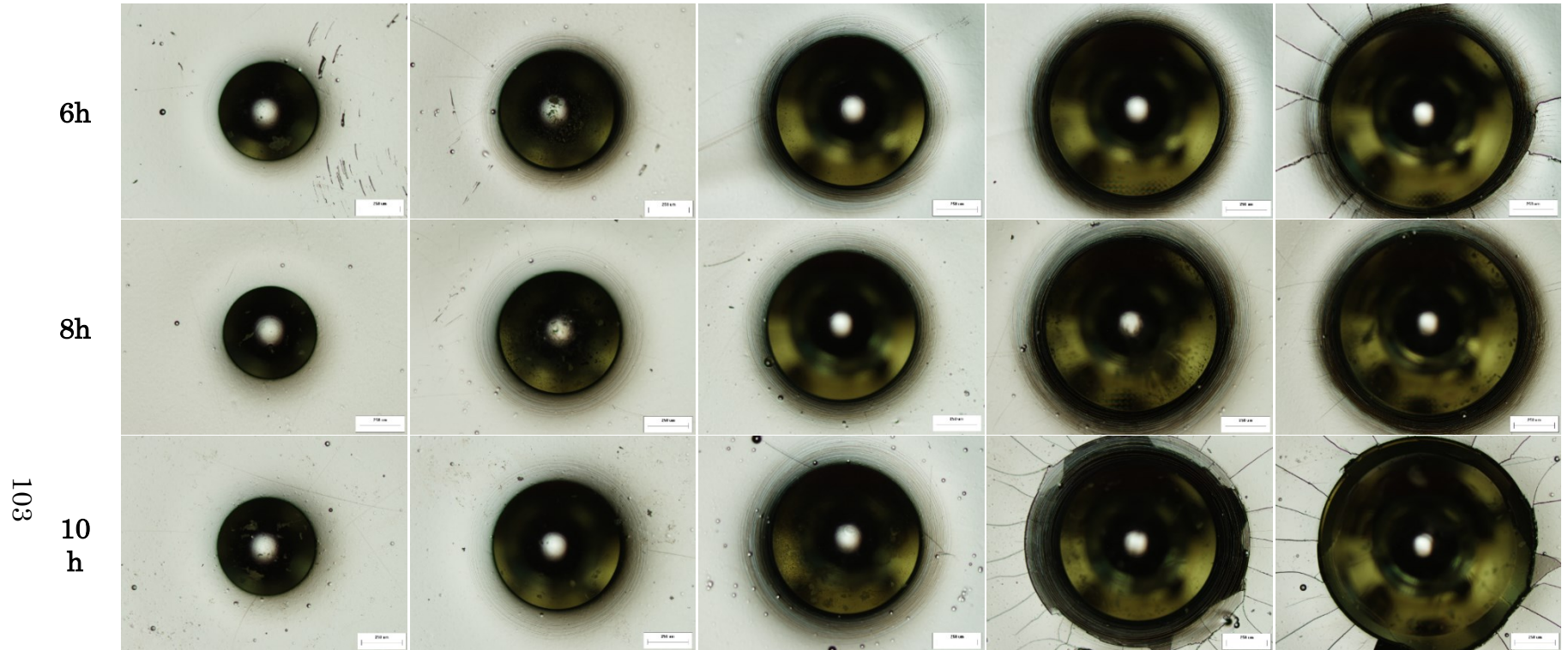|	600N	1000N	1500N	2000N	2300N
Steel					
1h					
4h					

102
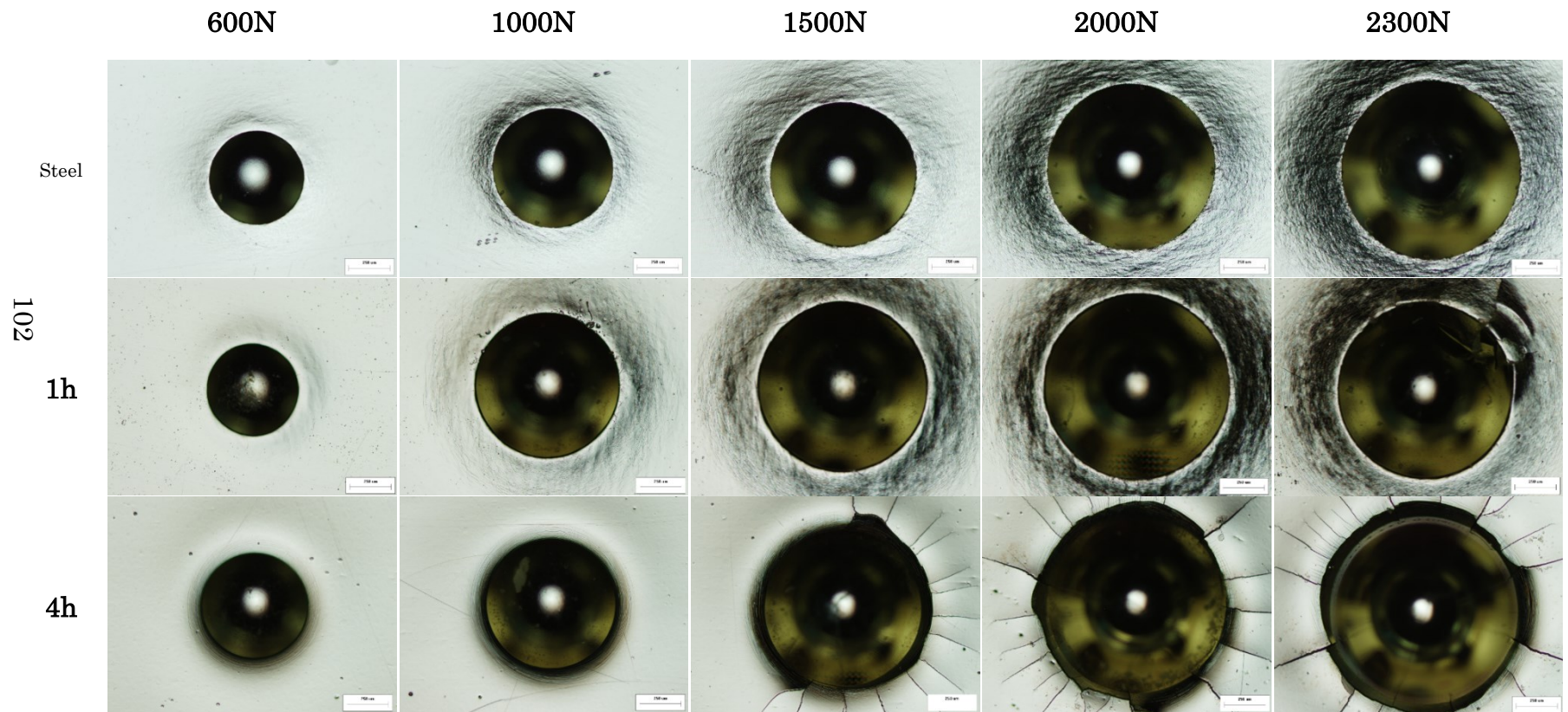
Table A-0-1Indentation surface views of as-deposited electroless Ni-P coatings with different thickness under different loads
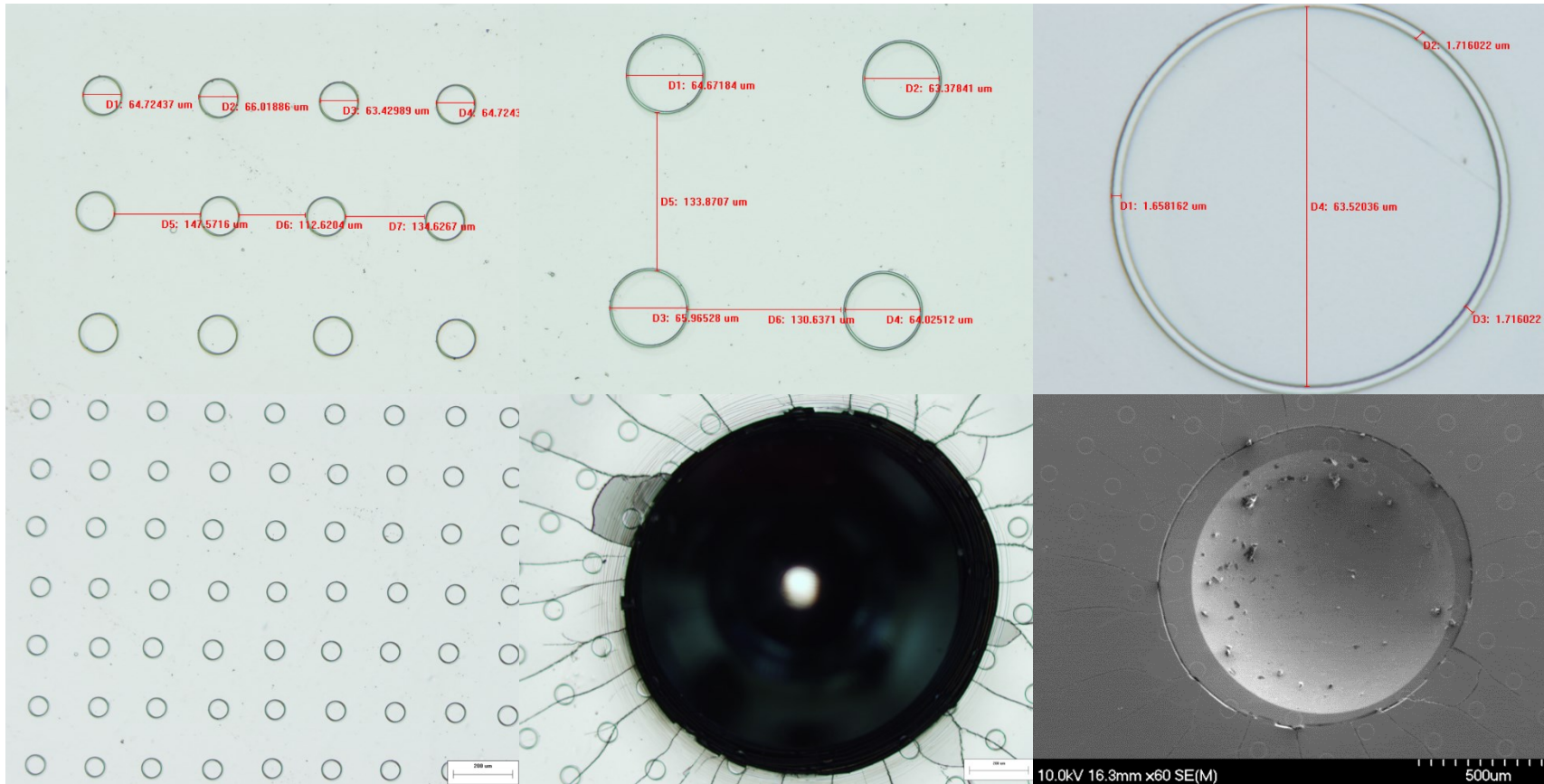
A B C

1 2

104

105

3

4
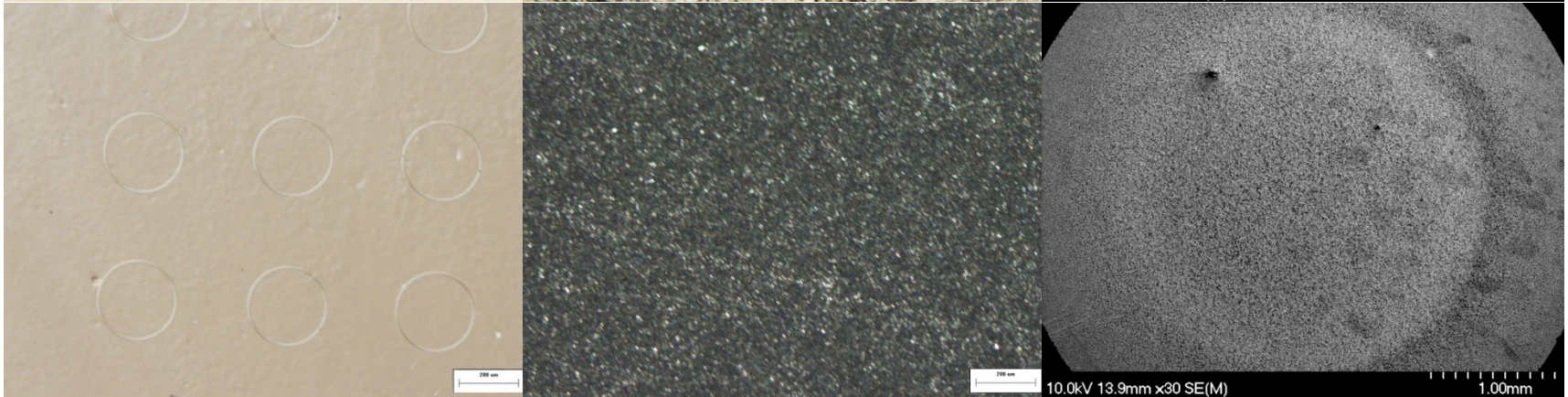
5
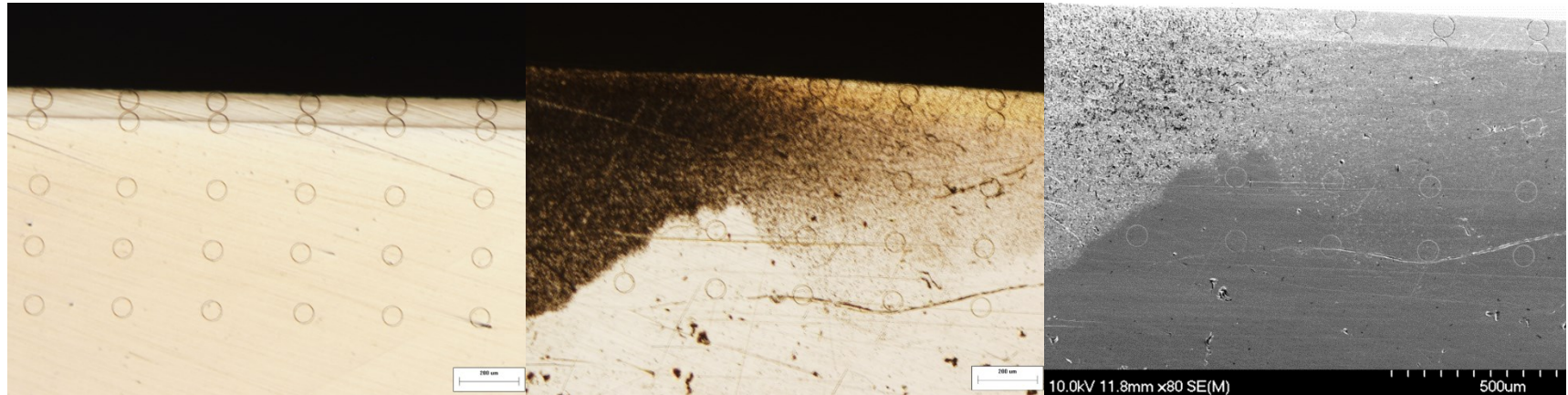
Table A-0-2Micrographs of indents and erosion scars of electroless Ni-P coatings using FIB technique.

1A-1C : Parameter of FIB circles.
2A: FIB circles on surface of indentation specimen before indentation. 2B: OM micrographs of FIB circles on surface of indentation specimen. 2C: SEM micrographs of FIB circles on surface of indentation specimen.
3A: FIB circles on cross-section of indentation specimen before indentation. 3B: OM micrographs of FIB circles on cross-section of indentation specimen. 3C: SEM micrographs of FIB circles on cross-section of indentation specimen.
4A: FIB circles on surface of erosion specimen before indentation. 4B: OM micrographs of FIB circles on surface of erosion specimen. 4C: SEM micrographs of FIB circles on surface of erosion specimen.
5A: FIB circles on cross-section of erosion specimen before indentation. 5B: OM micrographs of FIB circles on cross-section of erosion specimen. 5C: SEM micrographs of FIB circles on cross-section of erosion specimen.

Figure A 0-1 EDS results of Ni-P coating

Ni-P-Ti 6/20/2017 3:03:18 PM

Sample: Ni-P-Ti cross-section

Type: Default

Peaks possibly omitted : 6.398, 8.903 keV

Processing option : All elements analyzed (Normalised)

Number of iterations = 4

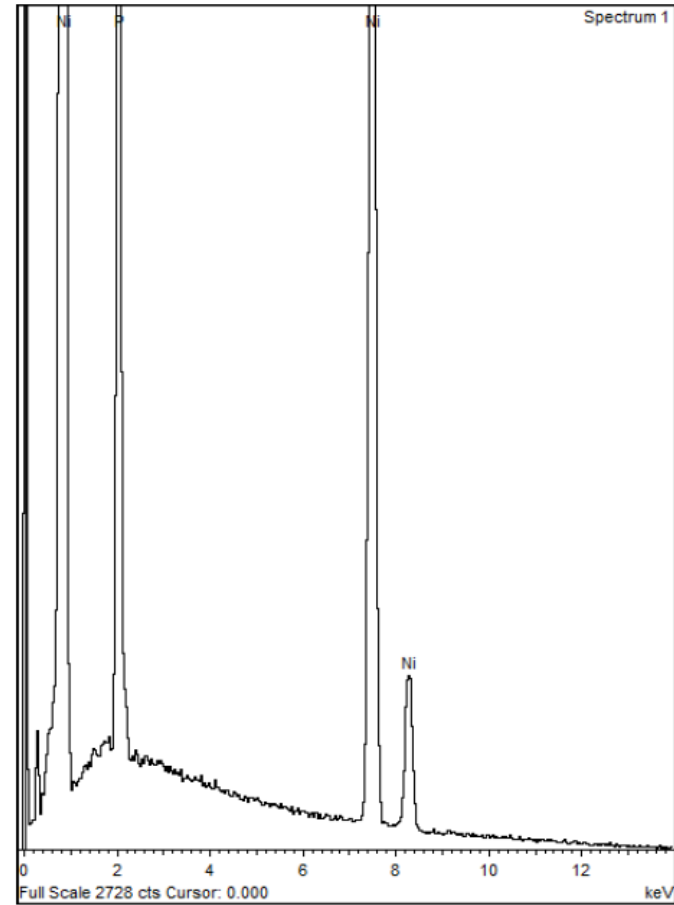| Element	Weight%	Atomic%
O K	2.51	7.91
P K	5.37	8.73
Ti L	22.76	23.92
Ni K	69.35	59.45

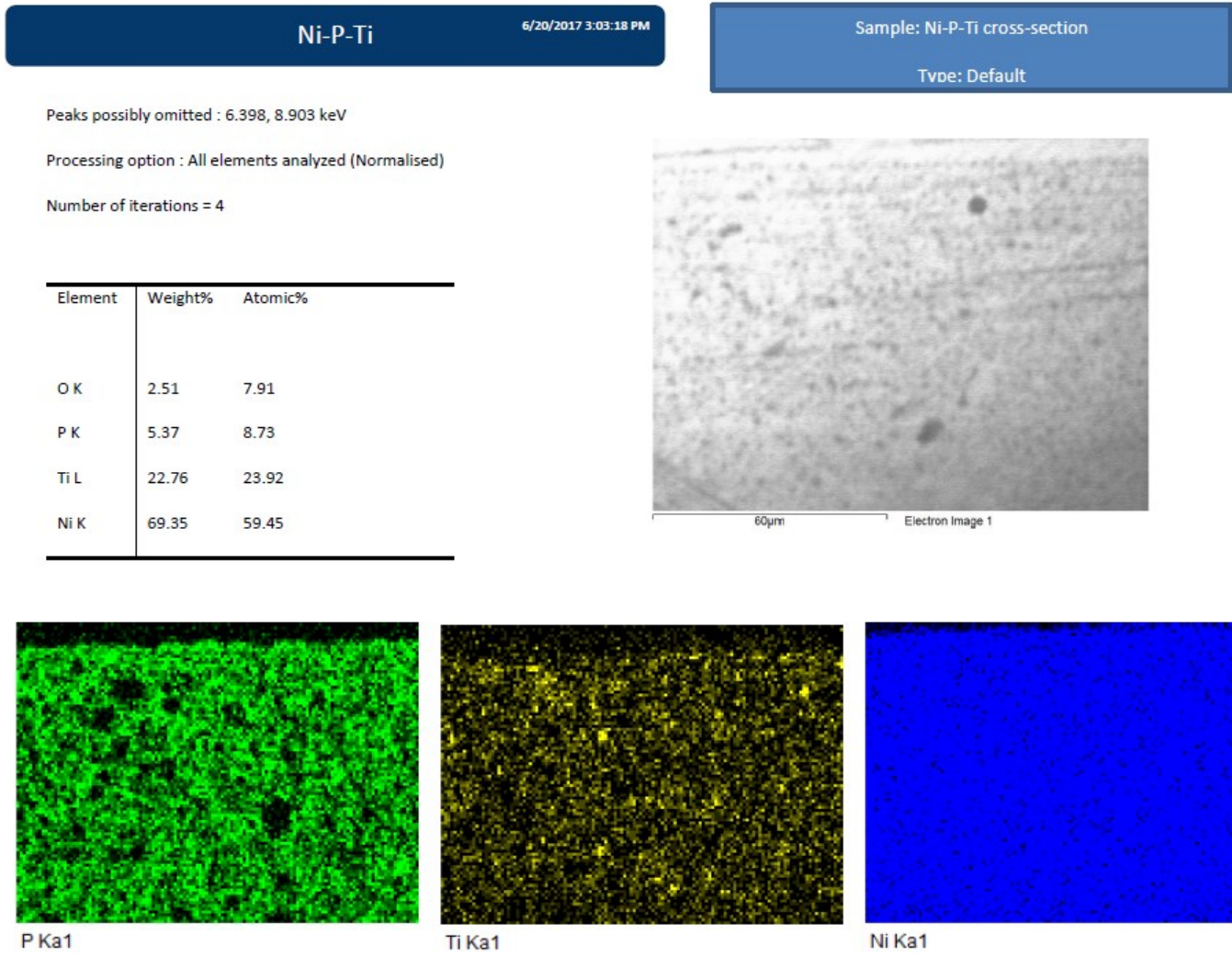60µm   Electron Image 1

P Ka1

Ti Ka1

Ni Ka1

Figure A-0-2 EDS map of cross-section of Ni-P-Ti coatings

References

[1] G. Haider, H. Arabnejad, S.A. Shirazi, B.S. McLaury, A mechanistic model for stochastic rebound of solid particles with application to erosion predictions, Wear, 376–377, Part A (2017) 615-624.

[2] M.A. Islam, T. Alam, Z.N. Farhat, A. Mohamed, A. Alfantazi, Effect of microstructure on the erosion behaviour of carbon steel, Wear, 332-333 (2015) 1080-1089.

[3] M.A. Islam, Z.N. Farhat, Effect of impact angle and velocity on erosion of API X42 pipeline steel under high abrasive feed rate, Wear, 311 (2014) 180-190.

[4] C. Wang, Z. Farhat, G. Jarjoura, M.K. Hassan, A.M. Abdullah, Indentation and erosion behaviour of electroless Ni-P coating on pipeline steel, Wear, 376–377, Part B (2017) 1630-1639.

[5] A. Cosham, P. Hopkins, The effect of dents in pipelines—guidance in the pipeline defect assessment manual, International Journal of Pressure Vessels and Piping, 81 (2004) 127-139.

[6] X.-H. Yang, W.-L. Zhu, Z. Lin, J.-J. Huo, Aerodynamic evaluation of an internal epoxy coating in nature gas pipeline, Progress in Organic Coatings, 54 (2005) 73-77.

[7] G.P. Guidetti, G.L. Rigosi, R. Marzola, The use of polypropylene in pipeline coatings, Progress in Organic Coatings, 27 (1996) 79-85.

[8] G.R. Howell, Y.F. Cheng, Characterization of high performance composite coating for the northern pipeline application, Progress in Organic Coatings, 60 (2007) 148-152.

[9] Electroless plating fundamentals and applications, Repr. ed.. ed., Orlando, Fla. : AESF
New York : Noyes Publications : William Andrew Publishing, Orlando, Fla. : New York, 1990.

[10] K.H. Krishnan, S. John, K. Srinivasan, J. Praveen, M. Ganesan, P. Kavimani, An overall aspect of electroless Ni-P depositions—a review article, Metallurgical and Materials Transactions A, 37 (2006) 1917-1926.

[11] R. Duncan, The metallurgical structure of electroless nickel deposits: effect on coating properties, Plating and surface finishing, 83 (1996) 65-69.

[12] Y.F. Shen, W.Y. Xue, Z.Y. Liu, L. Zuo, Nanoscratching deformation and fracture toughness of electroless Ni–P coatings, Surface and Coatings Technology, 205 (2010) 632-640.

[13] I.M. Hutchings, Ductile-brittle transitions and wear maps for the erosion and abrasion of brittle materials, Journal of Physics D: Applied Physics, 25 (1992) A212.

[14] P.H. Shipway, I.M. Hutchings, The rôle of particle properties in the erosion of brittle materials, Wear, 193 (1996) 105-113.

[15] S. Alirezaei, S.M. Monirvaghefi, M. Salehi, A. Saatchi, Wear behaviour of Ni–P and Ni–P–Al2O3 electroless coatings, Wear, 262 (2007) 978-985.

[16] J. Balaraju, S. Seshadri, Synthesis and corrosion behaviour of electroless Ni–P–Si3N4 composite coatings, Journal of Materials Science Letters, 17 (1998) 1297-1299.

[17] J. Balaraju, T. Sankara Narayanan, S. Seshadri, Evaluation of the corrosion resistance of electroless Ni-P and Ni-P composite coatings by electrochemical impedance spectroscopy, Journal of solid state electrochemistry, 5 (2001) 334-338.

[18] J. Balaraju, T. Sankara Narayanan, S. Seshadri, Electroless Ni–P composite coatings, Journal of applied electrochemistry, 33 (2003) 807-816.

[19] Z.N. Farhat, C. Zhang, The role of reversible martensitic transformation in the wear process of TiNi shape memory alloy, Tribology Transactions, 53 (2010) 917-926.

[20] D. Li, A new type of wear-resistant material: pseudo-elastic TiNi alloy, Wear, 221 (1998) 116-123.

[21] R. Neupane, Z. Farhat, Wear and dent resistance of superelastic TiNi alloy, Wear, 301 (2013) 682-687.

[22] G.M.P. Robert F. Cook, Direct Observation and Analysis of Indentation Cracking in Glasses and Ceramics, Journal of Ceramics, 73 (1990) 31.

[23] M.M. Lima, C. Godoy, P.J. Modenesi, J.C. Avelar-Batista, A. Davison, A. Matthews, Coating fracture toughness determined by Vickers indentation: an important parameter in cavitation erosion resistance of WC–Co thermally sprayed coatings, Surface and Coatings Technology, 177-178 (2004) 489-496.

[24] B.Q. Yang, K. Zhang, G.N. Chen, G.X. Luo, J.H. Xiao, Measurement of fracture toughness and interfacial shear strength of hard and brittle Cr coating on ductile steel substrate, Surface Engineering, 24 (2013) 332-336.

[25] S. Zhang, D. Sun, Y. Fu, H. Du, Toughness measurement of thin films: a critical review, Surface and Coatings Technology, 198 (2005) 74-84.

[26] A. Brenner, G.E. Riddell, Nickel plating on steel by chemical reduction, J. Res. Nat. Bur. Stand, 37 (1946) 31-34.

[27] J. Sudagar, J. Lian, W. Sha, Electroless nickel, alloy, composite and nano coatings–A critical review, Journal of Alloys and Compounds, 571 (2013) 183-204.

[28] W. Sha, X. Wu, K.G. Keong, Electroless copper and nickel-phosphorus plating: processing, characterisation and modelling, Elsevier, 2011.

[29] C. Leon, R. Drew, Preparation of nickel-coated powders as precursors to reinforce MMCs, Journal of Materials Science, 35 (2000) 4763-4768.

[30] R. Taheri, Evaluation of electroless nickel-phosphorus (EN) coatings, Mechanical Engineering, University of Saskatchewan, Saskatoon, 2003, pp. 268.

[31] G. Jiaqiang, L. Lei, W. Yating, S. Bin, H. Wenbin, Electroless Ni–P–SiC composite coatings with superfine particles, Surface and Coatings Technology, 200 (2006) 5836-5842.

[32] G. Jiaqiang, W. Yating, L. Lei, S. Bin, H. Wenbin, Crystallization temperature of amorphous electroless nickel–phosphorus alloys, Materials Letters, 59 (2005) 1665-1669.

[33] K.-H. Hur, J.-H. Jeong, D.N. Lee, Microstructures and crystallization of electroless Ni-P deposits, Journal of Materials Science, 25 (1990) 2573-2584.

[34] H. Ashassi-Sorkhabi, S.H. Rafizadeh, Effect of coating time and heat treatment on structures and corrosion characteristics of electroless Ni–P alloy deposits, Surface and Coatings Technology, 176 (2004) 318-326.

[35] C. Chen, H. Feng, H. Lin, M.-H. Hon, The effect of heat treatment on the microstructure of electroless Ni–P coatings containing SiC particles, Thin Solid Films, 416 (2002) 31-37.

[36] K.G. Keong, W. Sha, S. Malinov, Crystallisation kinetics and phase transformation behaviour of electroless nickel–phosphorus deposits with high phosphorus content, Journal of Alloys and Compounds, 334 (2002) 192-199.

[37] S.-K. Tien, J.-G. Duh, Y.I. Chen, The influence of thermal treatment on the microstructure and hardness in electroless Ni–P–W deposit, Thin Solid Films, 469 (2004) 333-338.

[38] R. Parkinson, Properties and applications of electroless nickel, Nickel Development Institute, 37 (1997).

[39] M.A. Islam, Z.N. Farhat, The synergistic effect between erosion and corrosion of API pipeline in CO2 and saline medium, Tribology International, 68 (2013) 26-34.

[40] S. Alirezaei, S.M. Monirvaghefi, M. Salehi, A. Saatchi, Effect of alumina content on surface morphology and hardness of Ni-P-Al2O3(α) electroless composite coatings, Surface and Coatings Technology, 184 (2004) 170-175.

[41] A. Grosjean, M. Rezrazi, Some morphological characteristics of the incorporation of silicon carbide (SiC) particles into electroless nickel deposits, Surface and Coatings Technology, 130 (2000) 252-256.

[42] Y. Wu, H. Liu, B. Shen, L. Liu, W. Hu, The friction and wear of electroless Ni–P matrix with PTFE and/or SiC particles composite, Tribology International, 39 (2006) 553-559.

[43] Y. Wu, B. Shen, L. Liu, W. Hu, The tribological behaviour of electroless Ni–P–Gr–SiC composite, Wear, 261 (2006) 201-207.

[44] H. Hertz, On the contact of elastic solids, J. Reine Angew Math., 92 (1881) 156-171.

[45] B.R. Lawn, Indentation of Ceramics with Spheres- A Century after Hertz, journal of advanced caremics, 81 (1998) 1977-1994.

[46] B. Lawn, R. Wilshaw, Indentation fracture: principles and applications, Journal of Materials Science, 10 (1975) 1049-1081.

[47] C. Jin, Indentation and Wear Damage Assessment of TiC-Stainless Steel Cermets, in: E. Department of Process, S. Applied, P. Doctor of, C. Dr. Thomas, D. Dr. Adam, F. Dr. Zoheir, T. Dr. Farid, P. Dr. Kevin, Received, Yes (Eds.), 2016.

[48] A.C. Fischer-Cripps, Introduction to contact mechanics, Springer, 2000.

[49] A. Almotairi, A. Warkentin, Z. Farhat, Mechanical damage of hard chromium coatings on 416 stainless steel, Engineering Failure Analysis, 66 (2016) 130-140.

[50] B. Lawn, M. Swain, Microfracture beneath point indentations in brittle solids, Journal of Materials Science, 10 (1975) 113-122.

[51] B.R. Lawn, E. Fuller, Equilibrium penny-like cracks in indentation fracture, Journal of Materials Science, 10 (1975) 2016-2024.

[52] A.G. EVans, E.A. Charles, Fracture toughness determinations by indentation, Journal of the American Ceramic Society, 59 (1976) 371-372.

[53] B.R. Lawn, A. Evans, D. Marshall, Elastic/plastic indentation damage in ceramics: the median/radial crack system, Journal of the American Ceramic Society, 63 (1980) 574-581.

[54] X.L. Gao, X.N. Jing, G. Subhash, Two new expanding cavity models for indentation deformations of elastic strain-hardening materials, International Journal of Solids and Structures, 43 (2006) 2193-2208.

[55] H. Chai, B. Lawn, S. Wuttiphan, Fracture modes in brittle coatings with large interlayer modulus mismatch, Journal of Materials Research, 14 (1999) 3805-3817.

[56] H. Chai, B.R. Lawn, Fracture mode transitions in brittle coatings on compliant substrates as a function of thickness, Journal of Materials Research, 19 (2011) 1752-1761.

[57] Standard Test Methods for Flexural Properties of Unreinforced and Reinforced Plastics and Electrical Insulating Materials, ASTM International, 2015.

[58] A. Rouzaud, E. Barbier, J. Ernoult, E. Quesnel, A method for elastic modulus measurements of magnetron sputtered thin films dedicated to mechanical applications, Thin Solid Films, 270 (1995) 270-274.

[59] E. Harry, A. Rouzaud, M. Ignat, P. Juliet, Mechanical properties of W and W (C) thin films: Young's modulus, fracture toughness and adhesion, Thin Solid Films, 332 (1998) 195-201.

[60] Y.W. Bao, Y.C. Zhou, X.X. Bu, Y. Qiu, Evaluating elastic modulus and strength of hard coatings by relative method, Materials Science and Engineering: A, 458 (2007) 268-274.

[61] H. Li, K. Khor, P. Cheang, Young's modulus and fracture toughness determination of high velocity oxy-fuel-sprayed bioceramic coatings, Surface and Coatings Technology, 155 (2002) 21-32.

[62] S. Afroukhteh, C. Dehghanian, M. Emamy, Preparation of the Ni–P composite coating co-deposited by nano TiC particles and evaluation of it's corrosion property, Applied Surface Science, 258 (2012) 2597-2601.

[63] Y. Charron, C. Mabile, European program studies ways to fight internal pressure losses in gas lines, Pipeline & gas journal, 231 (2004) 36-39.

[64] L. Niu, Y.F. Cheng, Development of innovative coating technology for pipeline operation crossing the permafrost terrain, Construction and Building Materials, 22 (2008) 417-422.

[65] Y.I. Oka, H. Ohnogi, T. Hosokawa, M. Matsumura, The impact angle dependence of erosion damage caused by solid particle impact, Wear, 203 (1997) 573-579.

[66] A.W. Ruff, L.K. Ives, Measurement of solid particle velocity in erosive wear, Wear, 35 (1975) 195-199.

[67] I.M. Hutchings, R.E. Winter, Particle erosion of ductile metals: A mechanism of material removal, Wear, 27 (1974) 121-128.

[68] S. Wiederhorn, B. Hockey, Effect of material parameters on the erosion resistance of brittle materials, Journal of Materials Science, 18 (1983) 766-780.

[69] H. Wensink, M.C. Elwenspoek, A closer look at the ductile–brittle transition in solid particle erosion, Wear, 253 (2002) 1035-1043.

[70] Q.S. Fu, R.S. Yang, M.T. Li, Study on Elastic Modulus of Porous Ti Coatings by Three-Point Bending and Indentation Measurement, Advanced Materials Research, 2014, pp. 74-77.

[71] W. Ziaja, J. Sieniawski, M. Ossowski, K. Kubiak, Deformation behaviour of surface treated two-phase titanium alloy in bending, Ti 2011 - Proceedings of the 12th World Conference on Titanium, 2012, pp. 1132-1136.

[72] R.B. Collier, K.P. Plucknett, Spherical indentation damage in TiC–Ni3Al composites, International Journal of Refractory Metals and Hard Materials, 30 (2012) 188-195.

[73] I.M. Hutchings, P. Shipway, Tribology: friction and wear of engineering materials, 1992.

[74] E.N. Landis, L. Baillon, Experiments to relate acoustic emission energy to fracture energy of concrete, Journal of engineering mechanics, 128 (2002) 698-702.

[75] S. Muralidhara, B.R. Prasad, H. Eskandari, B.L. Karihaloo, Fracture process zone size and true fracture energy of concrete using acoustic emission, Construction and Building Materials, 24 (2010) 479-486.

[76] J. Radon, A. Pollock, Acoustic emissions and energy transfer during crack propagation, Engineering Fracture Mechanics, 4 (1972) 295-310.

[77] R. Taheri, Evaluation of electroless nickel-phosphorus (EN) coatings, University of Saskatchewan Saskatoon, 2002.

[78] M.H. Staia, E.S. Puchi, G. Castro, F.O. Ramirez, D.B. Lewis, Effect of thermal history on the microhardness of electroless Ni–P, Thin Solid Films, 355 (1999) 472-479.

[79] C. Lin, N. Dadvand, Z. Farhat, ELECTROLESS NICKEL PHOSPHORUS PLATING ON CARBON STEEL, Materials Science &

Technology Conference and Exhibition 2013, Montreal, Quebec, Canada, 2013, pp. 2224-2237.

[80] P. Sahoo, S.K. Das, Tribology of electroless nickel coatings–a review, Materials & Design, 32 (2011) 1760-1775.

[81] C.K. Chen, H.M. Feng, H.C. Lin, M.H. Hon, The effect of heat treatment on the microstructure of electroless Ni–P coatings containing SiC particles, Thin Solid Films, 416 (2002) 31-37.

[82] Q. Zhao, Y. Liu, H. Müller-Steinhagen, G. Liu, Graded Ni–P–PTFE coatings and their potential applications, Surface and Coatings Technology, 155 (2002) 279-284.

[83] C.A. Schuh, T.C. Hufnagel, U. Ramamurty, Mechanical behaviour of amorphous alloys, Acta Materialia, 55 (2007) 4067-4109.

[84] F. Luborsky, Amorphous metallic alloys, Butterworth and Co (Publishers): London, UK, 1983.

[85] E. Harry, M. Ignat, A. Rouzaud, P. Juliet, Cracking investigation of W and W(C) films deposited by physical vapor deposition on steel substrates, Surface and Coatings Technology, 111 (1999) 177-183.

[86] Z. Chen, Z. Wang, S. Zhu, Tensile fracture behaviour of thermal barrier coatings on superalloy, Surface and Coatings Technology, 205 (2011) 3931-3938.

[87] V.D. Papachristos, C.N. Panagopoulos, L.W. Christoffersen, A. Markaki, Young's modulus, hardness and scratch adhesion of Ni–P–W multilayered alloy coatings produced by pulse plating, Thin Solid Films, 396 (2001) 174-183.

[88] Y. Suzuki, T. Egami, Shear deformation of glassy metals: Breakdown of cauchy relationship and anelasticity, Journal of non-crystalline solids, 75 (1985) 361-366.

[89] B. Bergman, On the variability of the fracture stress of brittle materials, Journal of Materials Science Letters, 4 (1985) 1143-1146.

[90] B. Lawn, Fracture of brittle solids, Cambridge university press, 1993.

[91] R. Hill, The mathematical theory of plasticity, Oxford university press, 1998.

[92] R.F. Cook, G.M. Pharr, Direct observation and analysis of indentation cracking in glasses and ceramics, Journal of the American Ceramic Society, 73 (1990) 787-817.